DISCRETE ELEMENT MODELING OF RAILROAD BALLAST USING IMAGING BASED AGGREGATE MORPHOLOGY CHARACTERIZATION

BY

HAI HUANG

DISSERTATION

Submitted in partial fulfillment of the requirements
for the degree of Doctor of Philosophy in Civil Engineering
in the Graduate College of the
University of Illinois at Urbana-Champaign, 2010

Urbana, Illinois

Doctoral Committee:

Professor Erol Tutumluer, Chair
Professor Christopher P.L. Barkan
Associate Professor Youssef M.A. Hashash
Professor Emeritus Marshall R. Thompson
Professor Emeritus Jamshid Ghaboussi

DISCRETE ELEMENT MODELING OF RAILROAD BALLAST USING IMAGING BASED AGGREGATE MORPHOLOGY CHARACTERIZATION

Hai Huang, Ph.D.
Department of Civil and Environmental Engineering
University of Illinois at Urbana Champaign, 2009
Erol Tutumluer, Advisor

Ballast is an essential layer of the railroad track structure, and provides primarily drainage and load distribution. In general, ballast aggregates are considered as uniformly graded, angular shaped with crushed faces. However, various ballast aggregate gradations and particle shapes are in use yet their effects on ballast performances remain unknown. In previous designs and modeling practices, railroad ballast has usually been treated as a homogeneous and continuous layer. This approach is not suitable to model the deformation behavior of the particulate nature railroad ballast aggregates under dynamic moving loads. Further, continuum solutions do not take into account realistically the morphological characteristics of aggregates such as particle size distribution and shapes. A combined digital image and Discrete Element Modeling (DEM) methodology has been developed in this PhD thesis to study effects of aggregate particle size and morphological characteristics on ballast performances. The approach has been calibrated using actual ballast aggregates through laboratory shear box texts and validated by further laboratory as well as field experiments. Using the DEM ballast model, individual effects of aggregate particle size distributions and shape properties on railroad ballast strength, lateral stability, and settlement potential were studied. From the DEM simulation results, it was found that aggregate particle size distribution and shape have significant impact on ballast performances. Ballast with broader size distribution was shown to yield less settlement potential than ballast with more uniformly graded aggregates. Also, ballast with angular aggregate particles were found from the DEM simulations to have higher strength as well as better lateral stability than ballast with rounded aggregate particles due to better stone on stone contact and aggregate interlock. In summary, the developed DEM ballast model has been proven in this PhD research to be a promising tool for studying railroad ballast load and deformation characteristics and could lead to the ultimate goal of designing better “engineered ballast.”

To My Parents Bingxun Huang & Huixian Yu
My Wife Shihui Shen
and My Daughter Sarah Huang

ACKNOWLEDGMENTS

This project would not have been possible without the support of many people. I am greatly in debt to my advisor, Professor Erol Tutumluer, who had led me through all these years of hard working, read my numerous revisions and made it a high quality final product. Thanks to my committee members, Professor Christopher P.L. Barkan, Associate Professor Youssef M.A. Hashash, Professor Marshall R. Thompson, and Professor Jamshid Ghaboussi, who offered guidance and support. Also thanks to Association of American Railroads (AAR) and Burlington Northern Santa Fe (BNSF) for their continuous support to our research. Many thanks to all friends I have made in Champaign, Professor Decheng Feng, Professor Xiaoming Huang, Mr. Zach W. Dombrow, Mr. Marcus S. Dersch, Mr. Hao Wang, Mr. Yuanjie Xiao and my badminton fellows, Dr. Ning Xie, Mr. Dingfeng Zhang, Dr. Zhengting Dai, Mr. Di Yun, Mr. Jingjin Yu, especially my partner Mr. Zhen Leng for such a joyful and memorable time they had brought to my life. I would like to express my sincere gratitude to my officemate Dr. Onur Pekcan who had always been on my side through those hard times. Finally, thanks to my wife, for always offering support and love without hesitate.

TABLE OF CONTENTS

LIST OF FIGURES

LIST OF TABLES

1. INTRODUCTION

Track is one of the basic elements that the railroad sector relies on. Traditional tracks consist of four basic components: rail, tie, ballast, and subgrade (see Figure 1.1). Wheel loads applied by rail and ties are distributed when passing through the ballast layer so that the low strength subgrade soil is protected. Ballast layer is usually made up of angular shaped coarse granular materials which serve the purpose of providing drainage, load distribution, strength, and stability. It needs to be closely monitored and regularly maintained to avoid deterioration, misalignment and consequently train derailments.

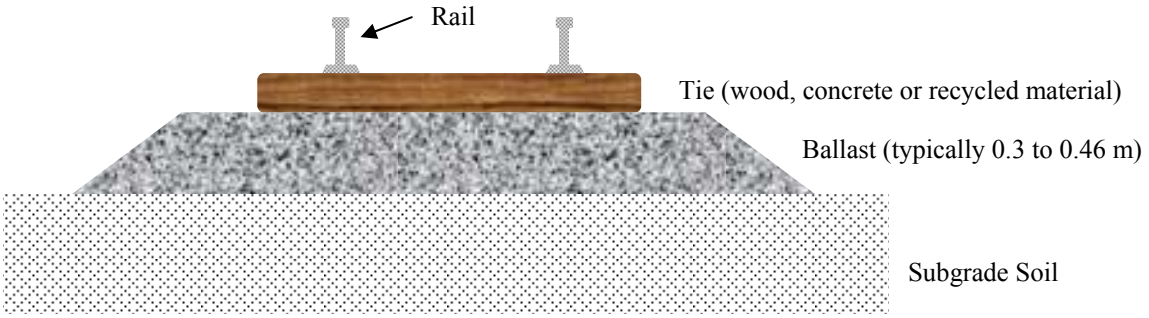

Figure 1.1 Typical Railroad Track Structure

1.1 Problem Statement

Problems investigated by this work are railroad track buckle and ballast settlement usually associated with the ballast component of track that require remedial action and routine maintenance. Figure 1.2 shows a typical track buckle due to lack of ballast lateral stability. Track lateral stability mainly comes from resistance supplied by rail lateral rigidity and tie ballast lateral interaction. Buckling usually happens in the hot summer

season just after ballast maintenance activities such as tamping. Tamping aims to raise the ballast layer and correct the track vertical profile. During tamping, tie is raised followed by inserting the tamping arms which squeeze and vibrate the ballast. Usually the track vertical profile can be corrected by one to several rounds of tamping. However, tamping dramatically decreases the ballast strength and lateral stability by disturbing the consolidated or shaken-down ballast. Tie lateral pull out tests show that ballast could lose up to 60% of its original lateral resistance to tie movement after tamping (Selig and Waters, 1994).

Figure 1.2 Track Buckle (Courtesy of FRA)

Many factors may influence the tie ballast lateral interaction, namely: aggregate shape properties including aggregate angularity and surface texture; tie-aggregate contact interface; and ballast compaction level. Among these factors, aggregate type and shape properties have been known to directly affect the compaction of ballast, lateral stability, settlement, and the long term performance of the railroad track.

According to the American Railway Engineering and Maintenance of Way Association (AREMA), ballast aggregate should be uniformly graded with hard, angular shaped particles providing sharp corners and cubical fragments with a very low percentage of flat and elongated particles (maximum 5% by weight over 3 to 1 longest to shortest dimensional ratio). Yet, there is so far no standard test procedure to evaluate ballast lateral stability and settlement potential in terms of ballast aggregate angularity and surface texture other than common visual inspection. As a result, the influences of aggregate shape on ballast strength, lateral stability, and deformation characteristics have not been thoroughly investigated by means of quantifying individually the effects of aggregate morphological properties.

Under repeated train loadings, ballast layer accumulates both recoverable and unrecoverable deformation vertically. When the unrecoverable ballast deformation increases to cause considerable settlement and stability problems, maintenance activities such as tamping are performed to maintain the track level. How ballast aggregate size distribution (i.e. gradation) and shape properties such as angularity and surface texture affect the ballast settlement needs to be addressed.

In the past few decades, research studies on railroad ballast extensively relied on expensive full-scale experiments both in the laboratory (Hay et al., 1977) and field (Li and Davis, 2005). Computer modeling techniques such as Finite Element Method (FEM) used for track analysis can hardly simulate the behavior of a particulate assembly such as the ballast layer to properly address problems related to track fouling, lateral stability, and settlement. In a ballast layer, individual aggregate particles move independently and interact only at contact points. Such discrete nature of the medium results in a complex

behavior of the granular assembly, which is very difficult to model by continuum theory used in the FEM. In addition, dilation, inter-particle sliding and nonlinear stress dependent behavior of granular materials with typical anisotropic stiffness and deformation properties under vertically induced load application are almost impossible to be adequately modeled using the continuum approach.

1.2 Research Objectives

In this study, a computational simulation model for the particulate nature of ballast referred to as the "Discrete Element Method (DEM)" will be introduced. A "Ballast DEM Model" is proposed based on a digital image aided particle shape generation for DEM and applied to simulate in full-scale railroad ballast behavior. Specific objectives to be accomplished are listed as follows:

(1) Establish ballast shape properties from processing digital images of aggregate particles;

(2) Introduce a "Digital Image Aided Particle Shape Generation Method" for DEM and validate the "Ballast DEM Model" using both laboratory and field collected data;

(3) As a starting point of designing "engineered ballast", investigate the effects of ballast aggregate gradation on the settlement of ballast by using "Ballast DEM Model";

(4) Use this model to investigate effects of aggregate shape properties including angularity and surface texture on the aggregate assembly strength, ballast aggregate settlement and lateral stability;

The research study aims to contribute to the development of a "Ballast DEM Model" that will help engineers better understand the behavior and performance of ballast

through realistic modeling of the effects of aggregate shape and size distribution on lateral stability, settlement, and the dynamic interactions under loading. The validated DEM ballast model developed is expected to provide improved railroad ballast design and maintenance practices by providing an analysis and design tool.

1.3 Research Scope

Identified as a "viable image processing technique" by NCHRP 4-30A project (Masad et al. 2005), the "University of Illinois Aggregate Image Analyzer (UIAIA)" and the aggregate morphological indices developed from UIAIA are considered in the study scope to evaluate ballast aggregate shape properties. Three dimensional (3D) element shapes are generated from UIAIA with different shape properties.

A novel DEM program BLOKS3D (Zhao et al. 2006) is also chosen as the modeling tool to be equipped with different element shape libraries generated from UIAIA. BLOKS3D uses user-defined 3-D "blocks" or polyhedrons as the basic elements to realistically simulate interactions such as interlock/contact of actual ballast aggregate particles.

The "Ballast DEM Model" is validated by experiments conducted by a large shear box equipment in the Newmark Civil Engineering Laboratory (NCEL) at the University of Illinois. The test device is a square box with side dimensions of 305 mm (12 in.) and a specimen height of 203 mm (8 in.). It has a total 102 mm (4 in.) travel of the bottom 152 mm (6 in.) high component, which is large enough for ballast testing purposes to record peak shear stresses. The vertical (normal direction) and horizontal load cells are capable of applying and recording up to 40 kN (8,889 lb) load magnitudes. The device controls

and the data collection are managed through an automated data acquisition system controlled by the operator through a built-in display and the test data are saved on to a personal computer.

For field validation of the methodology, settlement predictions from a half track DEM simulation model are compared with field settlement data collected from the Association of American Railroads' Transportation Technology Center, Inc (TTCI) test track in Pueblo, Colorado. Similar geometries, loading conditions, and ballast aggregate shape and size distributions are used to accomplish such model validation. To apply the similar track loading conditions in DEM simulations, a recently developed dynamic track model is also employed to calculate the loading profile on top of the ballast layer based on the traffic data collected from TTCI.

The validated "Ballast DEM Model" is first used to study ballast aggregate gradations and their impact on railroad ballast settlement by performing half track DEM settlement simulations. Ballast aggregate materials with different size distributions, including typical AREMA gradations, are generated in the DEM simulations and tested under repeated loading. The "Ballast DEM Model" is also used to study the aggregate shape (angularity and surface roughness) effects on the assembly strength through performing shear box simulations. Tie lateral pull out simulations are also performed to evaluate the aggregate shape effects on ballast settlement and lateral stability before and after tamping.

It is the ultimate goal to utilize the "Ballast DEM Model" for selecting ballast and engineering its properties. For example, by identifying the size and shape requirements for aggregate gradation, angularity, and surface texture, an "engineered ballast" aggregate

material can be developed for improved performance which would result in adequate track stability and low settlement potential.

1.4 Thesis Outline

In Chapter 2, a literature review is provided to cover several topics including aggregate gradation, lateral stability, track settlement, as well as concepts related to Discrete Element Modeling, ballast aggregate shape effects, and digital image analysis. In Chapter 3, the "Digital Image Aided Particle Shape Generation Method" is introduced and explained in detail. Chapter 3 also gives details on the laboratory research undertaken to evaluate and validate the applicability of the Ballast DEM Model. In Chapter 4, the ballast DEM model is further demonstrated to predict an actual record of track ballast settlement due to repeated train traffic. In Chapter 5, aggregate gradation effect is investigated by comparing settlements predicted by DEM for various different ballast gradations. In Chapter 6, the approach is applied to study aggregate shape effects on strength, settlement, and lateral stability of railroad ballast. Finally, Chapter 7 summarizes research effort and conclusions and future recommendations are provided.

2. LITERATURE REVIEW

In this chapter, a literature review of the background and recent research efforts related to this study is provided. The literature review includes the following topics: ballast gradation, ballast lateral stability, track settlement, and concepts related to Discrete Element Modeling, ballast aggregate shape effects and digital image analysis.

2.1 Ballast Gradation

Gradation is a term to describe the size and size distribution of a granular media. It is usually expressed as a relationship (gradation curve) between size and percentage by weight of particles smaller than that size. Gradation is one of the most influential aggregate characteristics in determining how aggregates will perform in a constructed structural layer. In bound Hot Mix Asphalt (HMA) layers, aggregate gradation influences almost every important property including stiffness, permeability, workability, and resistance to moisture damage (Roberts et al., 1996). Recently, Vavrik (2000) proposed a new HMA gradation design called the Bailey method that adequately characterized HMA voids and compaction characteristics for improved performance.

In Portland Cement Concrete (PCC), gradation impacts durability, porosity, and aggregate to cement bond strength through surface area characteristics of different aggregate sizes. Extensive research has been conducted on the optimization of aggregate packing in the concrete industry (Shilstone, 1990; Roy et al., 1993; de Larrard and Sedran, 1994; and Goltermann et al., 1997). A study by University of Wisconsin researchers has shown that with an optimized aggregate gradation an increase in concrete strength of 10

to 20 percent could be achieved (Goltermann et al., 1997). They also noticed decreased segregation after extended vibration, which leads to better quality construction and longer performance life. The air voids of compacted aggregate ranged from 32% to 41% depending on the gradation (Goltermann et al., 1997). For continuously graded sand, air voids are typically 33% to 38% (Powers, 1964).

Previous research efforts mainly focused on identifying relationships between the aggregate density and gradation. For example, analytical models exist for evaluating the densities resulting from combining two different sizes (binary packing) of spherical particles; those with spherical particle diameter ratios (small diameter divided by large diameter) below 0.22 and those with spherical particle diameter ratios above 0.22 (Johansen and Anderson, 1990). Toufar et al. (1976) indicated that the smaller particles, in the case of the diameter ratios greater than 0.22, would be too large to fit in the interstices between the large particles. Such models directly deal with aggregate particle sizes and packing orders to dictate density and air void content of a granular assembly.

Railroad ballast is often designed using uniformly graded material to mainly satisfy the drainage requirement. However, uniformly graded aggregates may tend to be structurally less stable due to larger air voids and possibly yield more settlement than continuously or densely graded materials. A good ballast design needs to consider both void space and structural stability.

It is usually reasonable to assume that the "preferred" gradation is the one that produces the maximum density which creates more particle-to-particle contact, thus increase the structural stability. In PCC, this reduced void space reduces the amount of cement paste required. Therefore, maximum density gradation generally provides a

common reference. A widely used equation to describe a maximum density gradation was developed by Fuller and Thompson (1907). Their basic equation is:

$$p = (\frac{d}{D})^n \quad 2.1$$

where: p is the percentage finer than the size;

d is the aggregate size being considered;

D is the maximum aggregate size;

n is around 0.5 for maximum density according to Fuller and Thompson (1907).

In the early 1960s, the FHWA introduced the standard gradation graph used in the HMA industry today. This graph uses n = 0.45 and is convenient for determining the maximum density line and adjusting gradation (Roberts et al., 1996). This graph is slightly different than other gradation curves because it uses the sieve size raised to the n^{th} power (usually 0.45) as the x-axis units. Thus, the maximum density line appears as a straight line from zero to the maximum aggregate size for the mixture being considered.

Railroad ballast is usually considered as uniformly graded. There are, however, different gradations of ballast commonly used around the world such as AREMA ballast gradations (see Table 2.1), French gradation, Australian gradation, etc. Efforts have been made to improve ballast performance by adjusting aggregate size distributions (Indraratna et al. 2004). From laboratory tests conducted by Indraratna et al. (2004) the use of slightly broader graded ballast gives lower settlement while not affecting drainage significantly.

Table 2.1 Typical Ballast Gradations According to AREMA (2000)

No.	Nominal Size Square Opening	Percentage Passing								
		76.2 mm	63.5 mm	50.8 mm	38.1 mm	25.4 mm	19.1 mm	12.7 mm	9.5 mm	4.75 mm
24	63.5-19.1 mm	100	90-100		25-60		0-10	0-5		
25	63.5-12.7 mm	100	80-100	60-85	50-70	25-50		5-20	0-10	0-3
3	50.8-25.4 mm		100	95-100	35-70	0-15		0-5		
4A	50.8-19.1 mm		100	90-100	60-90	10-35	0-10		0-3	

2.2 Ballast Lateral Stability

Due to insufficient super elevation, track at a curve experiences lateral forces from the train wheels. At tangential track, there also exist lateral forces coming from the wheel-rail negotiating movements. These dynamic forces are balanced by the rail lateral rigidity and the lateral resistance from the tie-ballast structure. Track becomes unstable under lateral impacts especially when the rail axial compressive force induced by summer high temperature increases. Adequate lateral resistance is essential to provide a stable track structure necessary for safe rail operations on passenger and freight railroad track.

Early research studies on lateral stability mainly focused on the rail buckle potential and behavior at high temperature. Ammann and Gruenewaldt (1932) conducted extensive tests of track buckling under compressive forces applied by hydraulic jacks. They observed that the buckling rail consisted of two horizontal half waves with 19 meters each in length. The largest lateral movement of the track was recorded to be 40 cm.

Raab (1934) conducted rail buckle tests by heating the rail with electric currents. The critical track buckling temperature was 105 ^{o}C. Birmann and Raab (1960) concluded that rails without noticeable geometric imperfections buckled at much higher loads than those with imperfections in the horizontal plane.

Bromberg (1966) conducted buckling tests on both tangential and curved tracks and discovered that the lateral displacement caused by buckle during heating will not vanish during cooling. Kerr (1975) suggested that the use of jacks for inducing "thermal force" should be avoided and the track test section should be sufficiently long. Kish and Samavedam (1991) in their study proposed the concept of "safe temperature increase" for continuously welded rails.

At the University of Illinois, railroad experiments by Hay et al. (1977) utilized a 60 kg (132-lb) rail, three-tie track segment using gravel, crushed limestone, and crushed steel slag as ballast. The track was loaded by hydraulic rams that gave both steady and pulsating loads equivalent to those of a 9,000 kg (20,000 lb) wheel. Shear reaction forces at different displacements were recorded. It was observed that the shear reaction force was built to a peak at about 12.7 mm (0.5 in.) lateral displacement. With unloaded track a shoulder width of 0.3 m (12 in.) gave a 20% increase in resistance over a non-shoulder situation. This was very important for quantifying effects shoulder designs have on track buckle resistance.

With the development of high speed train, research scope has been expanded to study also the lateral instability due to the lateral wheel-rail negotiating forces. Samavedam et al. (1997) developed a coupled train-track computer model "OMNISIM" to calculate the lateral dynamic force acting on the track and evaluate the lateral stability for high speed

track. Baseline validation studies showed very good agreement between model predictions and test results.

Tie-ballast interaction was studied to be essential to the track lateral stability. Selig and Waters (1994) realized that a decrease of the tie-ballast resistance after tamping caused the track buckle. A Single Tie Push Test (STPT) was proposed and conducted (Samavedam et al. 1995 and Kish et al. 1995) to investigate the lateral stability of both wood and concrete ties on ballast.

From the review of the previous research, it can be concluded that the wheel loading, temperature, rail lateral rigidity, tie-ballast lateral resistance, and even the fastening system connecting the rail and the tie are primary factors affecting the railroad lateral stability. Among them, the tie-ballast lateral resistance is particularly worth investigating and will be studied later in this thesis by using Discrete Element Method (DEM). In addition, methods to improve the tie-ballast lateral resistance such as by the use of textured tie will also be evaluated by DEM.

2.3 Track Settlement

Track settlement is related to the permanent deformation behavior of granular materials under repeated loading. A significant number of laboratory permanent deformation tests have been conducted on pavement base course materials using repeated load triaxial testing. It was concluded that load characteristics (Barksdale, 1971; Barksdale, 1972; Brown and Hyde, 1975; Monismith et al. 1975; Lourens, 1995; Van Niekerk, 2002) and material properties (Haynes and Yoder, 1963; Barksdale, 1972; Allen, 1973; Thom and Brown, 1988; Dawson et al. 1996; Cheung and Dawson, 2002; Rao et al.

2002) were two important factors affecting the permanent deformation behavior of pavement granular base materials.

Barksdale (1972) reported every load cycle to contribute to the accumulation of permanent deformation, resulting in continuous development of permanent axial strain under repeated loading. He suggested that the permanent deformation accumulation was related to the logarithm of the number of load applications given by the following equation:

$$\varepsilon_p = a + blog(N) \tag{2.2}$$

where:

ε_p: Permanent axial strain;

N: Number of load applications;

a, b: Model parameters obtained from regression analysis.

Monismith et al. (1975) suggested the log-log relationship (Equation 2.3) between the number of load applications and permanent strains.

$$\varepsilon_p = aN^b \tag{2.3}$$

where:

ε_p: Permanent axial strain;

N: Number of load applications;

a, b: Model parameters.

El-Mitiny (1980) and Khedr (1985) proposed the strain rate model which inversely correlates the rate of permanent axial strain to the logarithm of the number of load repetitions.

$$\varepsilon_p/N = aN^{-b} \tag{2.4}$$

where:

ε_p: Permanent axial strain;

N: Number of load applications;

a,b: Model parameters.

Thompson and Naumann (1993) used rut depth data obtained from field measurements instead of laboratory obtained axial strains and successfully developed a model (Equation 2.5) to predict the AASHO Road Test section rutting performances.

$$RR = \frac{RD}{N} = aN^b \tag{2.5}$$

where:

RR: Rutting rate permanent axial strain;

RD: Rut depth;

N: Number of load applications;

a, b: Model parameters.

Tseng and Lytton (1989) presented a three-parameter permanent deformation model to predict the accumulation of permanent deformation through material testing. The parameters were developed from the laboratory established relationship between permanent strains and the number of load applications.

Similarly, Ullidtz (1997) also proposed a permanent strain model which considered deviator stress in the formulation (Equation 2.6).

$$\varepsilon_p = a(\frac{\sigma_d}{P_0})^b N^c \tag{2.6}$$

where:

ε_p: Permanent axial strain;

σ_d: Deviator stress;

P_0: Reference stress (atmosphere pressure);

a, b, and c: Model parameters

Werkmeister et al. (2001) used the "shakedown concept" to categorize aggregate permanent deformation performances into three regions: plastic shakedown, plastic creep, and incremental collapse.

Railroad ballast settlement has been less emphasized in the literature. Heath and Shenton (1968) tested Meldon Stone ballast with three gradations in a 229 mm (9 in.) in diameter by 229 mm (9 in.) high triaxial testing apparatus. One of the conclusions was that the initial deformation and the rate of permanent deformation accumulation both depended on the applied stress.

Wong (1974) tested different types of ballast in a rigidly confined repeated load apparatus. He concluded that the permanent strain accumulation was proportional to the logarithm of the number of cycles and was the least for samples compacted to the highest densities. Bishop (1975) extended Wong's tests and concluded that different ballast types yielded different permanent deformation behavior.

Knutson et al. (1977) conducted a comprehensive study on ballast permanent deformation and concluded that compaction condition, stress level, and fine content (finer than 9.5 mm) were the most prominent factors.

Raymond (1979) found that the ballast aggregate hardness was the most significant variable influencing the rate of accumulation of the plastic deformation. The rate of accumulation decreased as the aggregate mineral hardness increased.

Feng (1984) employed a new testing method called "Ballast Box Testing" and concluded that most of the settlement occurred prior to 500,000 cycles. Han and Selig (1996) used the same method to evaluate the effect of fine material on the ballast settlement. They concluded that the particle sizes of the ballast and fouling materials would greatly affect the settlement of the ballast.

Raymond (2002) conducted ballast box tests on both angular and rounded ballast aggregate under geotextile confined conditions. He concluded that geotextiles could significantly decrease the settlement of angular ballast aggregates and even more than rounded ballast aggregates. Raymond (2003) also concluded that the greatest benefit on ballast settlement was obtained when the ratio between geotextile installation depth to the loading foot width was between 0.18 to 0.5 simply related to bearing capacity failure zone. Indraratna et al. (2004) conducted large scale triaxial tests on ballast and concluded that the axial unrecoverable strain decreased with the increasing confining pressure.

2.4 Traditional Track Ballast Modeling Techniques

Due to the advent of microcomputers in the last decade, mechanistic analysis aided by computerized numerical methods such as the Finite Element Method have become widely used in railroad track design. These quasi-static Finite Element programs include: ILLITRACK developed at the University of Illinois (Tayabji and Thompson 1977), GEOTRACK developed by Chang et al. (1980), KENTRACK (Huang et al. 1984 and Rose et al. 2003) and TRACK2 developed by US Corps of Engineers (2002). All these methods are based on classical continuum assumption for the analysis of deflection, stress, and strain within the track-tie-ballast system. Such a continuum solution assumes

the largest horizontal tensile stress at the bottom of the ballast layer which is typically modeled as a bending plate.

Ballast can however only take limited amount of tensile stresses in the form of friction between particles under confinement. Selig (1987) proposed that those assumed tensile stresses are actually offset by compaction induced residual stresses which are locked in the granular layer. Tutumluer (1995) employed a block model to simulate the aggregate layer in pavement granular bases. He used realistic properties obtained from direct shear test to model the particulate medium and found that the load transfer in granular materials was maintained by shear and normal compressive stresses at block interfaces since tensile stresses could not occur.

Most traditional methods based on continuum analysis cannot simulate track fouling and settlement in a satisfactory manner. The interactions among ballast aggregate particles are mostly discontinuous. New modeling techniques need to be employed for studying ballast behavior.

2.5 Discrete Element Modeling

Discrete Element Methods are numerical procedures to solve problems that exhibit gross discontinuous behavior. These methods are able to analyze multiple interacting bodies undergoing large dynamic movements. By modeling the individual particles and computing their motion, the overall behavior of the granular assembly, which may include unrecoverable deformations, dilation, post-peak behavior, and anisotropy, is modeled implicitly. Interaction of granular materials or rock masses can this way be

modeled accurately and realistically since any discontinuous detail can be included in the analysis.

Discrete Element Methods have been widely applied to the soil and rock mechanics. In early 1970's, Cundall (1971) introduced the first computer program to model the progressive failure of a discrete block system. The interaction between blocks was governed by friction and normal stiffness. There was no limit to the amount of displacement or rotation of each block whenever blocks were touching or separated. It was designed for rigid body motion problems which were at that time impossible to be solved by finite element techniques. Cundall also described the basic theory of DEM, i.e., force-displacement law, law of motion, and computation cycles with time steps.

The DEM method was next applied to model the granular assemblies by Cundall and Strack (1979) to simulate the particle contact force distributions in the assemblies. This granular medium was composed of distinct particles which displaced independently from one another and interacted only at contact points. A computer program called BALL was developed by integrating the calculation cycle, force displacement law, law of motion and damping effects. BALL was then used to validate the DEM method by comparing force vector plots with those obtained from the photo-elastic analysis. Good agreement was found between these two results. Cundall and Strack concluded that DEM and the program BALL were valid tools studying the behavior of granular assemblies. Later, BALL was applied by Cundall and Strack in investigating the behavior of disc assemblies under loading and unloading. Tests with 100 and 1000 discs were performed with computer interactive graphics to study the internal mechanism within a granular mass and

the response to stress probes. Figure 2.1 shows the initial state of the 100-disc test by Cundall and Strack (1979).

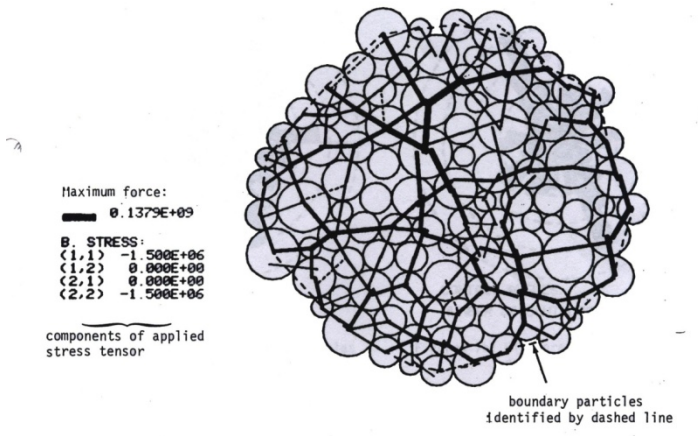

Figure 2.1 Initial State of 100-disc Test (Cundall and Strack, 1979)

DEM was further developed in the early 1980's by Cundall, Drescher, and Strack to introduce the methodologies of measuring and observing granular assemblies using the BALL simulation. Their work was divided into three parts. First, boundary conditions and average stresses and strains were defined. Then, they focused on the microscopic behavior and mechanisms observed in numerical simulations. The last part emphasized the measurement and interpretation of continuum quantities for an assembly of particles.

In the late 1980's, Cundall improved the computer program BALL to a 3D version called TRUBAL (Cundall, 1988). He used TRUBAL to perform a simulation on dense spherical assemblies. The numerical simulation results agreed well with the test results described by Ishibashi et al. (1988), except for the volume strain measured from tri-axial tests.

Thorton et al. (1986) described a modified version of BALL, called GRANULE. This code is capable of modeling the fracture of an agglomerate of spherical balls bonded

together. In their model, they attributed a surface energy to the balls in the agglomerates so that tensile forces between balls were defined as auto-adhesive.

After realizing the limitation of spherical element shape, Barbosa and Ghaboussi (1990) developed a new program called "BLOCKS3D" which utilized arbitrarily shaped elements instead of spherical elements. Block shaped elements are more realistic than spherical elements especially in modelling crushed particles like railroad ballast aggregates.

Nezami et al. (2004) proposed a fast contact detection algorithm called "Fast Common Plane" for 3D block shaped discrete elements. With this advanced algorithm, a 3D discrete element analysis code "DBLOCK3D" was developed (Hashash et al. 2005) for the simulation of granular media and soil-machine interaction. According to the ongoing research, Nezami et al. (2006) developed the "Shortest Link Method" to search the common plane. Zhao et al. (2006) implemented this algorithm to DBLOCKS3D and developed a modified DEM code "BLOKS3D". Nezami et al. (2007) successfully utilized "BLOKS3D" to simulate a bucket-soil interaction model.

2.5.1 Theory of DEM

Discrete element methodology models dynamic interactions of aggregate particles in a granular assembly. Each particle in this discontinuous medium is modeled as an individual element. Force displacement law and the law of motion govern the movement and contact of each element. Since, in most cases, elements are assumed to be rigid, compression of two elements contacting each other is represented by overlapping. The contact forces and displacements of elements are computed by tracing the movements of

the individual particles. This dynamic behavior is represented numerically by a time-stepping algorithm in which it is assumed that the velocities and accelerations are kept constant within one time step.

The DEM procedure includes three major operations: (1) computation of element contact forces; (2) computation of particle motion; and (3) detection of contacts, as shown in Figure 2.2.

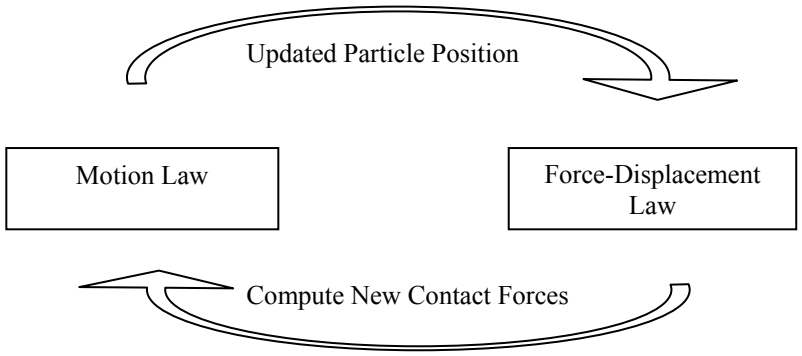

Figure 2.2 Calculation Cycle in DEM (ITASCA, 1999)

The force-displacement law is applied to all contacts. It relates the relative displacement between two elements in contact to the contact force acting on each element. The law is applied at the start of each cycle to obtain the new contact force. The contact force vector F_i is resolved into normal and shear components with respect to contact plane as:

$$F_i = F_i^n + F_i^s \tag{2.7}$$

where F_i^n and F_i^s denote normal and shear component vectors, respectively. The normal contact force vector is described as:

$$F_i^n = K^n U^n n_i \tag{2.8}$$

where K^n = normal stiffness at contact,

U^n = overlapping displacement magnitude of two contacting entities and

n_i = the unit normal vector.

Depending on the element type used, the normal vector can be oriented differently; some are directed along the line between particle centers such as in spherical elements, some are perpendicular to the common plane like in block elements which will be further explained.

To compute the shear contact force, more complicated calculations are performed in an incremental fashion. The shear contact force is initialized to zero when a contact is formed. Each subsequent relative shear displacement causes an incremental shear force to be developed. The incremental shear force is then calculated using:

$$\Delta F_i^s = -K^s V_i^s \Delta t \tag{2.9}$$

where K_s = the shear contact stiffness,

V_i^s = the shear component of contact velocity and

Δt = the time step.

The total shear force is then calculated by summing the shear force vector at the previous time step with the incremental elastic shear force vector:

$$F_i^s = \left\{F_i^s\right\}^{current} + \Delta F_i^s \tag{2.10}$$

As such, the shear force $\left\{F_i^s\right\}^{current}$ is updated in every time step by taking into account the motion due to contact. These updated contact forces (and moments) are then used in the following time step to calculate the acceleration using Newton's second law, which is integrated to give velocity and displacement and the updated position of the element.

The motion of a rigid particle is determined by the resultant force and moment vector acting upon it, which are described in terms of translation and rotation of the particle. The equation of motion is expressed as two vector quantities; one relates the resultant force to the translational motion, and the other relates the resultant moment to the rotational motion of the particle. The equation for translational motion is written in vector form as follows:

$$F_i = m(\ddot{x}_i - g_i) \tag{2.11}$$

where: F_i = Sum of all externally applied forces acting on the particle;

m = Total mass of the particle,

$\ddot{x}_i$ = Acceleration of particle,

g_i = Body force acceleration vector (e.g., gravity loading).

The equation for rotational motion is also written in the vector form as follows:

$$M_i = I\dot{\omega}_i \tag{2.12}$$

where: M_i = Resultant moment acting on particle,

I = Moment of inertia of a particle,

$\dot{\omega}_i$ = Angular acceleration of a particle.

The equations of motion, given by Equations 2.11 and 2.12 are integrated using a centered finite difference procedure involving a time step of Δt. The quantities $\dot{x}_i$ and ω_i are computed at the mid-intervals of t ± n Δt/2, while the quantities x_i, $\ddot{x}_i$, $\dot{\omega}_i$, F_i, and M_i are computed at the primary intervals of t ± nΔt. The translational and rotational accelerations at time t are calculated as

$$\ddot{x}_i^{(t)} = \frac{1}{\Delta t}\left(\dot{x}_i^{(t+\Delta t/2)} - \dot{x}_i^{(t-\Delta t/2)}\right) \tag{2.13}$$

$$\dot{\omega}_i^{(t)} = \frac{1}{\Delta t}\left(\omega_i^{(t+\Delta t/2)} - \omega_i^{(t-\Delta t/2)}\right) \tag{2.14}$$

Translational and rotational velocities at time (t+Δt/2) can be solved by inserting Equations 2.13 and 2.14 into Equations 2.11 and 2.12, respectively. Hence,

$$\dot{x}_i^{(t+\Delta t/2)} = \dot{x}_i^{(t-\Delta t/2)} + \left(\frac{F_i^{(t)}}{m} + g_i\right)\Delta t \tag{2.15}$$

$$\omega_i^{(t+\Delta t/2)} = \omega_i^{(t-\Delta t/2)} + \left(\frac{M_i^{(t)}}{I}\right)\Delta t \tag{2.16}$$

Finally, the position of the particle center is updated by using velocities as follows:

$$x_i^{(t+\Delta t)} = x_i^{(t)} + \dot{x}_i^{(t+\Delta t/2)}\Delta t \tag{2.17}$$

The calculation cycle for the law of motion is summarized as follows. Given the initial particle speed $\dot{x}_i^{(t-\Delta t/2)}, \omega_i^{(t-\Delta t/2)}$, the initial force $F_i^{(t)}$ and moment $M_i^{(t)}$, Equations 2.15 and 2.16 are used to obtain the speed at the next time interval $\dot{x}_i^{(t+\Delta t/2)}, \omega_i^{(t+\Delta t/2)}$. Then, the speed $\dot{x}_i^{(t+\Delta t/2)}$ and the initial displacement $x_i^{(t)}$ are used in Equation 2.17 to obtain new displacement $x_i^{(t+\Delta t)}$. From $x_i^{(t+\Delta t)}$ the force and moment components $F_i^{(t+\Delta t)}$ and $M_i^{(t+\Delta t)}$ are updated, and the iterations are continued as shown in Figure 2.3.

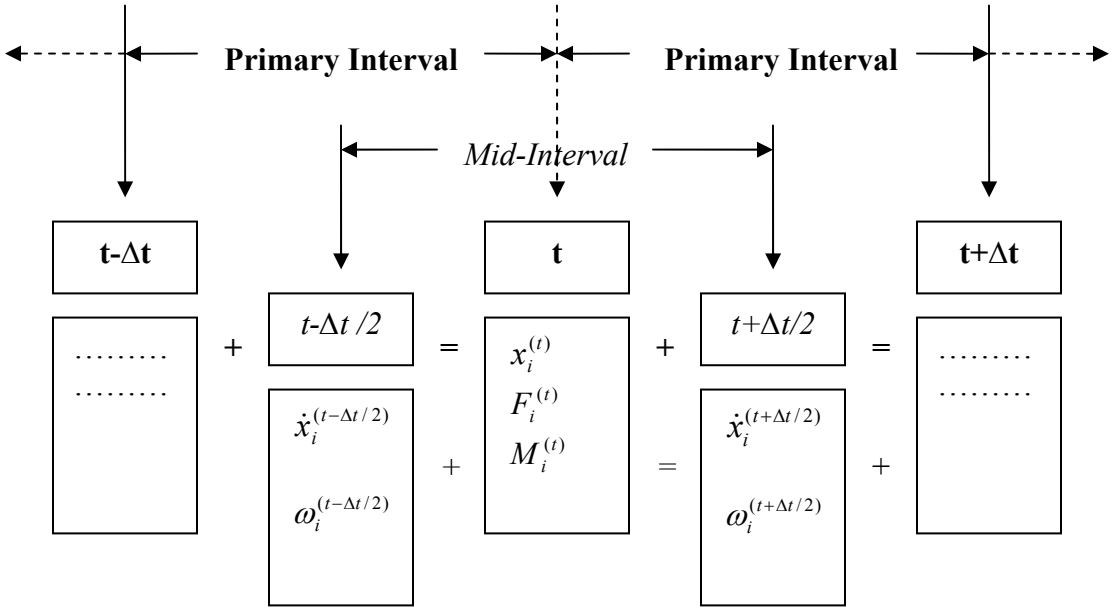

Figure 2.3 Law of Motion Calculation Flow Chart (ITASCA, 1999)

2.5.2 Contact Detection Schemes

In the DEM procedure, at every time step, some elements will come into contact and some will separate. It is necessary to keep performing contact detection throughout the whole analysis. For elements with shape describable by a function, such as spherical or elliptical contact detection can be performed analytically. For example, for the spherical element, two elements are considered in contact if the distance between two centers is equal to or smaller than the sum of the radii of these two elements. However, for arbitrary shape elements, contact detection is generally much more complex.

Fast Common Plane

Common plane was defined as "a plane that bisects the space between the two contacting particles". It was introduced by Cundall and Hart (1992). It has a two-stage

procedure to find the common plane. The first step is specifying one point (between two particles) on the common plane; the second stage is an iterative process in which a plane is rotated around this point until the biggest gap is reached. The plane with the biggest gap is the common plane. If two particles were in contact, both of them should intersect the common plane. By using common plane, the particle-to-particle contact detection problem was transformed to a much faster plane-to-particle contact detection problem.

Nezami et al. (2004) proposed a new Fast Common Plane approach to obtain the common plane for 2D and 3D particles. By this new approach, a common plane can be easily identified by checking only 5 candidates. This approach is briefly explained in 2D mode as follows.

When two particles are not in contact, the Fast Common Plane approach has to meet two requirements:

1. A common plane has to completely separate these two particles;
2. As shown in Figure 2.4, once a plane separates the two particles completely, the closest vertex to the plane of particle A and B and respective distances a and b can both be found. The common plane is the plane that has the same a and b value and the maximum sum of a and b.

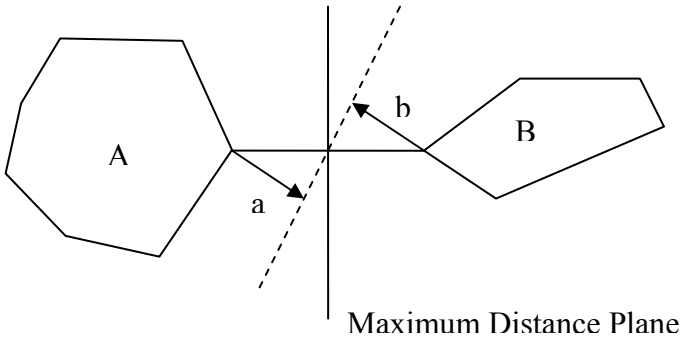

Figure 2.4 Definition of Common Plane (Cundall and Hart, 1992)

If, in one time step, a or b becomes 0 or a very small value, these two particles are considered to be actually in contact.

The basic procedure to determine the common plane includes 5 steps:

1. Connect the two particles center of gravities and find the mid-point G of this connection (Figure 2.5a).

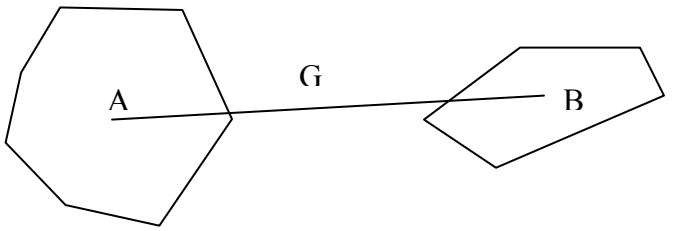

Figure 2.5a Connected Center of Gravities of Two Particles

2. Draw a plane which is perpendicular to the connection of two center of gravities through the mid-point G; and find the closest vertex to the perpendicular plane of particle A and particle B (Figure 2.5b).

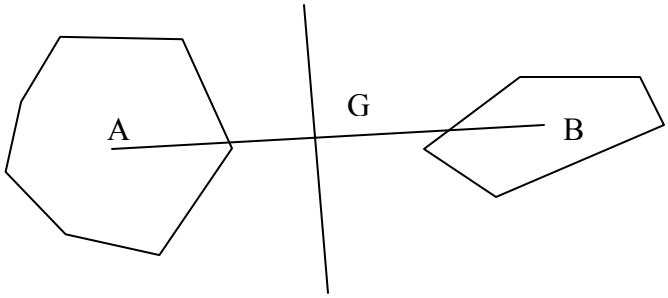

Figure 2.5b A Plane Perpendicular to the Connection of Center of Gravities

3. Connect these two vertices and draw normal line of this connect through the mid-point M (Figure 2.5c).

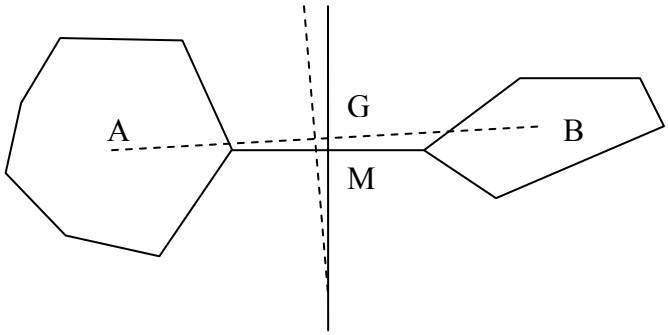

Figure 2.5c A Plane Perpendicular to the Connection of Two Closest Vertices

4. Draw lines through M which are parallel to the four closest edges to these two vertices (Figure 2.5d).

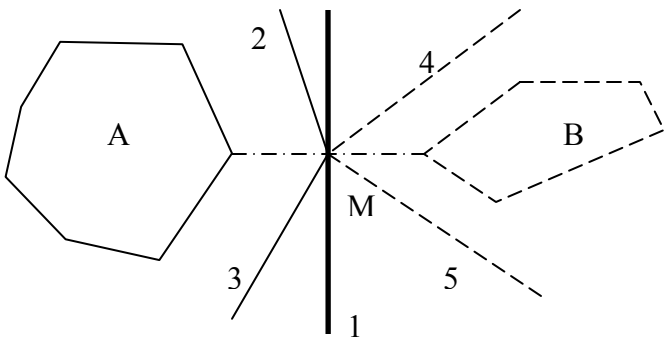

Figure 2.5d Five Common Plane Candidates (Nezami et al. 2004)

5. The common plane is one of these five planes. If line 1 is in between line 3 and 5, and also 2 and 4, then the common plane is line 1. Otherwise, the common plane is one of 2, 3, 4, or 5 depending on the distance to the vertex.

For two particles that are already in contact, BLOKS3D will artificially pull them apart and then use the same method to detect contact. This Fast Common Plane algorithm was proven to be fast and accurate by Nezami et al. (2004). Nezami et al. (2006) also proposed "Shortest Link Method" to search the "common plane", which has been proven to be even faster in terms of contact detecting.

2.5.3 Major DEM Model Parameters

BLOKS3D is chosen as an example to explain the major model parameters used in DEM which are: (1) element shape, size, and gradation; and (2) parameters describing contact between two elements. Element shape, size, and gradation can be well captured and characterized by using an image analysis device such as the University of Illinois Aggregate Image Analyzer (UIAIA) to be discussed later. The contact between two

elements in BLOKS3D (Figure 2.6) consists of three parts: (1) normal spring which controls the relationship between normal contact force and the total relative displacement perpendicular to the common plane; (2) shear spring which controls the relationship between incremental shear contact force and the movement parallel to the common plane; and (3) the surface friction angle which acts as a frictional slider and supplies friction between two elements in contact. The surface friction angle also serves as a trigger for two elements to start sliding against each other when the shear contact force exceeds the product of normal contact force and the tangent of surface friction angle. The major parameters: normal spring (normal contact) stiffness (Kn), shear spring (shear contact) stiffness (Ks), and the surface friction angle (θ) need to be extensively studied for their effects on DEM simulation results. For the purpose of sensitivity analysis to be conducted in the next chapter, the following literature review supplies some basic theoretical background.

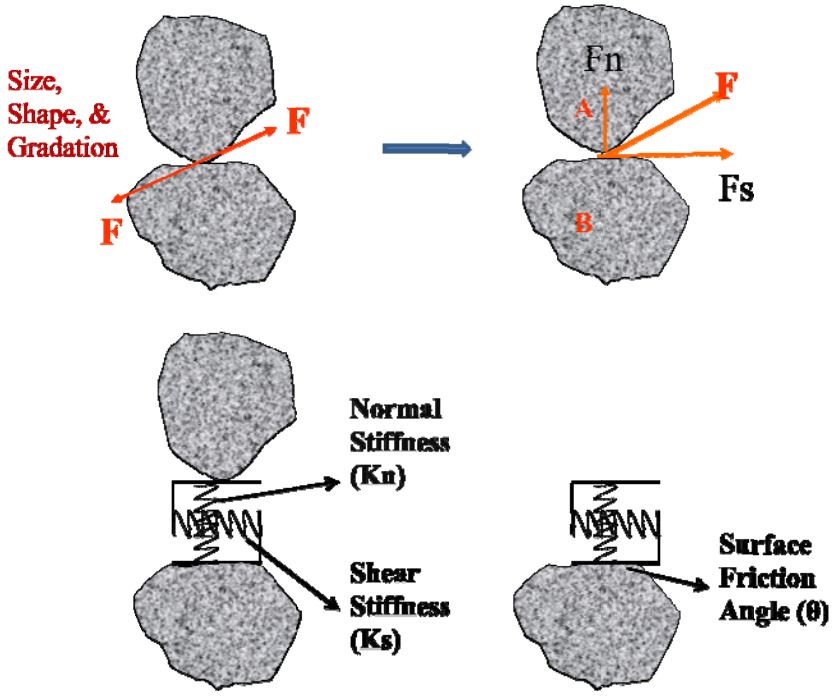

Figure 2.6 Major DEM Model Parameters

Contact Stiffness

Contact stiffness in DEM relates contact force to particle movement. Although contact stiffness for a few scenarios can be mathematically derived (Hertz 1895; Kalker 1990; Johnson 1987), contact stiffness in numerical solutions, such as a DEM simulation, has not been studied extensively because of its complexity.

Contact stiffness determination starts with the problem of semi-infinite plane subjected to normal and shear forces as shown in Figure 2.7a. This problem was first solved by Flamant in 1892, and is treated in Timoshenko and Goodier (1951). Based on Flamant's solution, the situation of semi-infinite plane subjected to arbitrarily distributed force (Figure 2.7b) can also be solved (Hills et al, 1993). Of particular relevance are the surface displacements which are obtained by Equations 2.18 and 2.19. For convenience, displacement functions are given as derivatives.

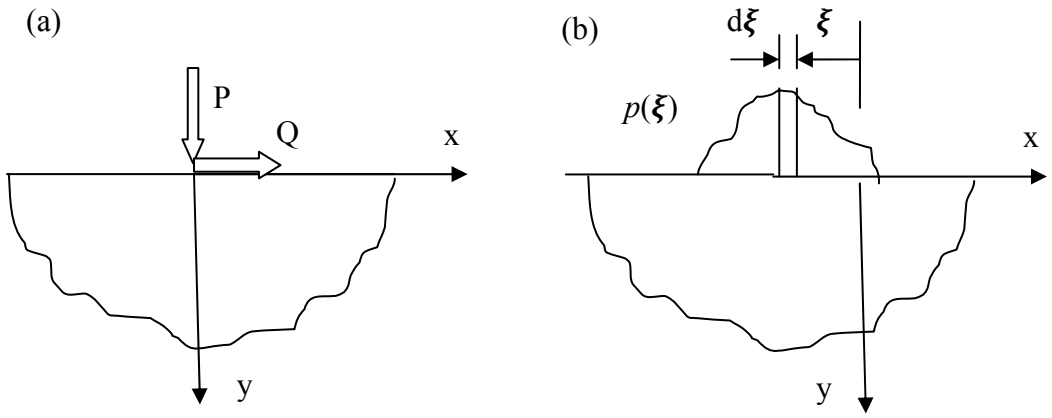

Figure 2.7 Force Acting on "Semi-infinite Plane"

$$\frac{\partial u}{\partial x} = \frac{k-1}{4\mu} p(x) + \frac{k+1}{4\mu\pi} \int \frac{q(\xi) d\xi}{x-\xi} \tag{2.18}$$

$$\frac{\partial v}{\partial x} = \frac{k+1}{4\mu\pi} \int \frac{p(\xi) d\xi}{x-\xi} - \frac{k-1}{4\mu} q(x) \tag{2.19}$$

where: u, v are horizontal and vertical displacements respectively; $k = (3-\nu)/(1+\nu)$ for plane stress and $k = (3-4\nu)$ for plane strain; ν is Poison's ratio; μ is the Lame constant and $\mu = E/2(1+\nu)$; and p and q are normal and shear contact force functions of these two objects in contact.

When two objects are in contact, assuming the solutions still apply, one object can be treated as force profile acting on another object. The following equations give vertical deformation at contact surface.

$$\frac{\partial v_1}{\partial x} = \frac{k_1+1}{4\mu\pi} \int \frac{p(\xi) d\xi}{x-\xi} - \frac{k_1-1}{4\mu} q(x) \tag{2.20}$$

$$\frac{\partial v_2}{\partial x} = -\frac{k_2+1}{4\mu\pi} \int \frac{p(\xi) d\xi}{x-\xi} - \frac{k_2-1}{4\mu} q(x) \tag{2.21}$$

As the two bodies are pressed together deformation must occur so that the deformed bodies will conform within the contact. In the unloaded state, if two bodies interpenetrate freely into each other, so that the amount of overlap are given by function h(x) (see Figure 2.8) within the contact patch, the relative compressive displacements of surface, i.e. $v_1(x) - v_2(x)$ must be equal to the degree of overlap. So, from Equations 2.20 and 2.21, the following can be derived (Hills et al, 1993):

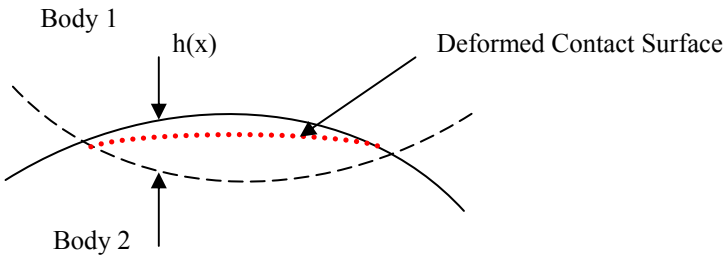

Figure 2.8 Two Objects in Contact

$$\frac{1}{A}\frac{\partial h}{\partial x} = \frac{1}{\pi}\int \frac{p(\xi)d\xi}{x-\xi} - \beta q(x) \tag{2.22}$$

where:

$$A = \frac{k_1 + 1}{4\mu_1} + \frac{k_2 + 1}{4\mu_2} \tag{2.23}$$

$$\beta = \frac{\mu_2(k_1 - 1) - \mu_1(k_2 - 1)}{\mu_2(k_1 + 1) + \mu_1(k_2 + 1)} \tag{2.24}$$

Inverting Equation 2.22 gives the relationship between contact normal stress and the normal displacement, which eventually constructs the contact stiffness. Two special cases are reviewed as typical "Frictionless Elastic" contact scenarios. "Frictionless" means there is no shear traction to arise during contact which is assumed to assure the derived analytical solution.

Contact of Spheres (Hertzian Contact)

A spherical surface may be idealized as a rotated parabola provided that the radius of contact area is small compared to the radius of curvature of the contact spheres. The overlap function can thus be described in axisymmetric coordinates as:

$$h(r) = d - \frac{Kr^2}{2} \tag{2.25}$$

where: d is the maximum magnitude of normal overlap and $K = \frac{1}{R_1} + \frac{1}{R_2}$, R_1 and R_2 are the radii of contact spheres (see Figure 2.9), respectively.

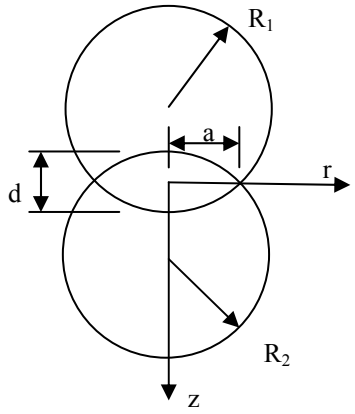

Figure 2.9 Hertzian Contact between Two Spheres

Axisymmetrically distributed force acting on semi-infinite plane can be solved by Potential Theory (Love, 1927) in axisymmetric coordinates and the transformation of displacement can be expressed as (Hills et al, 1993):

$$h^t(r) = A\int_r^a \frac{sp(s)ds}{\sqrt{s^2 - r^2}} \tag{2.26}$$

where "a" is the radius of contact area, "p" is the function of normal contact pressure.

The transformation of the assumed displacement from Equation 2.25 is:

$$h^t(r) = \frac{d}{dr}\int_0^r \frac{s(d - \frac{Ks^2}{2})ds}{\sqrt{r^2 - s^2}} \tag{2.27}$$

Accordingly, Equations 2.26 and 2.27 have to be equal:

$$-A\int_r^a \frac{sp(s)ds}{\sqrt{s^2 - r^2}} = d - \frac{Kr^2}{2} \tag{2.28}$$

By inverting Equation 2.28 (Barber, 1983) and expressing the normal contact pressure as the total normal contact force: $p = \int_0^a 2\pi rp(r)dr$, Equation 2.29 (Hills et al, 1993) can be derived for the relationship between normal contact force and normal contact displacement.

$$d = \sqrt[3]{\left(\frac{9A^2K}{64}\right)P^2} \tag{2.29}$$

where d is the maximum magnitude of normal overlap; A is the parameter calculated from Equation 2.23; $K = \frac{1}{R_1} + \frac{1}{R_2}$, R1 and R2 are the radii of contact spheres (see Figure 2.9), respectively; and P is the contact force between two particles.

Contact between Cone and Plane

The contact between a cone and a plane (see Figure 2.10) can be treated by the same procedure as Hertzian contact. The following overlap function is assumed to describe the cone and plane contact.

$$h(r) = d - \lambda r \tag{2.30}$$

where d is the maximum overlap between the cone and the plane and λ is the angle between cone and plane (see Figure 2.10) which needs to be small.

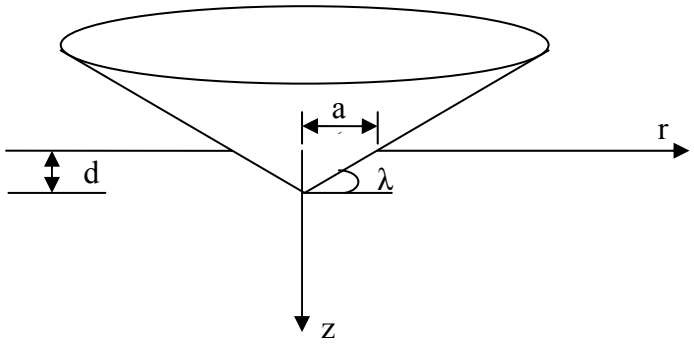

Figure 2.10 Cone on Plane Contact

The normal displacement and normal force relationship can then be expressed as (Hills et al. 1993):

$$d = \sqrt{\frac{PA\theta\pi}{8}} \tag{2.31}$$

Surface Friction Angle

In reality, aggregates within an assembly have very complicated movements; sliding and rolling may take place at the same time. Both of these two modes will lead to failure. If the rolling resistance of the aggregate is high, such as for an angular aggregate, sliding will happen first in which case the surface friction angle plays a major role on the strength. However, when the surface is rough, i.e., the surface friction angle is so high

that sliding is much more difficult than rolling, the particle weight and shape properties will dominate over the surface roughness resulting in the movement of rolling over.

Surface friction angle can be determined in the laboratory by a method described in Marsal's (1973) work. A rock with a nominal diameter of 5 to 7 cm is cast in a concrete cube (see Figure 2.11), 15 cm one side. The cube is cut in half with a diamond saw and a thin layer is removed so that the rock particle surface protrudes. Normal forces are applied as shown in Figure 2.11 followed by shear displacement. The surface friction angle can thus be obtained by dividing the normal force by the peak shear force.

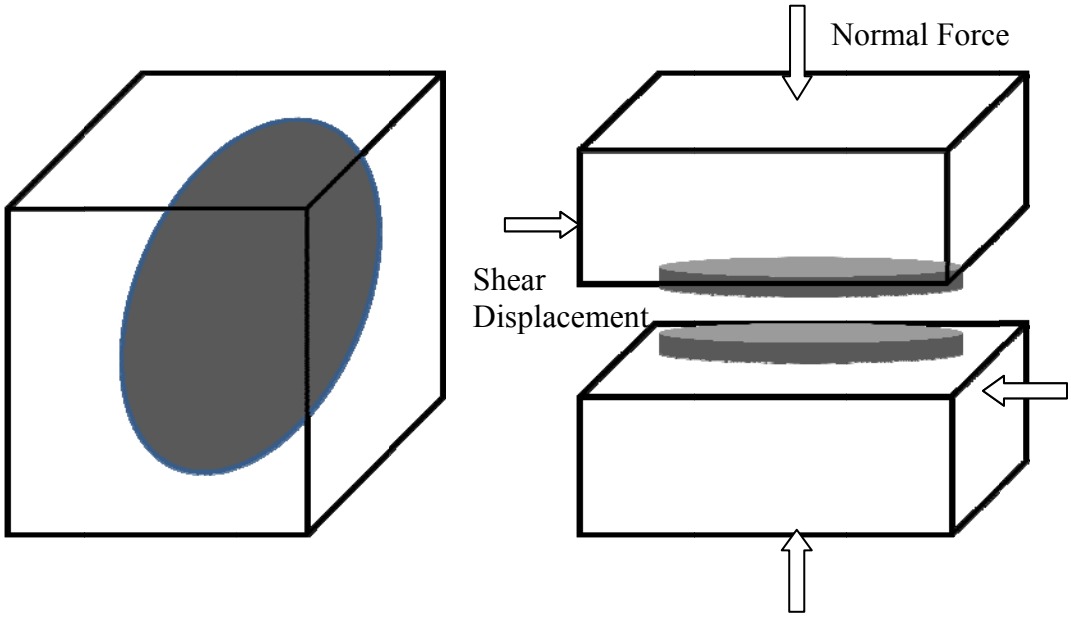

Figure 2.11 Experimental Approach to Determine Surface Friction Angle of an Aggregate (Marsal, 1973)

Marsal (1973) suggested that the surface friction angle for granitic-gneiss, when experiencing normal stress within the range used in this study (160~400 kPa), falls in the range of 26 to 35 degrees.

2.6 Aggregate (Element) Shape Effects

The DEM approach with user defined arbitrary element shapes offer a new perspective to study aggregate shape effects on assembly performance. Shape of the ballast aggregate is one of the most important factors to affect ballast strength, workability, and stability. However, compared to particle gradation and air voids, the influences of aggregate shape properties on aggregate assembly strength, stability, and deformation characteristics have received less attention and have not been thoroughly investigated by means of quantifying individually the effects of aggregate morphological properties. Vallerga et al (1957) proposed that aggregate shape would have a major impact on material strength depending on how different materials are compacted. Koerner (1968) found internal friction angles of cohesionless soils to vary inversely with particle sphericity. Marsal (1973) evaluated aggregate shape properties based on a statistical method. Holubec and Appolonia (1973) conducted triaxial tests and observed particle angularity to positively influence strength of granular materials. Also, research work by Santamarina and Cho (2004) indicated particle shape had a major influence on soil behavior. Han (1998) developed a computer model to evaluate the effect of aggregate shape on railroad ballast performance based on large amounts of test data.

Efforts have been made in pavement engineering to correlate aggregate physical and structural layer properties to overall performance. Early researchers (Herrin and Goetz, 1945) found shapes of aggregates within hot mix asphalt had only minor effects. A study undertaken by Monismith (1970) concluded that aggregate shape and surface texture characteristics had a considerable influence on the fatigue and stiffness characteristics of

asphalt mixtures. Laboratory studies based on the Marshall Mixture design procedure suggested that the use of crushed gravel over natural gravel significantly improved the stability of the hot mix asphalt (Benson, 1970). Further, it was also concluded that the use of crushed stone instead of gravel could increase the stability of the mix by as much as 45 percent (Benson, 1970). Yeggoni et al. (1994) noted a significant influence of aggregate size, shape and surface texture on the rutting resistance of asphalt concrete and underlying layers. Barksdale et al. (1992) indicated that using a coarser asphalt mixture reduced rutting in the base, asphalt binder, and surface courses by approximately 23, 14, and 13%, respectively.

Aggregate shape properties have also been found to influence Portland Cement Concrete (PCC) strength properties. Mixes containing angular particles produced higher strength and modulus values compared to PCC samples with gravel (Choubane et al., 1996). It is however interesting to note that this is somewhat in contradiction with the traditional recommendation to use rounded gravel with minimal surface areas for reduced paste requirement to cover the particle completely (Mindess and Young, 1981). The use of angular particles in PCC mixes would, however, increase the unit cost of the mix due to crushing costs and increased paste requirements.

In the base courses, while compaction is important from a shear resistance and strength point of view, the shape, size and texture of coarse aggregates are also important in providing stability (National Stone Association, 1991). Field tests of conventional asphalt pavement sections with two different base thicknesses and three different base gradations showed that crushed-stone bases gave excellent stability because of a uniform, high degree of density and little or no segregation (Barksdale, 1984). Rounded river

gravel with smooth surfaces was found to be twice as susceptible to rutting compared to crushed stones (Barksdale and Itani, 1989).

A particle index test was proposed (Huang, 1962; Huang et al., 1963; and Huang et al., 1964) to account for combined aggregate shape effects including parameters such as, shape, texture and angularity. The test provides an index value to evaluate combined aggregate morphological characteristics. This method has been used to indicate the effects of these characteristic on the compaction and strength characteristics of soil-aggregate and asphalt concrete mixtures.

Rao et al. (2002) utilized "University of Illinois Aggregate Image Analyzer (UIAIA)" to evaluate aggregate shape and proposed a shape index "Angularity Index (AI)" to describe the angularity of aggregates. They concluded that aggregates with higher AI usually correspond to higher shear strength.

Not only angularity but also flat and elongated (F&E) ratio of aggregate is used to check if particles have undesirable shapes that might negatively affect mechanical properties of the railroad ballast. The standardized ASTM D4791 test for flat, elongated, or flat and elongated particles, was adapted from the original U.S. Corps of Engineers Method CRD-C 119 test, and is performed on particles retained on the No. 4 sieve. Puzinauskas (1964) showed that AC samples displayed a fair amount of anisotropic properties with the presence of flat particles. However, the effects of particle alignment became less pronounced as the size of the particles was reduced. Subsequent test results (Li and Kett, 1967) verified that the strength of asphalt mixes was adversely affected when they contained coarse aggregate particles with length to width ratios greater than 3.

Inclusion of more than 30-40% of particles with length to width ratios greater than 3:1 caused undesirable mix properties.

Pan et al. (2005) concluded that asphalt mixtures made up of rough surfaced aggregates gave higher resilient moduli than those asphalt mixtures with smooth surfaced aggregates. Pan (2006) discovered that aggregate surface texture had a dramatic impact on aggregate assembly permanent deformation. By implementing the surface texture index concept obtained from UIAIA, Pan (2006) concluded that aggregates with rough surfaces i.e., higher surface texture index, significantly increased rutting resistance.

2.7 Digital Image Technologies

Depending on the most important sensory inputs to the human perceptual system, vision aided intelligent tools for improving production efficiency draws most of the attention in human's efforts to explore the unknown world. Engineers have investigated ways to make these tools capable of accurate interpretation of image inputs. Application of image analysis in the different fields of civil engineering can be tracked back to the 1980s in the pavement distress data collection (Cable and Marks, 1990), investigation of soil and rock properties (Raschke, 1998; Glaser and Haud, 1998), microstructure of asphalt concrete (Yue et al., 1995; Masad et al., 1998; Masad et al., 1999) and Portland Cement Concrete (Bentz and Garboczi, 1996). Image analysis techniques have also been combined with other tools such as finite element analysis (Kose et al., 2000) and artificial intelligence techniques (Chang et al., 2000). A hybrid model was developed based on image analysis and neural network modeling to provide reliable, consistent and objective quality assessment of steel bridge coating corrosion and further, to determine the extent

of rehabilitation required (Chang et al., 2000). Research in fine aggregate shape analysis is also actively pursued (Wilson et al., 1997; Masad et al., 2001).

As an application of the imaging technology, imaging based morphology analysis has been pursued for almost a decade to quantify the shape, angularity and texture of coarse aggregate particles. Digital image equipment and computer algorithms were developed to analyze images to estimate the desired information: dimensions and sizes of aggregate, shape, texture, angularity and gradation. Tutumluer et al. (2001) developed an image analysis device, University of Illinois Aggregate Image Analyzer (UIAIA), to analyze aggregate shape and size properties. NCHRP 4-30A (Masad et al. 2004) identified UIAIA as one of the two promising systems to use in the assessment of aggregate morphology.

The UIAIA uses 3 cameras to collect individual aggregate particle images from three orthogonal directions and in essence captures an "actual" 3D view of each aggregate particle (see Figure 2.12). The choice of using 3 cameras to collect the front, top and side views was to provide the unique capability of determining accurately the volume of each particle. Figure 2.13 shows a schematic of the UIAIA illustrating the operating principle and the various components of the UIAIA. Particles to be analyzed are continuously fed on to a conveyor belt system, which carries them towards the orthogonally positioned cameras. As the individual particles travel along the conveyor, each particle comes into the field of view of a sensor that detects the particle and immediately triggers the cameras. Once triggered, the three synchronized cameras capture the images of the front, top, and side views of the particle. There is a small time delay between the detection of the particle by the sensor and the actual image acquisition. This allows enough time for the particle to move into the field of the three camera views. The captured images are

then processed using software developed specifically for this application and the needed size and shape properties are determined.

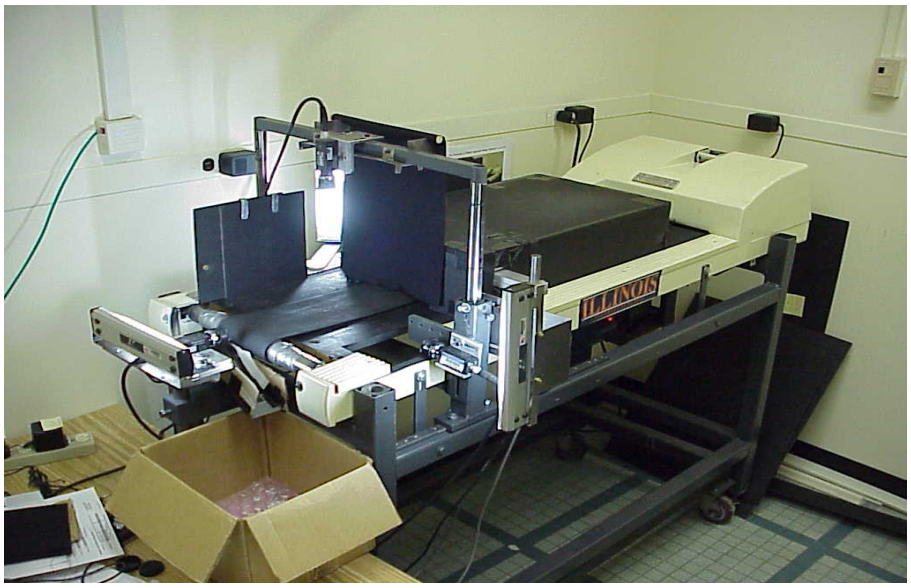

Figure 2.12 Photo of the University of Illinois Aggregate Image Analyzer (UIAIA)

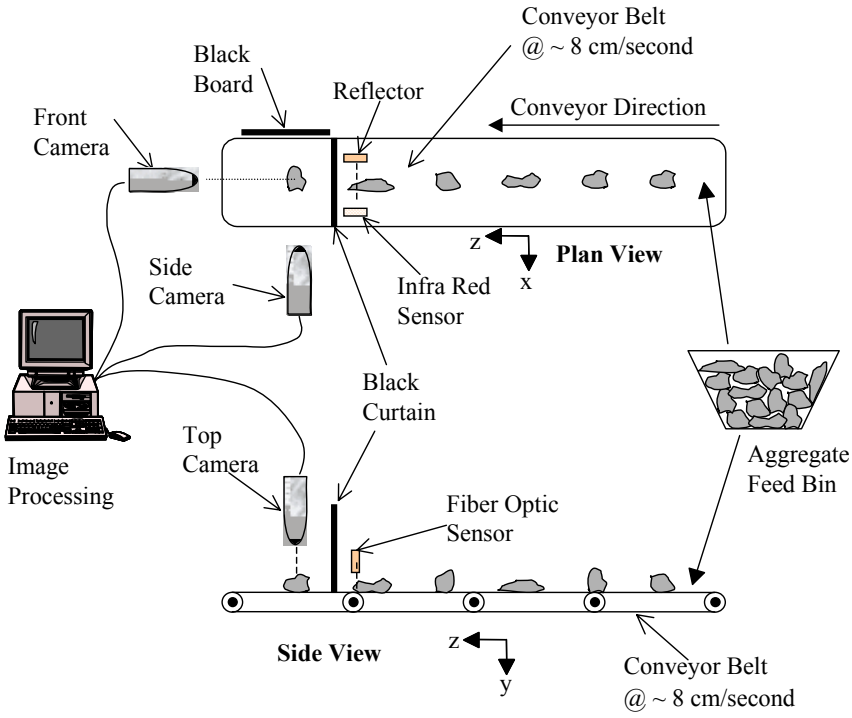

Figure 2.13 Schematic of the University of Illinois Aggregate Image Analyzer

Coarse aggregate particle shape indices defined by the UIAIA system include the Flat and Elongated Ratio (F&E Ratio), Angularity Index (AI) and Surface Texture (ST) Index. These three indices were developed to represent the three key morphological descriptors of coarse aggregate materials as the shape or form, angularity and surface texture as shown in Figure 2.14. Each one characterizes a different aggregate morphological property at a different magnification level linked to the overall aggregate mechanical behavior. The UIAIA image analysis modules, each developed individually as a Labview Virtual Instrument (VI) with a set of unique algorithms, are executed through the Labview IMAQ Vision analysis software to determine these three key shape indices. A description of each imaging based shape index is given in the following paragraphs.

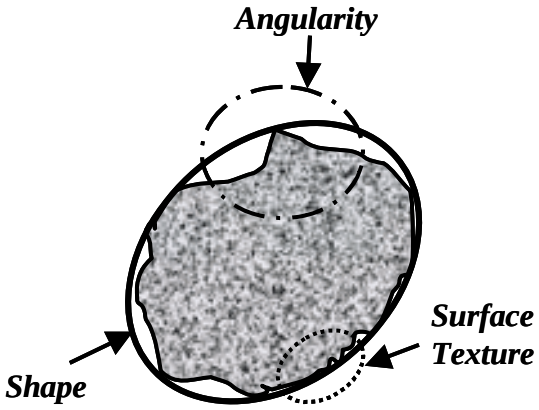

Figure 2.14 Three Key Morphological Descriptors of Coarse Aggregate Particles

Flat and Elongated Ratio

Flat and elongated particles have a general tendency to break during construction and under traffic loads, therefore, cubical and angular particles are commonly preferred. The flat and elongated (F&E) ratio is defined as the ratio of the longest dimension of the particle to its minimum dimension. In the standard manual test procedure, a proportional caliper is used to determine the maximum to minimum dimensional aspect ratios as 2:1, 3:1, and 5:1 (ASTM D 4791-99). The minimum dimension is often measured in a direction that is considered perpendicular to the longest dimension based on the operator's visual judgment.

In analyzing the UIAIA captured images, a similar approach was adopted for determining the longest and the shortest dimensions from the image (see Equation 2.32). The particle is analyzed for the longest dimension and the shortest dimension, which is perpendicular to the longest dimension, from each view of the 3-camera front, top, and

side images. Also discussed by Rao et al. (2001), the ratio of the longest dimension to the shortest finally gives the desired F&E ratio as illustrated in Figure 2.15.

$$F\ \&\ E\ Ratio = \frac{Longest\ Dimension}{Shortest\ Perpendicular\ Dimension} \tag{2.32}$$

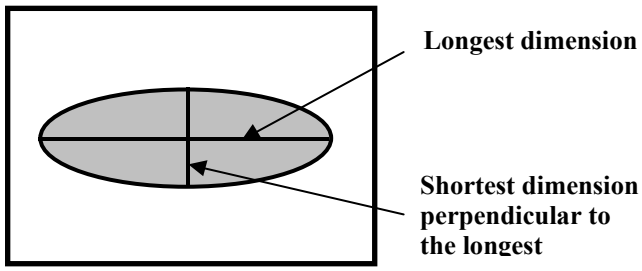

Figure 2.15 Illustration of the Longest and Shortest Perpendicular Dimensions

Angularity Index (AI)

Coarse aggregate angularity is determined manually by counting the number of fractured faces on an aggregate particle according to ASTM D 5821-95. Figures 2.16 and 2.17 show the test setups for the Uncompacted Voids in Coarse Aggregate (AASHTO TP56) and the Uncompacted voids in Fine Aggregate (AASHTO T304), respectively. In both tests, aggregate particles at a specified gradation fell down freely into a cylindrical container. Knowing the specified gravity of the aggregate, the voids between aggregate particles can be determined. The more angular the aggregates are, usually the higher is the voids content.

A quantitative "Angularity Index" (AI) was developed based on image analysis from the images captured by the UIAIA (Rao et al., 2002). This AI methodology is based on tracing the change in slope of the particle image outline obtained from each of the top,

side and front images. Accordingly, the AI procedure first determines an angularity index value for each 2-D image. Then, a final AI is established for the particle by taking a weighted average of its angularity determined for all three views.

To determine angularity for each 2-D projection, an image outline, based on aggregate camera view projection, and its coordinates are extracted first. Next, the outline is approximated by an *n*-sided polygon as shown in Figure 2.18. The angle subtended at each vertex of the polygon is then computed. Relative change in slope of the n sides of the polygon is subsequently estimated by computing the change in angle at each vertex with respect to the angle in the preceding vertex. The frequency distribution of the changes in the vertex angles is established in 10-degree class intervals. The number of occurrences in a certain interval and the magnitude are then related to the angularity of the particle profile.

Figure 2.16 Test Setup for Uncompacted Voids in Coarse Aggregate (AASHTO TP56)

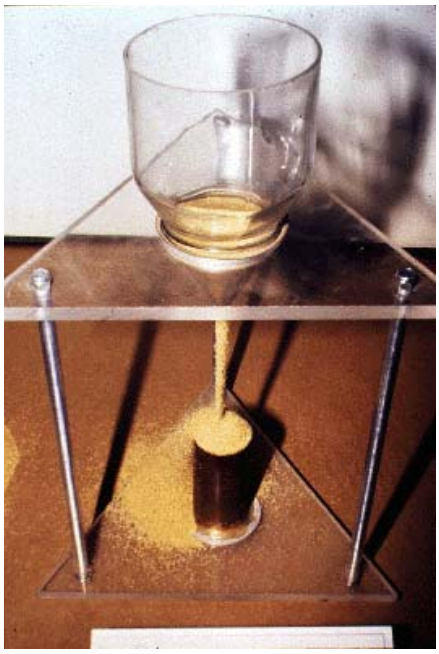

Figure 2.17 Test Setup for Uncompacted Voids in Fine Aggregate (AASHTO T304)

Equation 2.33 is used for calculating angularity of each projected image. In this equation, *e* is the starting angle value for each 10-degree class interval and *P(e)* is the probability of the change in angle and has a value in the range *e* to (*e+10*).

$$Angularity, \quad A = \sum_{e=0}^{170} e * P(e) \tag{2.33}$$

The "Angularity Index" (*AI*) of a particle is then determined by averaging the Angularity values (see Equation 2.34) calculated from all three views when weighted by their areas as given in the following equation:

$$AI = \frac{\sum_{i=1}^{3} Angularity(i) * Area(i)}{\sum_{i=1}^{3} Area(i)} \tag{2.34}$$

where, *i* takes values from 1 to 3 for top, front, and side orthogonal views. The final AI value for the entire sample is simply an average of the Angularity values of all the particles weighted by the particle weight, which measures overall degree changes on the boundary of a particle.

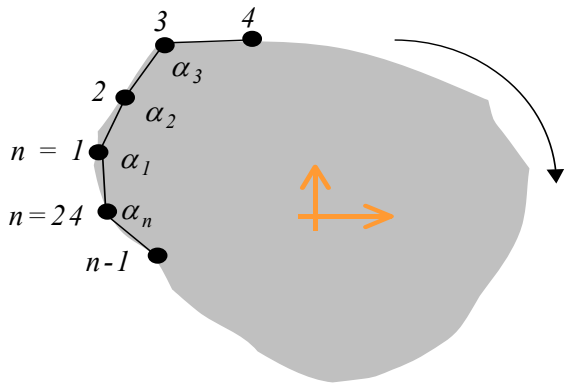

Figure 2.18 Illustration of An n-sided Polygon Approximating the Outline of a Particle (Rao et al. 2002)

Surface Texture

Surface texture usually determines the surface friction property which plays an important role in aggregate interlock providing the strength through inter-particular friction. In this study, surface texture is simplified as the surface friction angle described previously.

Table 2.2 lists typical ranges of morphological index values including Angularity Index and Surface Texture index, for common aggregates according to Tutumluer et al. (2005).

Table 2.2 Typical Ranges of Angularity and Surface Texture Indices (Tutumluer et al., 2005)

Aggregate Type	Angularity Index (AI)		Surface Texture (ST) Index	
	Range	Mean	Range	Mean
Uncrushed Gravel	250-350	300	0.5-1.20	0.900
Crushed Gravel	300-450	400	1.00-1.50	1.200
Crushed Limestone	400-550	500	1.20-1.80	1.600
Crushed Granite	500-650	550	1.80-2.90	2.200

2.8 Summary

Previous research studies on factors affecting ballast strength and stability were reviewed in this chapter. Research studies about ballast aggregate size distribution and shape properties are summarized. Effects of ballast aggregate size distribution and morphological properties on ballast settlement and lateral stability need to be further studied and are determined to be the research task of this thesis. Among the numerical methods readily available to apply to railroad track research, the Discrete Element Modeling technique is the most promising. A DEM program BLOKS3D chosen for this study was described in detail about fast contact detection algorithm and the use of arbitrary block shaped elements. By introducing digital image analysis techniques, DEM can be implemented with aggregate particle shapes characterized through imaging based shape indices also introduced as part of the University of Illinois Aggregate Image Analyzer (UIAIA).

3. DIGITAL IMAGE AIDED PARTICLE SHAPE GENERATION IN DISCRETE ELEMENT METHOD

The Discrete Element Method (DEM) is more realistic when compared to continuum analysis of a railroad ballast layer. The BLOKS3D DEM program used in this research considers polyhedrons to represent arbitrary shaped angular aggregates as discrete elements with the capability of user defined particle morphological properties from imaging based shape indices. This chapter introduces a digital image aided particle shape generation method for DEM to better capture the shape effects of aggregate particles on railroad ballast behavior. The 3D image analysis approach developed by Tutumluer et al. (2001) is readily available to be used to construct discrete elements with shapes close to the morphological properties of actual ballast aggregate shapes.

A large sized shear box is used in direct shear tests to validate this image aided particle shape generation DEM method. The purpose of validation is to match the laboratory test results with the DEM simulation results by using one single set of model parameters. To that end, sensitivity of DEM model parameters are investigated by conducting DEM shear box simulations using different combinations of model parameters realistically chosen based on previous research studies. The validation process is finally accomplished by statistically demonstrating that the DEM shear box simulation results based on one set of parameters can predict reasonably well the laboratory shear box test results under varies normal stress levels.

3.1 Digital Image Aided DEM Particle Shape Generation Method

The UIAIA captures images to establish aggregate morphological indices from three orthogonal 2D digital images of an aggregate particle (see Figure 3.1). It is possible to create a 3D particle by using these three 2D orthogonal views with desired shape indices. Further, such a 3-D particle can be generated in the DEM program BLOKS3D as an element with desired morphological characteristics. The following section describes the detailed procedure on how to generate an element with the aid of digital image technology.

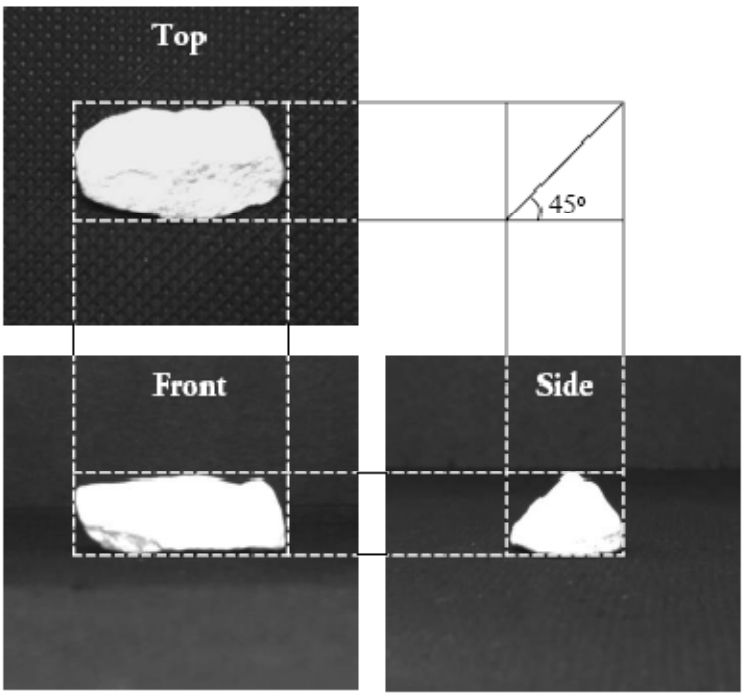

Figure 3.1 Top, Front, and Side Views of an Aggregate Particle Processed through UIAIA

3D DEM Element Generation Based on Particle Shape Properties

1. Generate three 2D images from orthogonal views in terms of the geometrical compatibility principles shown in Figure 3.2.

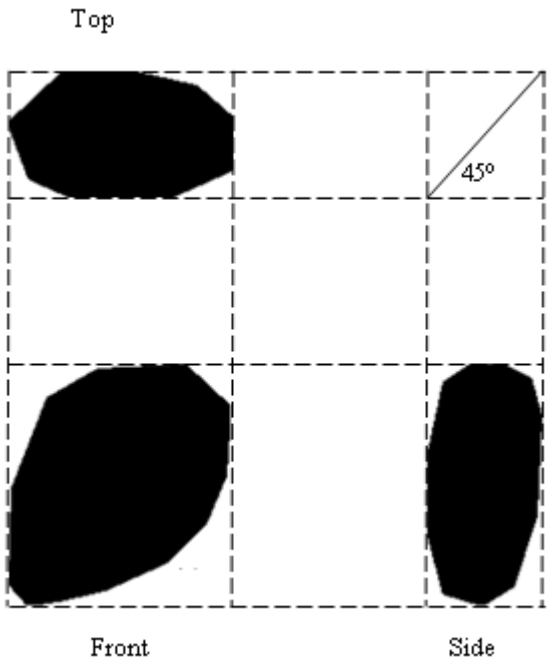

Figure 3.2 Generated 2D Images of Desired Particle Shapes from Three Orthogonal Views

2. Compute next the areas (represented by pixels), AIs, and F&E Ratios for these three images. In this case, areas of 10920, 19600, and 9380 square pixels were obtained for top, front, and side views, respectively. Also, AIs of 465, 357, and 410 were obtained for top, front, and side views, respectively. Based on the Equation 2.34, the AI index (i.e. the weighted average of the AIs over areas of three views) of an aggregate particle with these three 2D views is 399. For the aggregate particle a F&E ratio of 2.1:1 is also obtained in this case. If the particle

indices are adequate for the discrete element to be generated, continue to the next step; otherwise, adjust these three views and repeat step 2 until the desired shape indices are accomplished for the discrete element generated.

3. As shown in Figure 3.3, assemble these three orthogonal views to establish the aggregate particle discrete element representation.
4. As shown in Figure 3.4, extrude these 2D images in the three orthogonal directions to form 3D columns intersecting each other;
5. Figure 3.5 shows only the 3D generation of these intersecting columns which is defined in this study as the discrete element with desired shape indices in to be used in the BLOKS3D DEM program.

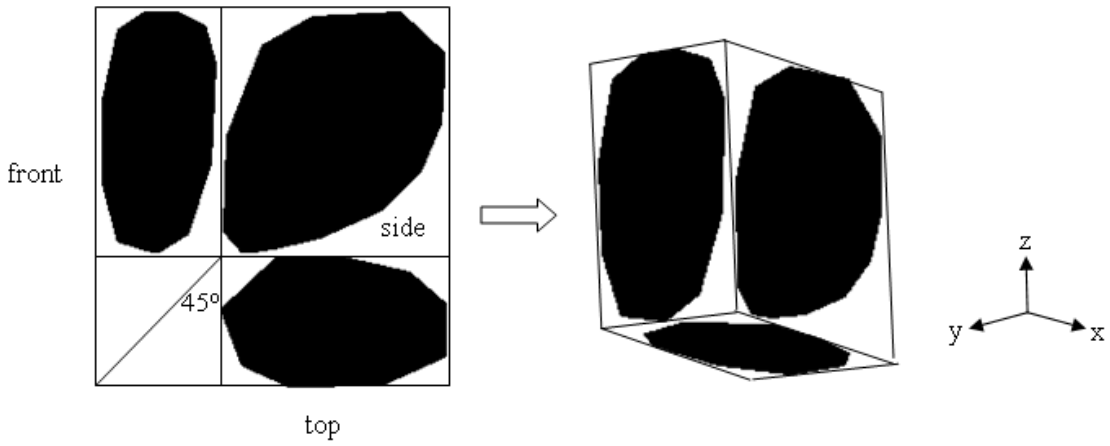

Figure 3.3 Three 2D Images Generated in Terms of the Desired Particle Shape Indices

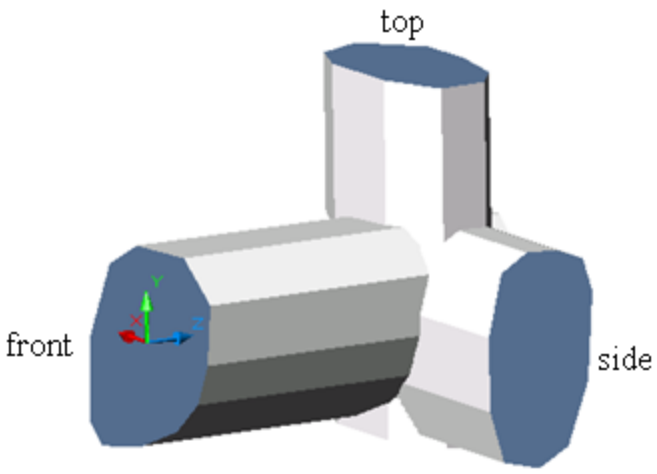

Figure 3.4 Three Orthogonal Views Intersecting Each Other

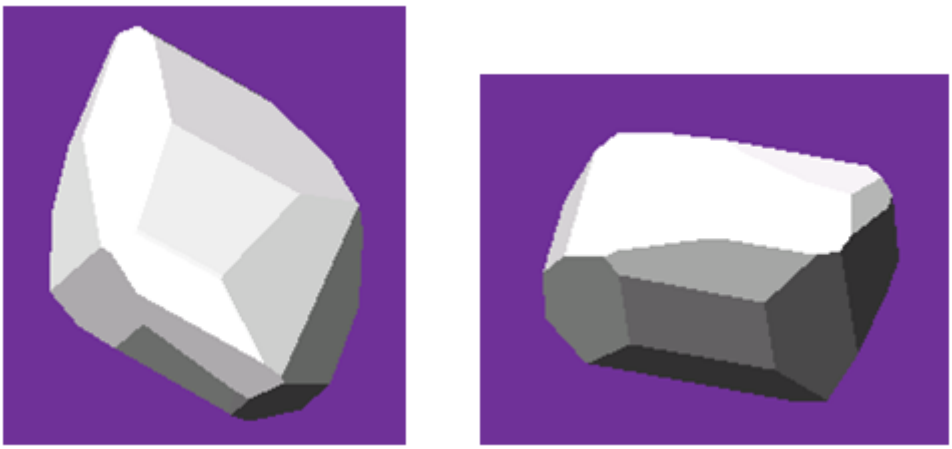

Figure 3.5 Two Views of the Generated BLOKS3D Element Based on the Desired Particle Shape Indices

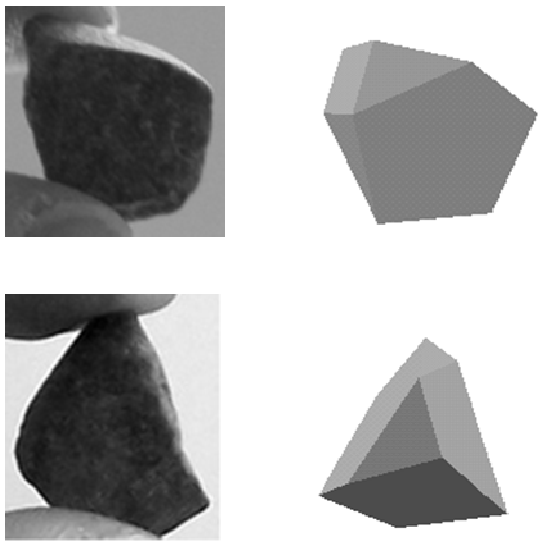

Figure 3.6 The Aggregate Particle Shown by Photos and the Generated BLOKS3D Element

Figure 3.6 compares two images of an aggregate particle with the two views of the discrete element generated for BLOKS3D DEM program. It can be seen that the element has a fairly shape when compared to the real aggregate. Figure 3.7 shows a total of 11 such representative aggregate particle shapes generated with the method described ranging from cubical and angular to rounded and flat and elongated. The detailed shape indices of these particle shapes are listed in Table 3.1. These shapes have been built for DEM program BLOKS3D to study effects of aggregate morphological properties on the ballast lateral stability, strength and settlement behavior in this thesis.

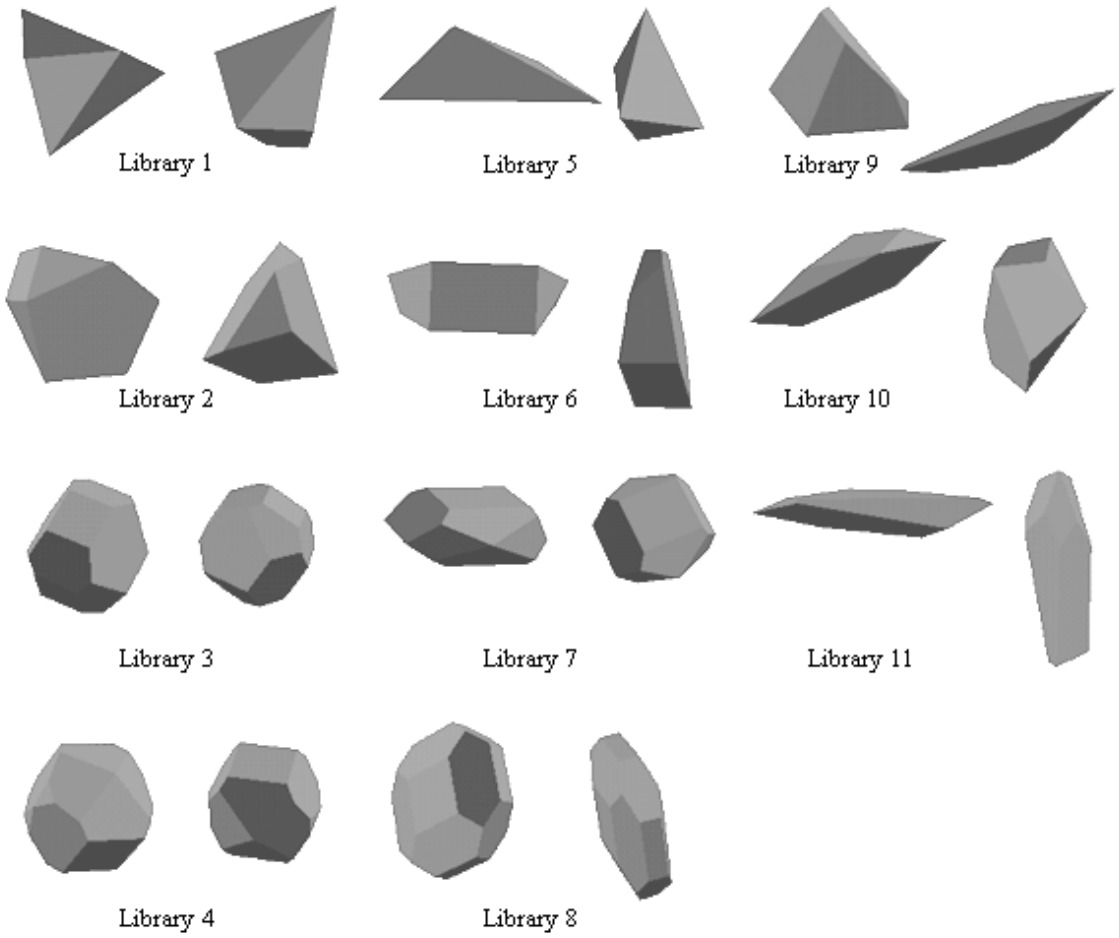

Figure 3.7 Two Views Each of Eleven Representative Aggregate Shapes

Table 3.1 Angularity Indices and F&E Ratios of the Eleven Representative Aggregate Particles

Library	**1**	**2**	**3**	**4**	**5**	**6**	**7**	**8**	**9**	**10**	**11**
AI	630	570	448	390	620	570	454	347	573	490	360
F&E	1:1	1:1	1:1	1:1	3:1	3:1	3:1	3:1	5:1	5:1	5:1

3.2 Laboratory Validation

After the generation of "representative aggregate shapes" for use in DEM with the aid of digital image technology, laboratory validation of the ballast DEM model is undertaken to simulate the shear box direct shear strength test results. The principle of validation is to match the experimental results with DEM simulation results by adjusting DEM parameters until simulation results from one set of model parameters match all experimental results.

3.2.1 Laboratory Tests

Shear box direct shear strength tests on ballast aggregates were performed in the Geotechnical Laboratory of Newmark Civil Engineering Laboratory (NCEL). Since aggregates studied are quite large (0.076 m top sized railroad ballast aggregate), a large laboratory testing device had to be used to minimize the size effects. The large direct shear device used was 0.08 m (3 in.) deep, with square dimensions of 0.3 m (12 in.) for the upper ring and 0.16 m (6 in.) deep with dimensions of 0.3 m (12 in.) by 0.36 m (14 in.) for the lower box (see Figure 3.8). An air bladder supplied the normal pressure up to 550 kPa (80 psi).

Clean granite ballast aggregates were used for the validation tests. The granite aggregates were sieved and analyzed by the imaging equipment UIAIA. Their size distribution (see Figure 3.9) conformed with the AREMA No.24 gradation. The granite aggregate had an average AI of 550, and an average F&E ratio of 1.3:1. Large shear box samples were then prepared according to the following procedure:

1. Place aggregates in the lower box by lifts (usually two 76 mm lifts).

2. For each lift, use a vibratory compactor on top of a flat Plexiglas compaction platform and compact until no noticeable movement of particles is observed (see Figure 3.8).
3. Record the weight of aggregates used.

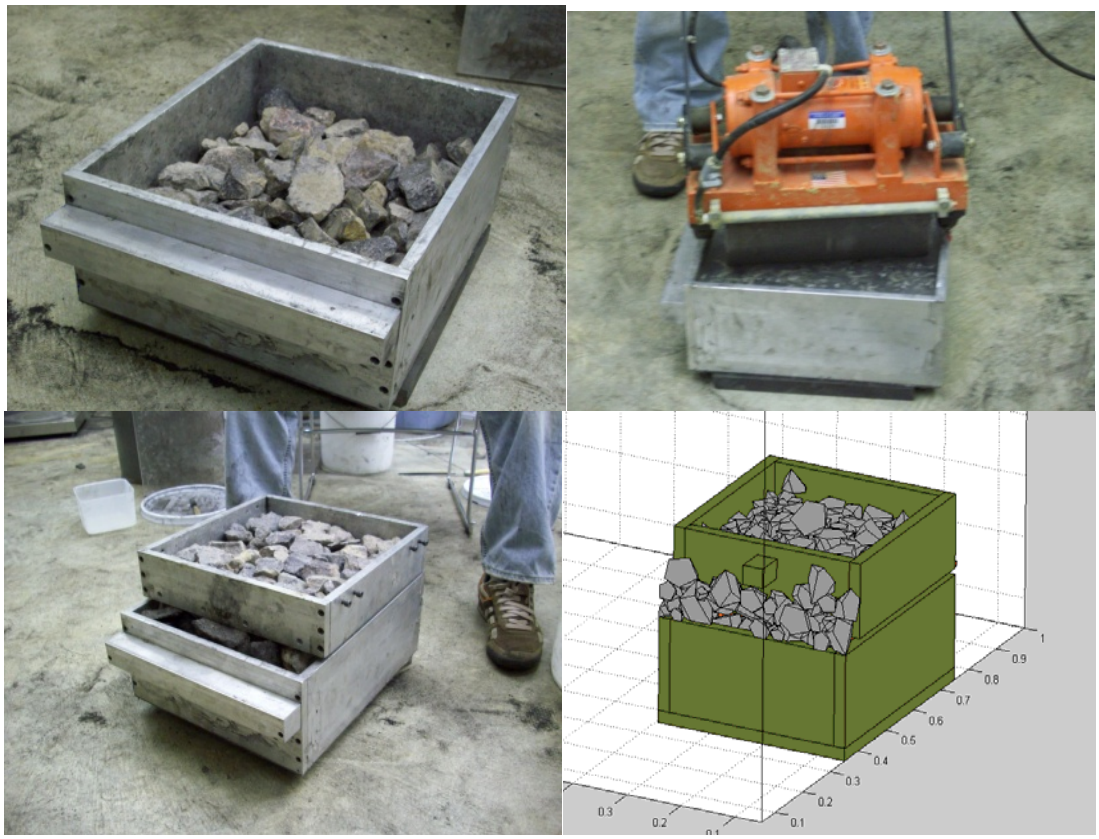

Figure 3.8 Preparing Large Shear Box Sample and Its DEM Model

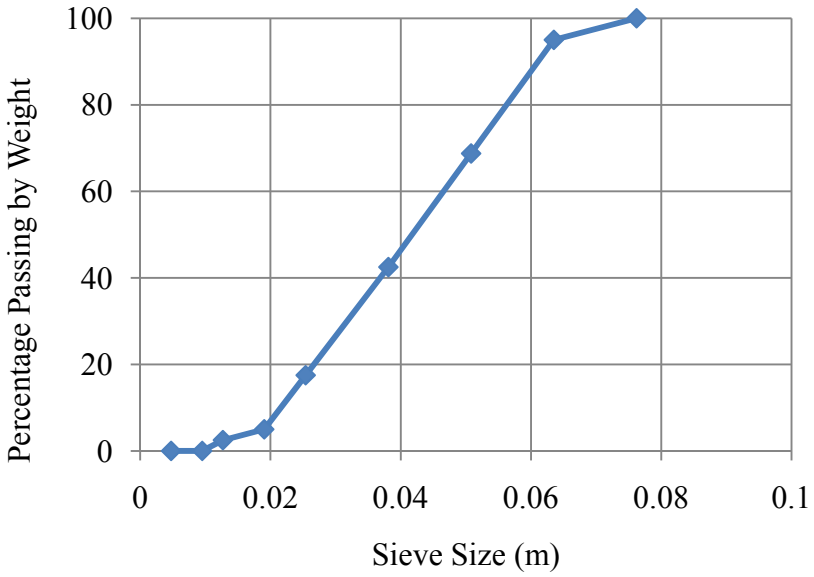

Figure 3.9 Size Distribution of the Granite Aggregate Used for Validation

A typical field air voids content of around 43% was achieved for all shear box samples. Three target normal pressures (103, 172, and 241 kPa) were applied followed by a shearing rate of 0.2 mm/sec. Figure 3.10 shows the typical trend of shear stress changing with the shear displacement for one individual shear box specimen tested under the targeted normal stress of 103 kPa (158 kPa actual applied stress).

Figure 3.11 shows the shear strength envelope constructed by using results from 11 individual direct shear box tests. Each data point on this strength envelope represents the peak shear stresses plotted against the actual normal stresses from an individual shear box test. A friction angle of 44 degrees was obtained for the granite aggregate with a high coefficient of determination (0.93) implying fairly high repeatability for the large direct shear apparatus.

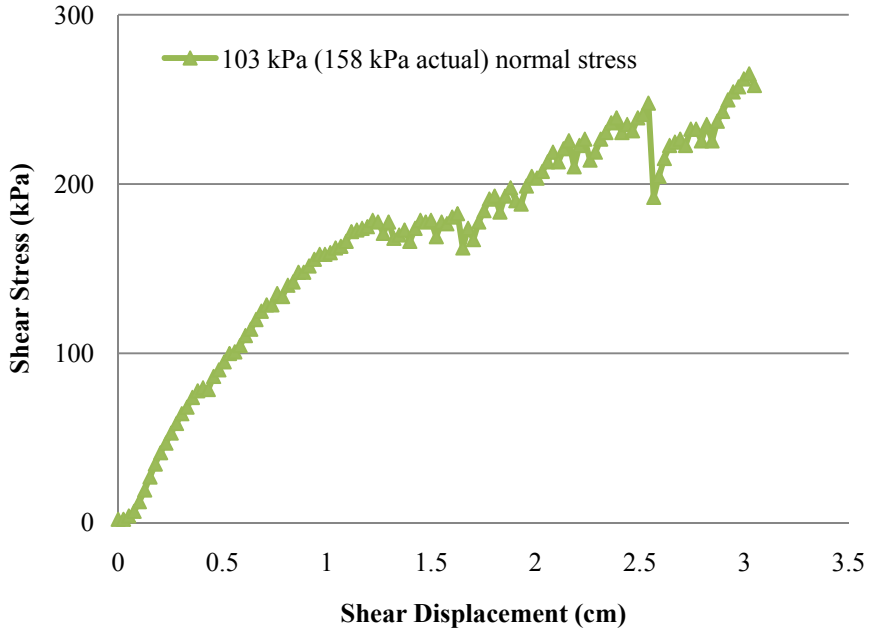

Figure 3.10 Shear Reaction Stress Plotted against Shear Displacement at 103 kPa Target (158 kPa Applied) Normal Stress

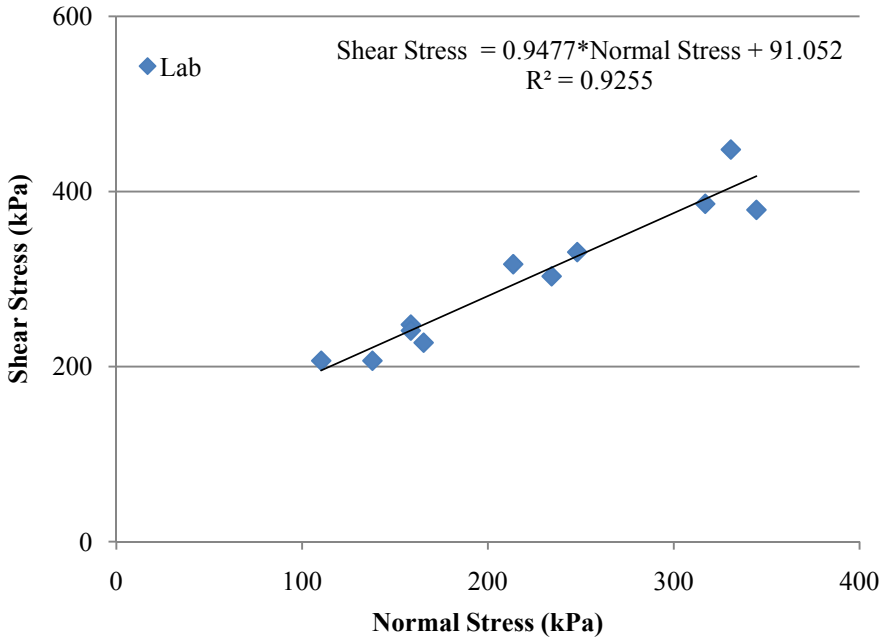

Figure 3.11 Results from Laboratory Large Direct Shear Apparatus for Clean Granite Ballast

After completing laboratory direct shear tests on the granite aggregate, ballast DEM model shear box simulations were performed. Elements from BLOKS3D library 2 corresponding to AI of 550 and F&E ratio of 1.3:1 were generated with AREMA No.24 gradation (see Figure 3.8 for the DEM simulation). As mentioned previously, the purpose of validation is to match the laboratory test results with the DEM simulation results by using one single set of DEM model parameters. To select such a set of model parameters, a sensitivity study was conducted on major model parameters to establish a better basic understanding of the influence of the model parameters on the DEM simulation results.

3.2.2 Sensitivities of DEM Model Parameters

Normal and shear contact stiffnesses and surface friction angle have been reviewed in the previous chapter as the major DEM model parameters. Their effects on the shear box DEM simulation results need to be studied in detail. This section investigates the effects of contact stiffnesses and the surface friction angle on the shear box DEM simulation results.

A normal stress of 158 kPa, similar to the experimental conditions indicated in Figure 3.10, is applied in all DEM shear box simulations undertaken as part of the sensitivity study. Table 3.2 lists the approximate ranges of the contact stiffness values for granite type ballast aggregate based on the theoretical derivations in Chapter 2. In addition, surface friction angles of 22, 27, 31, 35 degrees are also considered based on the work done by Marsal (1963) previously described in Chapter 2.

Table 3.2 Contact Stiffness Values for Granite Type Railroad Ballast Aggregate

Aggregate Elastic Modulus (GPa)	Poison's Ratio	Normal Contact Force "P" (N)	Aggregate Equvalent Radius (R) (m)	λ (degrees)	Hertzian Normal Contact Stiffness (N/m)	Cone on Plane Normal Contact Stiffness (N/m)
53	0.2	350	0.02	15	30,114,276	10,656,028

To investigate first the effect of contact stiffness on DEM simulation results, the four cases with varying normal and shear contact stiffnesses as listed in Table 3.3 are studied. For Kn and Ks, 10 and 20 MN/m values were considered according to Table 3.2. Note that these values for contact stiffnesses adequately cover rounded and angular aggregates with possible sharp corners.

Aggregate samples generated in DEM simulations with exactly the same particle shapes and size distributions may still yield different results. This is mainly due to the differences in initial sample conditions including locations and orientations of each individual element (see Figure 3.12). Figure 3.12 shows two example initial conditions with the same air voids content. To further study these differences and minimize the error caused by different initial sample conditions, three repetitions of each simulation case have also been studied in the sensitivity analyses of major model parameters.

Table 3.3 DEM Model Parameter Combinations for Contact Stiffness Effect

Case	Normal Contact Stiffness (MN/m)	Shear Contact Stiffness (MN/m)	Surface Friction Angle (degree)
1	20	20	31
2	20	10	31
3	10	20	31
4	10	10	31

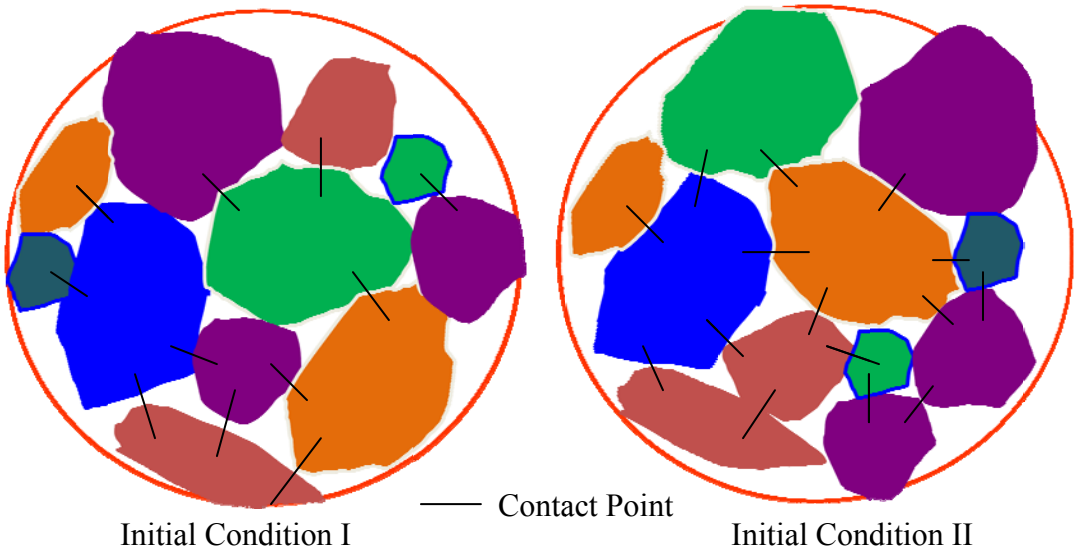

Figure 3.12 Differences in Initial Sample Conditions with Same Elements

Figure 3.13 through Figure 3.16 show the predicted shear stresses plotted against the shear displacements for three different initial conditions under the applied normal stress of 158 kPa using the surface friction angle $\theta = 31$ degrees. Figures 3.13 and 3.14 assign Kn = 20 MN/m and Figures 3.15 and 3.16 assign Kn = 10 MN/m. Similarly, Figures 3.13 and 3.15 assign Ks = 20 MN/m and Figures 3.14 and 3.16 assign Ks = 10 MN/m.

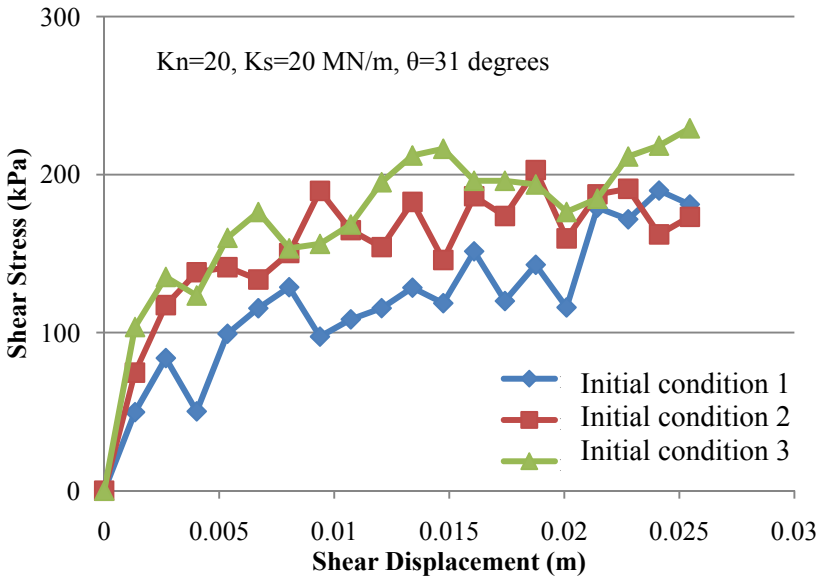

Figure 3.13 Shear Stresses Plotted against Shear Displacements for Kn=20, Ks=20 MN/m, and θ=31 degrees

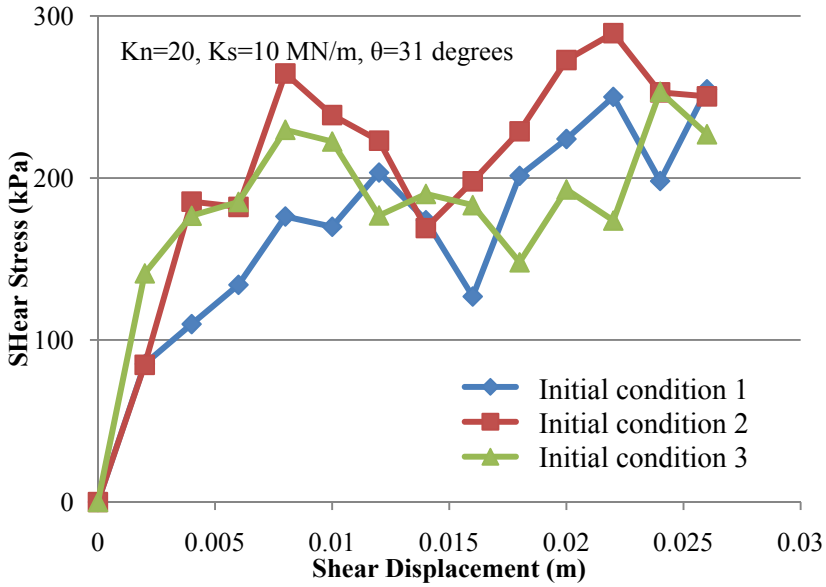

Figure 3.14 Shear Stresses Plotted against Shear Displacements for Kn=20, Ks=10 MN/m, and θ=31 degrees

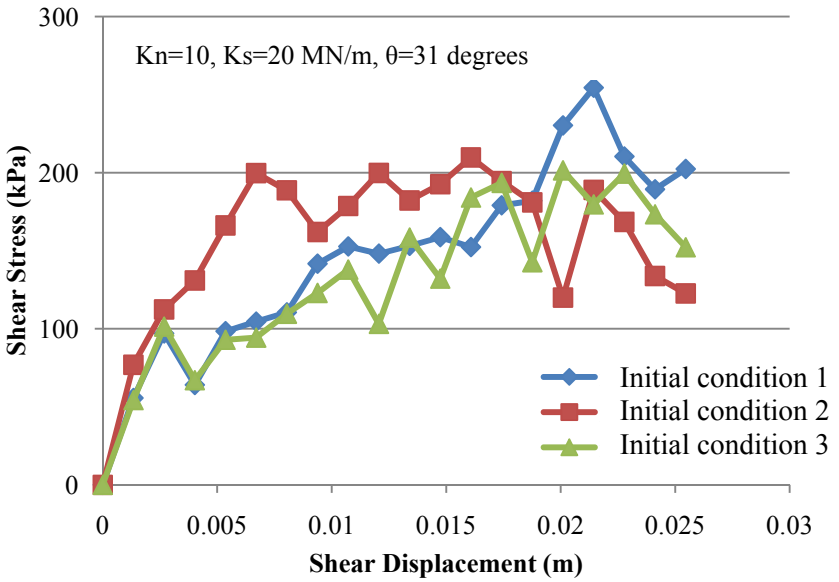

Figure 3.15 Shear Stresses Plotted against Shear Displacements for Kn=10, Ks=20 MN/m, and θ=31 degrees

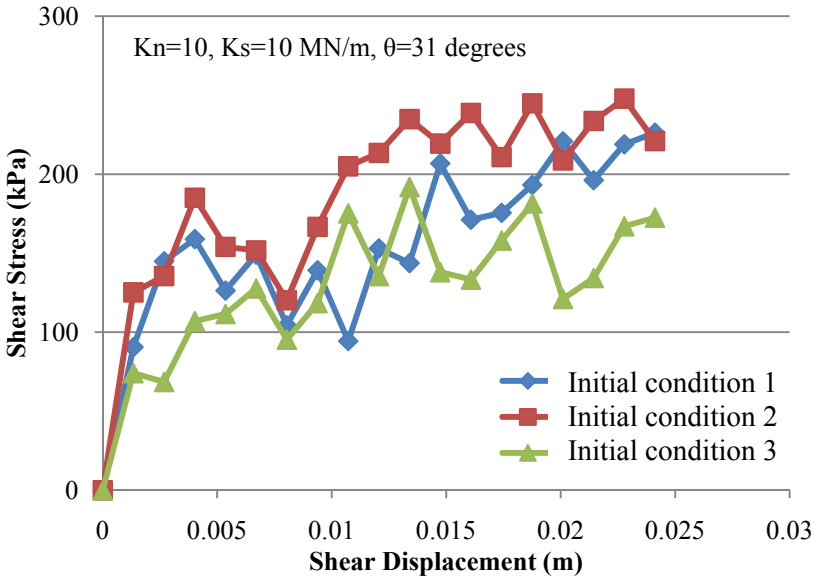

Figure 3.16 Shear Stresses Plotted against Shear Displacements for Kn=10, Ks=10 MN/m, and θ=31 degrees

To better visualize the sensitivity of DEM model parameters to the simulation results, mean values and 95% confidence intervals of all the results from DEM simulations are plotted in Figure 3.17 to Figure 3.20. The 95% confidence interval lines (dash lines) connect each confidence interval of three shear stress values for every displacement value (see Figure 3.17) calculated in the EXCEL spreadsheet by using the function "CONFIDENCE (alpha, standard deviation, sample size). Alpha in this case is 0.05 and the sample size is 3. The standard deviations are obtained by using EXCEL "descriptive statistics" function and listed in Table 3.4.

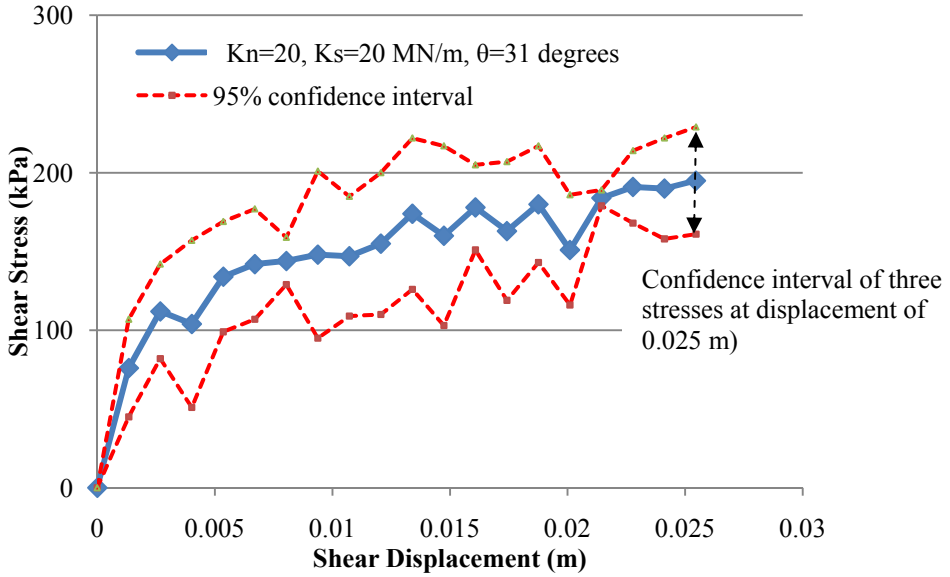

Figure 3.17 Mean and 95% Confidence Interval of Shear Stress Plotted against Shear Displacement for Kn=20, Ks=20 MN/m, and θ=31 degrees

Table 3.4 Mean Stresses and Standard Deviations for Three Replicates

Displacement	0	0.00134	0.00268	0.00402	0.00536	0.0067	0.00804	0.00938	0.01072	0.01206
Mean	0	76	112	104	134	142	144	148	147	155
Standard Deviation	0	26.9	26.1	47.1	31.1	31.2	13.4	46.7	33.6	39.8
Displacement	0.0134	0.01474	0.01608	0.01742	0.01876	0.0201	0.02144	0.02278	0.02412	0.02546
Mean	174	160	178	163	180	151	184	191	190	195
Standard Deviation	42.4	50.4	23.5	39.1	32.3	31.2	4.32	19.9	28.1	30.4

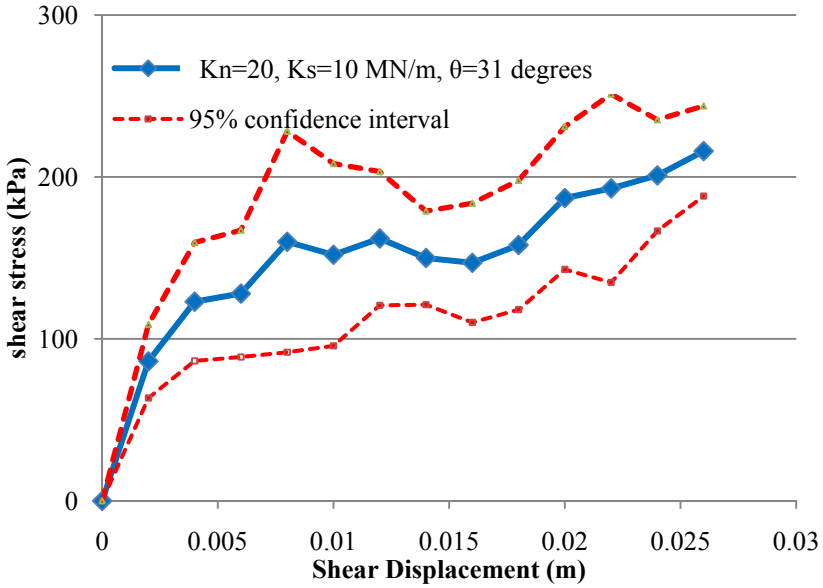

Figure 3.18 Mean and 95% Confidence Interval of Shear Stress Plotted against Shear Displacement for Kn=20, Ks=10 MN/m, and θ=31 degrees

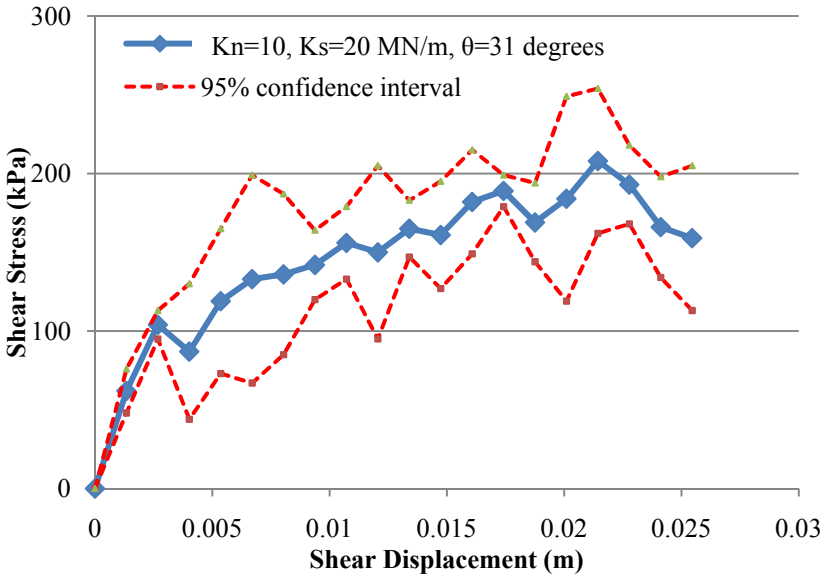

Figure 3.19 Mean and 95% Confidence Interval of Shear Stress Plotted against Shear Displacement for Kn=10, Ks=20 MN/m, and θ=31 degrees

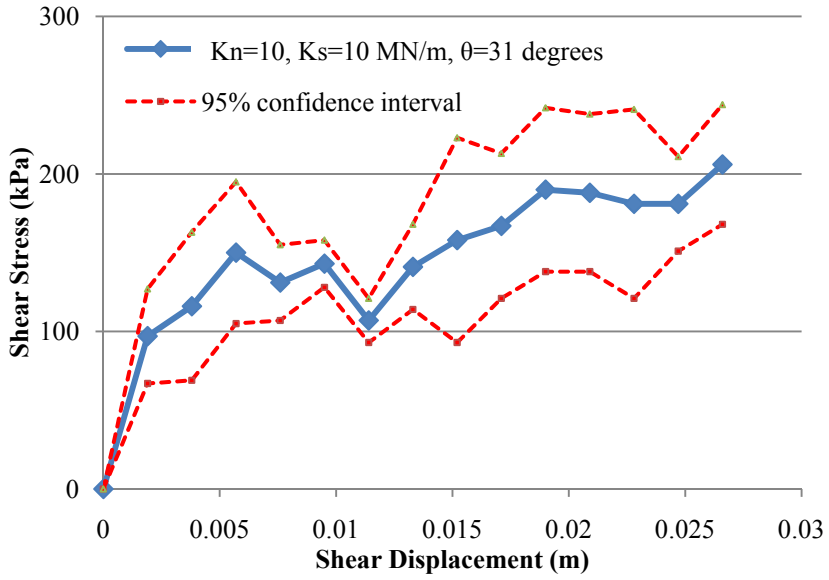

Figure 3.20 Mean and 95% Confidence Interval of Shear Stress Plotted against Shear Displacement for Kn=10, Ks=10 MN/m, and θ=31 degrees

Finally, Figure 3.21 graphs the mean shear stress values plotted against the shear displacement for all contact stiffness combinations. Only slight differences can be observed in the results obtained from all different stiffness combinations which may imply that the contact stiffnesses have in general a minor effect on DEM simulation results. That is also consistent with the findings of the previous study by Nezami (2007).

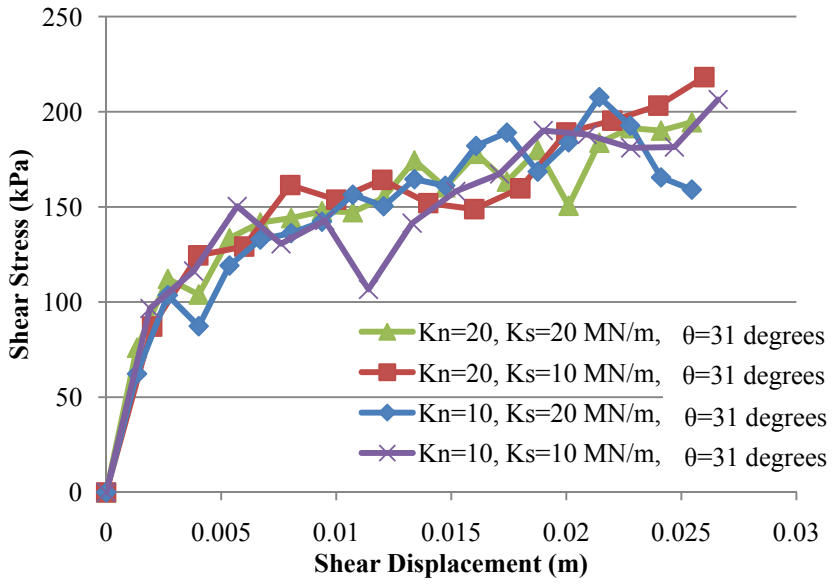

Figure 3.21 Mean Shear Stress Values Plotted against Shear Displacements for All Stiffness Combinations

To investigate the effect of surface friction angle θ on DEM simulation results, four different θ values were also studied as listed in Table 3.5. Contact stiffnesses of Kn = 20 MN/m and Ks = 10 MN/m were used since the simulation results from this contact stiffness combination indicated a close trend with the experimental results obtained in the laboratory (see Figure 3.10). Figure 3.22 highlights this close agreement.

Table 3.5 DEM Model Parameter Combinations for Surface Friction Angle Effect

Case	Normal Contact Stiffness (MN/m)	Shear Contact Stiffness (MN/m)	Surface Friction Angle (degree)
1	20	10	35
2	20	10	31
3	20	10	27
4	20	10	22

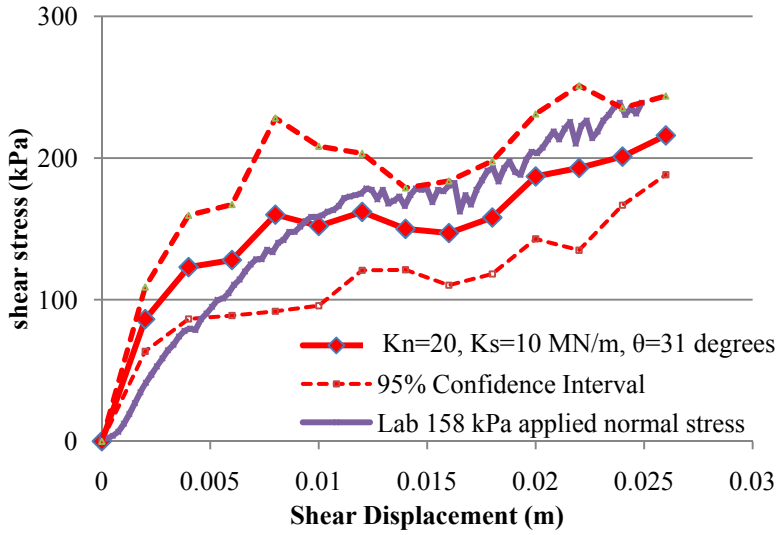

Figure 3.22 Close Match Observed between Laboratory Results and DEM Simulations Using Kn=20, Ks=10 MN/m and θ = 31 degrees

Figure 3.23 through Figure 3.25 show the shear stresses plotted against the shear displacements for different initial conditions under the applied normal stress of 158 kPa using Kn = 20 MN/m, Ks = 10 MN/m, and θ = 35, 27 and 22 degrees, respectively. Figure 3.26 through Figure 3.28 show the mean values and 95% confidence intervals of the results for θ = 35, 27 and 22 degrees, respectively.

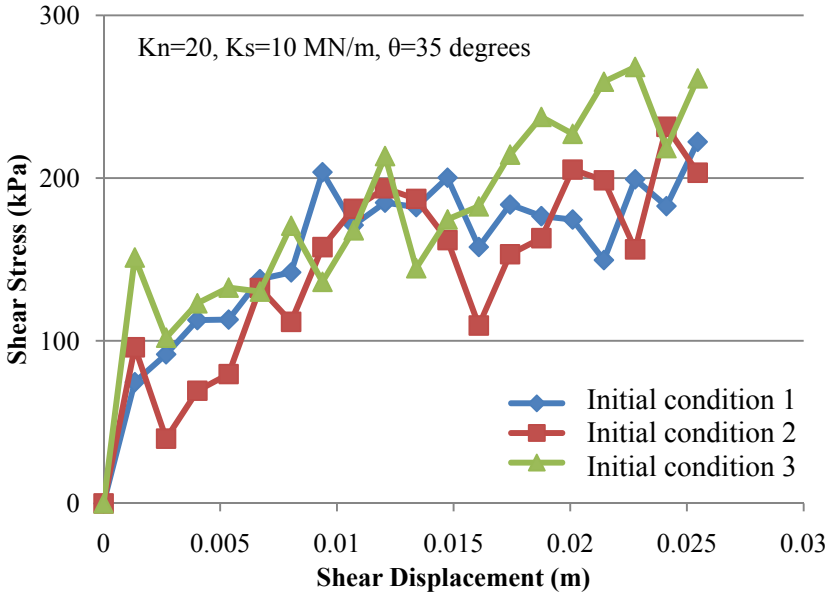

Figure 3.23 Shear Stresses Plotted against Shear Displacements for Kn=20, Ks=10 MN/m, and θ=35 degrees

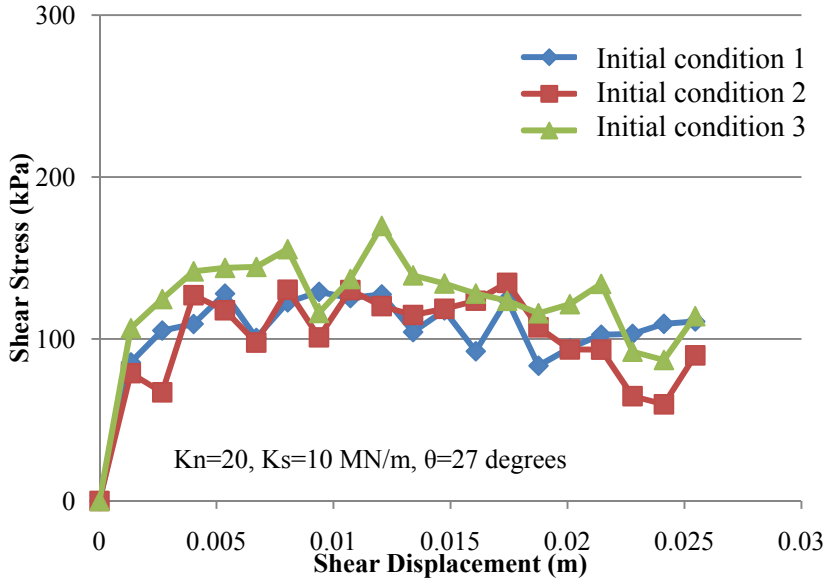

Figure 3.24 Shear Stresses Plotted against Shear Displacements for Kn=20, Ks=10 MN/m, and θ=27 degrees

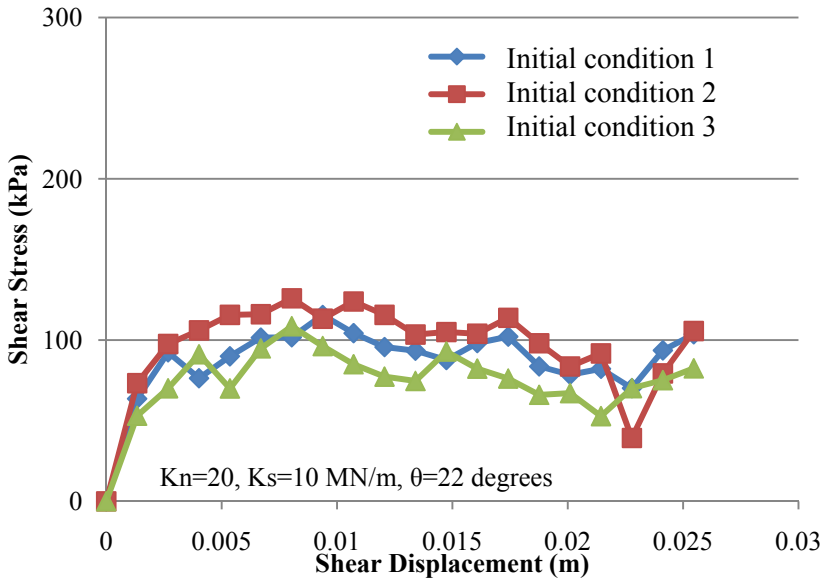

Figure 3.25 Shear Stresses Plotted against Shear Displacements for Kn=20, Ks=10 MN/m, and θ=22 degrees

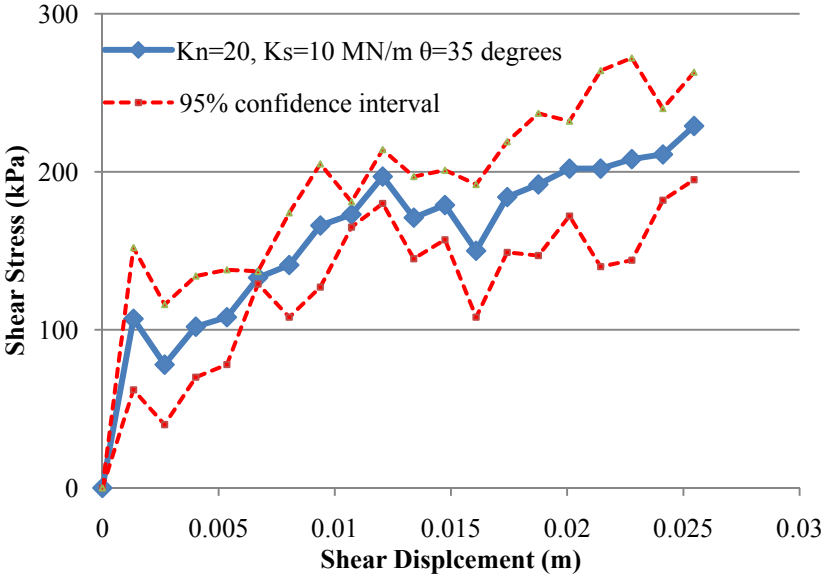

Figure 3.26 Mean and 95% Confidence Interval of Shear Stress Plotted against Shear Displacements for Kn=20, Ks=10 MN/m, and θ=35 degrees

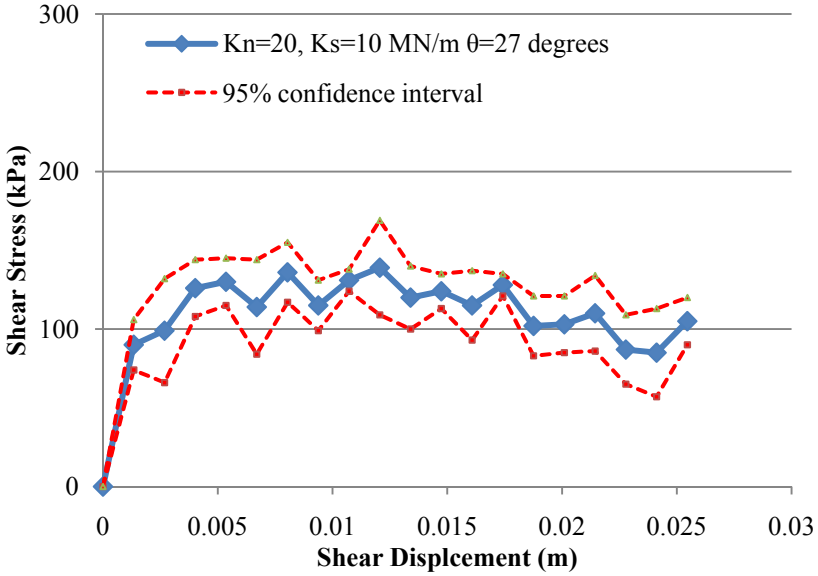

Figure 3.27 Mean and 95% Confidence Interval of Shear Stress Plotted against Shear Displacements for Kn=20, Ks=10 MN/m, and θ=27 degrees

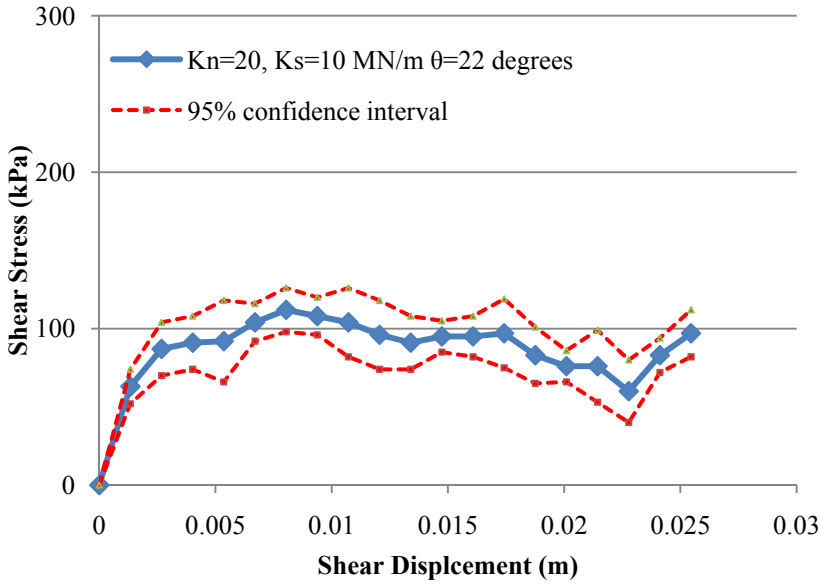

Figure 3.28 Mean and 95% Confidence Interval of Shear Stress Plotted against Shear Displacements for Kn=20, Ks=10 MN/m, and θ=22 degrees

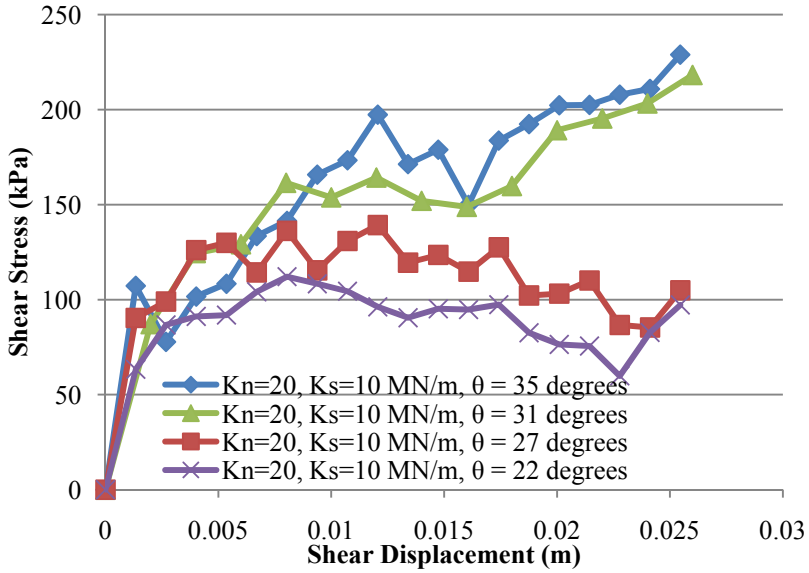

Figure 3.29 Mean Shear Stress Values Plotted against Shear Displacements for All Surface Friction Angle Combinations

Figure 3.29 graphs the mean shear stress values plotted against the shear displacements for all surface friction angle combinations. Significant differences are observed for results from all different surface friction angle combinations when compared to those from different contact stiffness combinations. Therefore, based on the sensitivity results, the following approach was adopted to better calibrate the DEM model.

1. A reasonably large contact stiffness, obtained from testing contact surface properties of aggregate parent material, can prevent excessive penetration into particles and thus avoid numerical instability. A very large contact stiffness value, however, may result in a very long computation time, since larger contact stiffness values require shorter time steps to maintain the numerical stability and

accuracy. So, normal contact stiffness value should be carefully chosen to satisfy not only the numerical stability and accuracy but also the computation cost.

2. Calibration of the DEM model parameters can best be accomplished through adjusting the surface friction angle so that the DEM simulation results can match the laboratory test results.

3.2.3 Repeatability of Laboratory and the DEM Results

Based on the results of the sensitivity study and the calibration approach adopted, the final set of DEM model parameters established here are: Kn = 20MN/m, Ks = 10MN/m, and $\theta = 31^{o}$. To demonstrate that this set of parameters can predict laboratory results reasonably accurately, DEM shear box simulations were conducted under three normal stresses using this single set of model parameters and then compared with the laboratory shear box results. Six repetitions were performed for each DEM shear box simulation to take into account any possible error caused by different sample initial conditions.

Figure 3.30 shows the shear stresses varying with the shear displacements for DEM repetitions with six different initial conditions as well as the laboratory test under the applied normal stress of 158 kPa (103 kPa target). Figure 3.31 shows the mean values and 95% confidence intervals for the six repetitions with the experimental results.

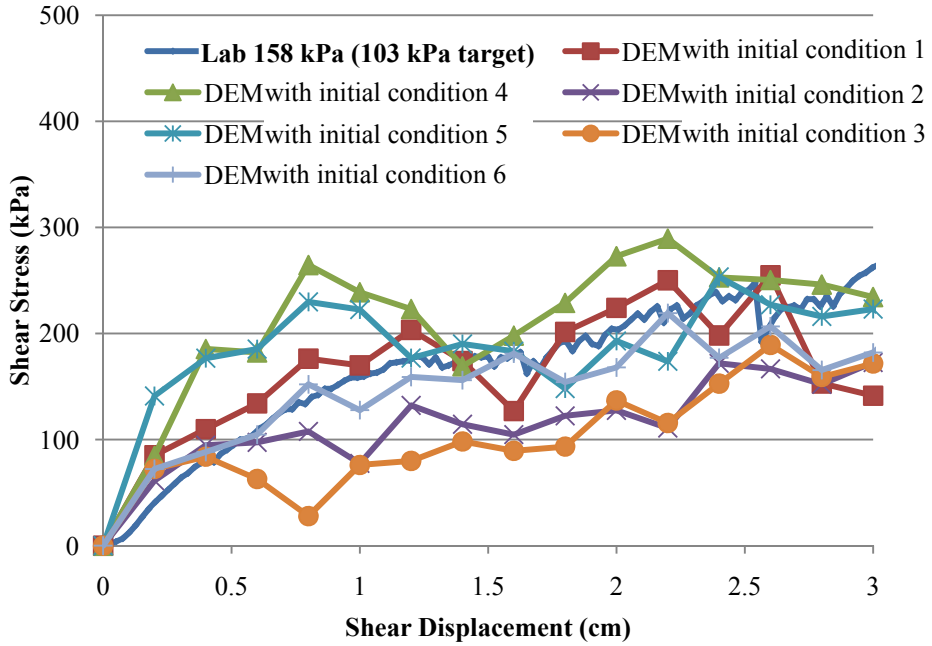

Figure 3.30 Shear Stress Plotted against Shear Displacement for both DEM and Experimental Results under Normal Stress of 158 kPa (103 kPa Target)

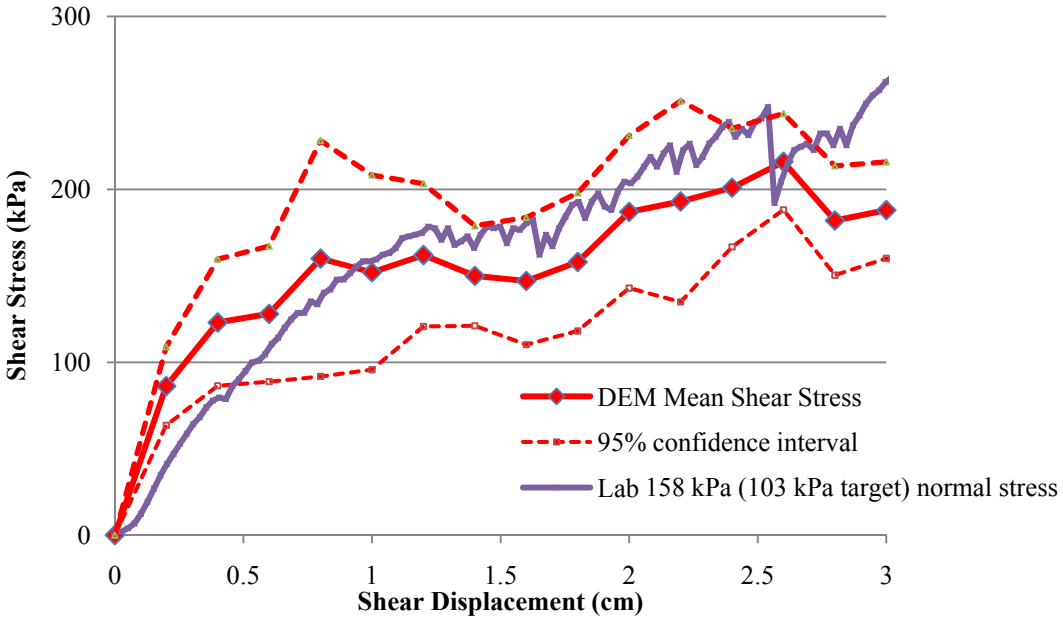

Figure 3.31 Mean Shear Stresses and 95% Confidence Intervals of DEM Simulations Plotted with the Experimental Result under the Normal Stress of 158 kPa

Similarly, Figure 3.32 graphs the shear stress changing with the shear displacement for DEM repetitions with six initial conditions as well as the laboratory test under the normal stress of 248 kPa (172 kPa target). Figure 3.33 graphs the mean values and 95% confidence intervals for six DEM repetitions and the laboratory test result. The same type of graphs are given in Figures 3.34 and 3.35 for the normal stress of 317 kPa (241 target).

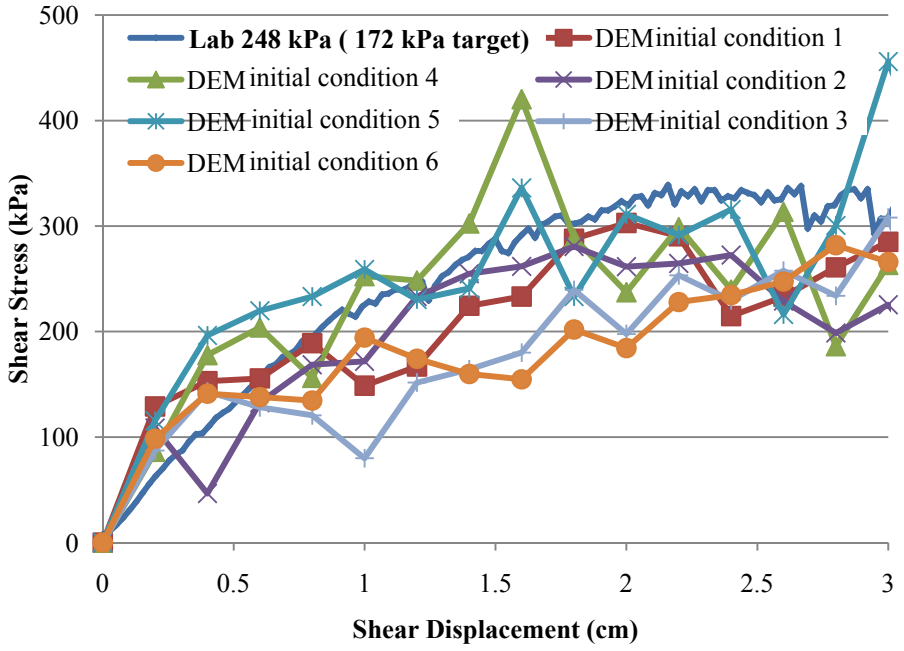

Figure 3.32 Shear Stress Plotted against Shear Displacement for both the DEM Simulations and the Laboratory Result under Normal Stress of 248 kPa (172 kPa Target)

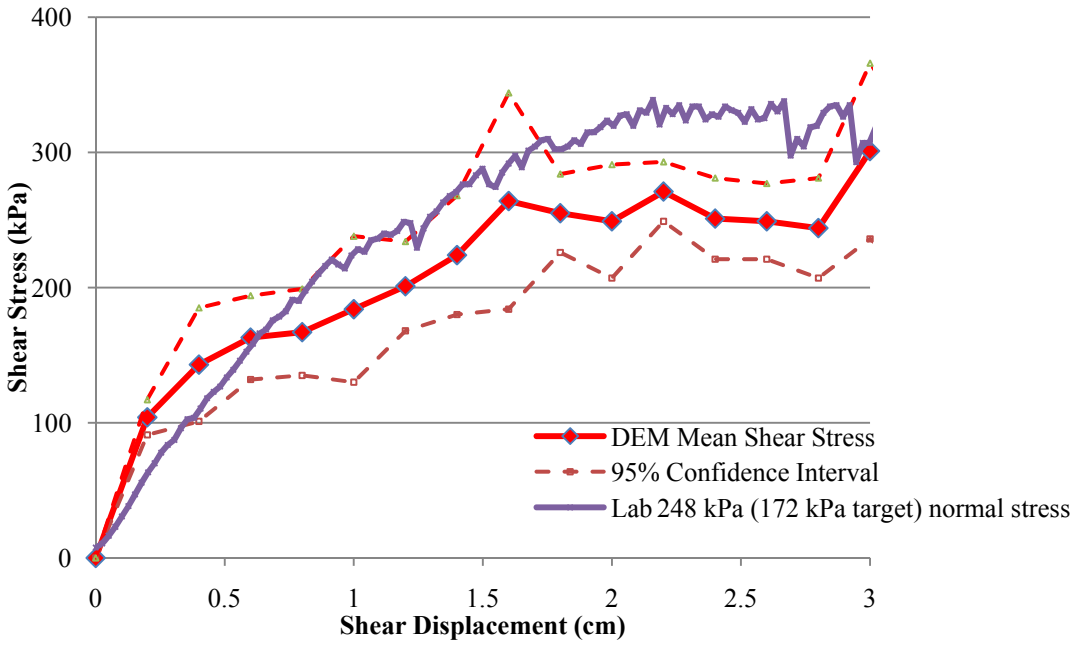

Figure 3.33 Mean Shear Stress and 95% Confidence Interval of DEM Plotted with the Laboratory Result under the Normal Stress of 248 kPa (172 kPa Target)

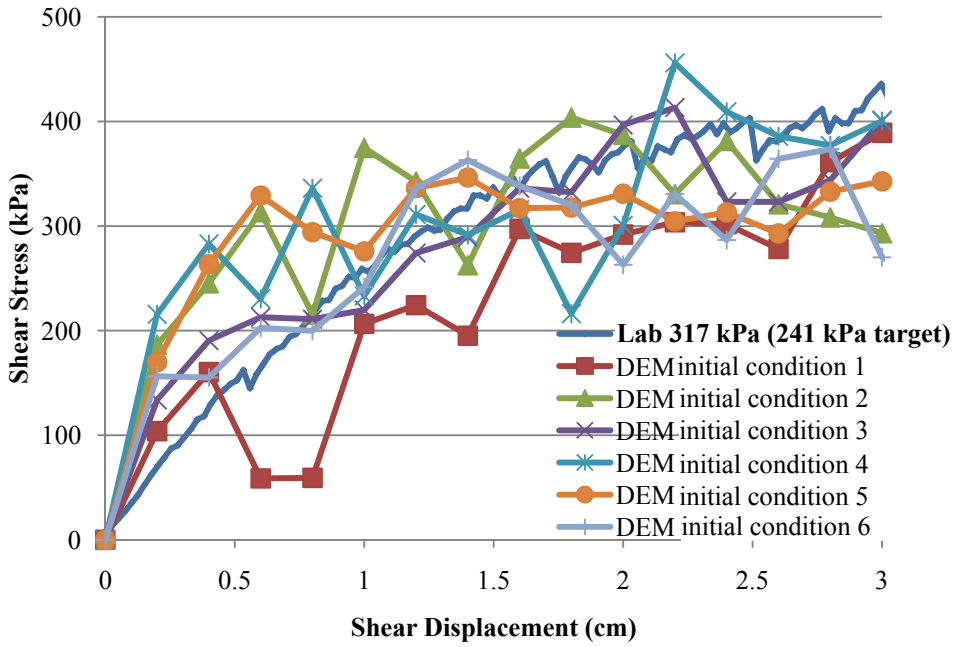

Figure 3.34 Shear Stress Plotted against Shear Displacement for both DEM Simulations and the Laboratory Result under Normal Stress of 317 kPa (241 kPa Target)

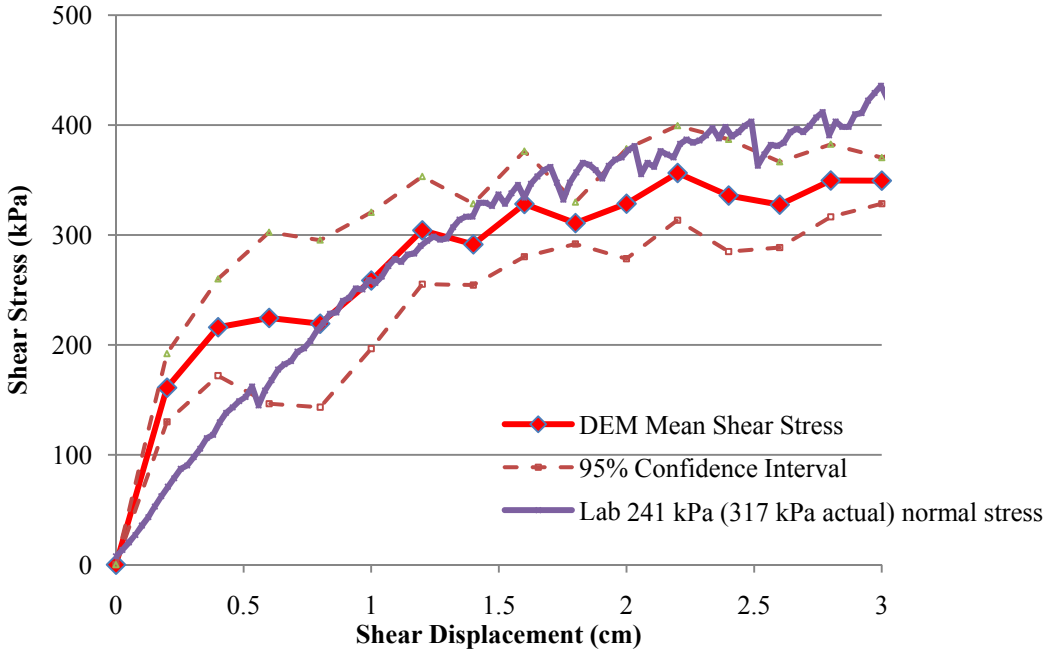

Figure 3.35 Mean Shear Stress and 95% Confidence Interval of DEM Plotted with the Laboratory Result under the Normal Stress of 317 kPa (241 kPa Target)

A reasonably good agreement between the experimental and the DEM simulation results can be observed from Figures 3.30 through 3.35. In Figure 3.36, the Mohr-Coulomb strength envelope from the DEM simulations is plotted together with the strength envelope obtained from the laboratory tests. To further demonstrate that the DEM simulations can predict results similar to the laboratory strength values, or the two envelopes are not significantly different, a statistical study is undertaken.

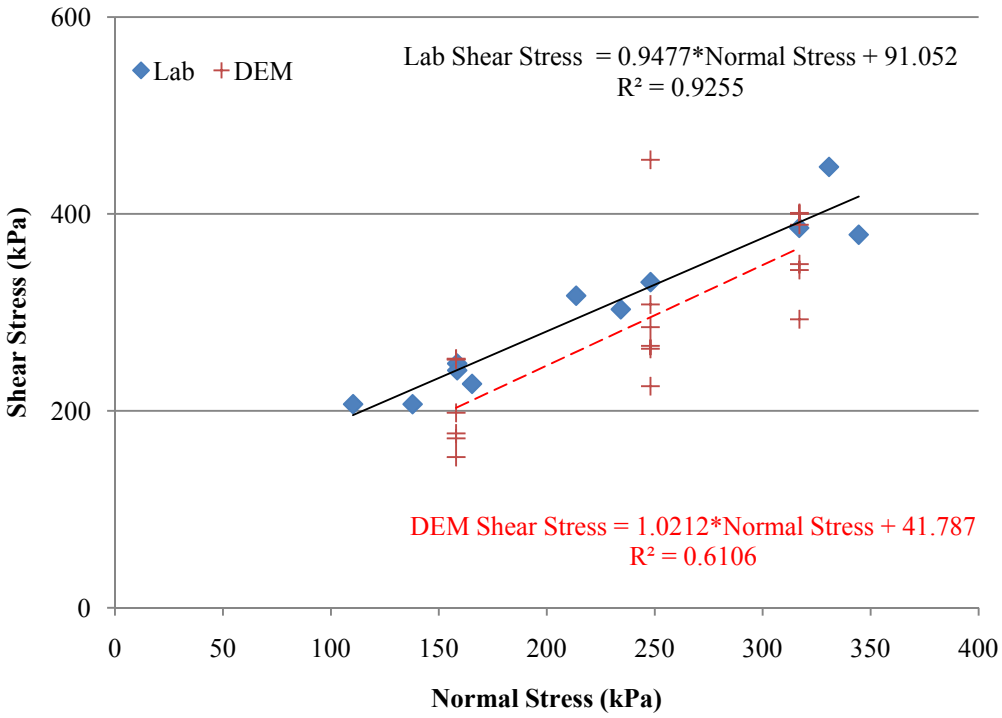

Figure 3.36 Strength Envelopes from Both Laboratory Tests and DEM Simulations

The statistical approach introduced by Neter et al. (1974), Motulsky et al. (2003), and later by Shen (2006) is used in this study to evaluate any differences between these two strength envelopes shown in Figure 3.36. That is to determine if two or several regression curves are different or actually the same. The detailed procedure is explained as follows:

1. Hypothesis: Ho: the regression lines are the same. Ha: the lines are different.
2. Fit each data set and get the total error sum of squares SSE(F)=SSE(lab)+SSE(DEM); and the total degees of freedom df(F)=df(lab)+df(DEM).
3. Mix all data together, fit the combined model under the Ho that all lines are the same and obtain the error sum of squares SSE(R) and degrees of freedom df(R).
4. Calculate the F* statistic by using the equation:

$$F^* = \frac{\mathrm{SSE(R)} - \mathrm{SSE(F)}}{\mathrm{df(R)} - \mathrm{df(F)}} \div \frac{\mathrm{SSE(F)}}{\mathrm{df(F)}} \quad 3.1$$

5. Obtain the p-value by using ANOVA analysis internal function of F probability distribution for two data sets (FDIST).
6. Reject Ho if p-value <= α (0.05 in this study) to conclude the two lines are different. Otherwise, Ho hypothesis that two lines are the same is acceptable (Ott, 2001).

Table 3.6 lists the statistical analysis results and the calculated p-value. Since the p-value (0.22) is larger than α (0.05), from a statistical view, it is concluded that the DEM simulations can accurately predict the laboratory results. In other words, this "Ballast DEM Model" has been validated to simulate large shear box test results for aggregate assembly strength properties.

Table 3.6 Statistical Analysis Results

	LAB		DEM		COMBINED	
	df	*SS*	*df*	*SS*	*df*	*SS*
Regression	1	60664.4	1	79548.19	1	133915.6
Residual	9	4881.622	16	50735.59	27	62819.16
Total	10	65546.02	17	130283.8	28	196734.8
SSE(F)	SSE (R)	*df*(F)	*df* (R)	F*	p	
55617.2091	62819.16	25	27	1.618642	0.218255	

3.3 Summary

In this chapter, a digital image aided particle shape generation for Discrete Element Method is introduced. Element shapes representing aggregate particles from cubical and

angular to flat and elongated and rounded were generated to take into account both aggregate shape properties and the discrete nature of aggregate particle movements. Before validating this approach, a sensitivity analysis was performed to better understand individual influences of major DEM model parameters on the simulation results. Sensitivity study results reveal that the surface friction angle is the most critical parameter among the major DEM model parameters.

Using a proper DEM model calibration approach a contact stiffness combination of 20 MN/m and 10 MN/m for normal and shear, respectively, and a surface friction angle of 31 degrees were selected as model parameters for the clean granite ballast. These parameters produced DEM simulation results statistically similar to the laboratory shear box results for the clean granite to validate the Ballast DEM Model application for large shear box test simulations.

4. FIELD VALIDATION OF THE "BALLAST DEM MODEL"

In the previous chapter, a digital image aided particle shape generation method for DEM is proposed and the "Ballast DEM Model" is validated by large direct shear apparatus in the laboratory. This chapter is intended to provide preliminary field validation using ballast settlement records collected from Transportation Technology Center, Inc (TTCI) Heavy Tonnage Loop (HTL). To link the traffic information including train weight, train speed, and traffic volume to the repeated loading profile applied on the top of a single tie in half track DEM simulation, a dynamic track model is also proposed and derived in this chapter. The ballast settlement prediction extrapolated based on the DEM simulation for the first 1,000 cycles is shown to match the trend of field ballast settlement collected in TTCI HTL tests track.

4.1 TTCI Test Track

There are approximately 77 km (48 miles) of railroad track available for testing locomotives, vehicles, track components, and signaling devices at TTCI, a subsidiary of Association of American Railroads (AAR), Research Center in Pueblo, Colorado. The track includes the following test sections (see Figure 4.1) for different testing purposes: Railroad Test Track (RTT), Transit Test Track (TTT), Facility for Accelerated Service Testing (FAST), High Tonnage Loop (HTL), Wheel Rail Mechanism (WRM), Impact Test Track, and Precision Test Track (PTT).

The HTL is used for track component reliability, wear, and fatigue research under heavy axle loads. Currently the test train in operation with a 39,000 kg (86,667 lb) axle

load. Operations are restricted to a maximum 64 km per hour (40 mph). The HTL is divided into test sections which generally correspond to tangents, spirals, curves (three 5-degree curves and one 6-degree curve), and turnouts. Eight different experiments can be carried out including rail performance, evaluation of ties and fasteners, frogs, turnouts, ballast, and subgrade.

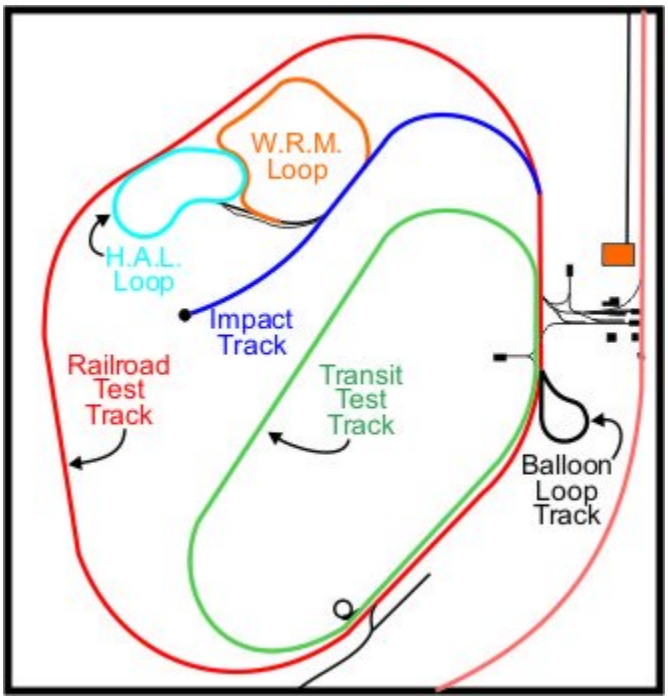

Figure 4.1 TTCI Test Track (Courtesy of Transportation Technology Center, Inc)

4.2 Interpretation of TTCI Traffic Data

Ballast settlement data were collected from previous bridge approach and transition zone study by Li and Davis (2005). Bridge approaches and other track transitions such as road crossings and slab tracks to ballasted tracks are common locations of accelerated track geometry degradation (differential settlement). Accelerated track geometry

degradation in these localized areas can lead to increased costs to railroads due to maintenance, train delays, or speed restrictions. TTCI researchers investigated factors that can cause or accelerate performance problems associated with bridge approach or track transition (Li and Davis, 2005). Test sections included the TTCI heavy tonnage loop and four other bridges from Marysville, Kansas. In this thesis, ballast settlement records after 4-month traffic (see Figure 4.2) were collected from TTCI Heavy Tonnage Loop (HTL) Mile Post 03-1745 (concrete bridge). The recorded settlement of the concrete bridge was the settlement accumulated only in the ballast layer. The traffic information including train weight, speed, and volume per week within this testing period is listed in Table 4.1.

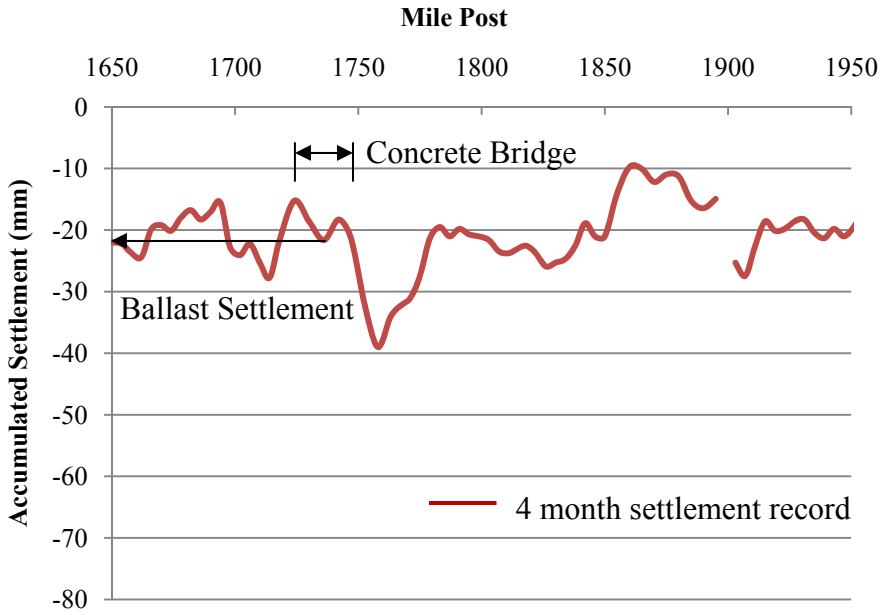

Figure 4.2 Ballast Settlement at TTCI HTL Test Track after 4-Months of Trafficking (Li and Davis, 2005)

Table 4.1 TTCI HTL Test Track Ballast and Traffic Information

Ballast Aggregate Type	Ballast Depth (cm)	Train Speed (km/hr)	Car Weight (kg)	Traffic (cars/week)
Granite	32	64	141,750	42,408

Table 4.1 lists the field traffic data collected from the TTCI test track. However, these values need to be transformed to the force (profile) applied to the top of each individual tie for using in DEM simulations. To that end, a dynamic track model describing a conventional railroad track under moving load is proposed and derived in the following section.

Dynamic Track Model

The history of railroad dynamics is well documented by Knothe and Grassie (1993) and many other railroad researchers. Only analytical track solutions are discussed in this section although significant research has been conducted on the use of numerical methods by several researchers in the past (Diana and Cheli, 1988; Cai and Raymond, 1994; Andersson and Oscarsson, 1999; and Samavedam et al., 1997). Analytical solutions for traditional railroad track structure under moving wheel loading fall into two main categories: (i) continuously supported (Achenbach and Sun, 1965 and Grassie and Cox, 1984), and (ii) discretely supported (Jezequel, 1981; Zhai, 1992; and Kalker 1996). In the case of continuously supported rail, track has been modeled as beam(s) with uniform and

continuous “Winkler” type support. However, when track becomes non-uniform or even discontinuous due to tie or ballast distresses, such as due to missing tie or loss of ballast support, the use of the continuously supported track model becomes troublesome. A typical form of discretely supported track model is a beam supported at the positions of individual ties. If there is sub-ballast or asphalt trackbed installed or in the case of track on bridge, the whole structure is preferably modeled as a “sandwich” type structure, i.e., “beam (rail) on discrete support (ballast) on beam (trackbed, or bridge deck) on Winkler foundation (subgrade)” combination, as illustrated in Figure 4.3.

As shown in Figure 4.3, the rail is modeled as an Euler beam. Each rail pad, tie, and ballast is represented as a system of mass, spring, and damper with designated spacing. The structure underneath ballast is then modeled as another Euler beam on Winkler foundation. By adjusting the properties of the second beam and the foundation, one can approximate different conditions such as when sub-ballast, asphalt trackbed, or bridge deck is installed. A wheel with arbitrary load input moves on the rail at a certain speed. The derivation technique used here is primarily motivated by Kalker’s (1996) work.

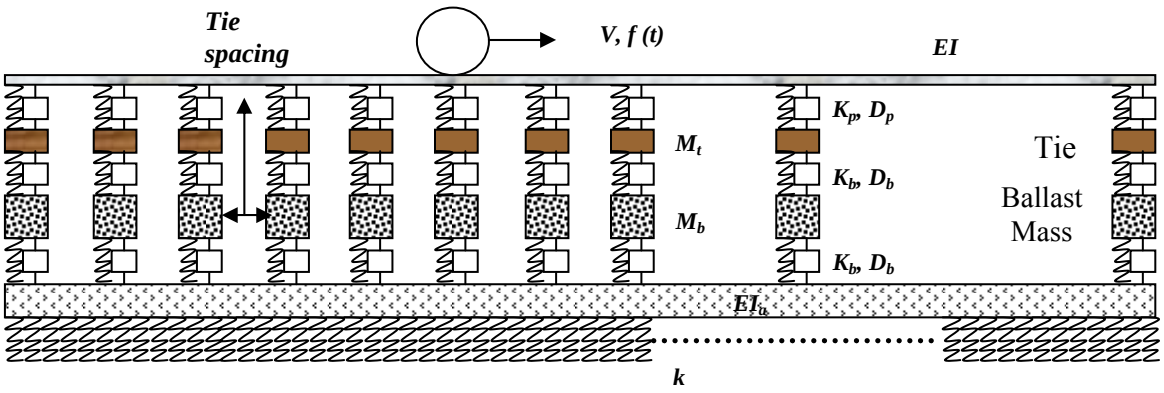

Figure 4.3 "Sandwich" Track Model

To solve this analytical model, it is decomposed into three parts: rail, support (including pad, tie, and ballast), and beam on subgrade which are analyzed separately and later assembled together.

Discrete Support

First, support is derived using the following set of equations:

$$a_m(t) =$$

$$\left(U_r(x_m,t) - U_t(x_m,t)\right)K_p(m) + \left(\dot{U}_r(x_m,t) - \dot{U}_t(x_m,t)\right)D_p(m) \quad (4.1)$$

$$b_m(t) =$$

$$\left(U_b(x_m,t) - U_a(x_m,t)\right)K_b(m) + \left(\dot{U}_b(x_m,t) - \dot{U}_a(x_m,t)\right)D_b(m) \quad (4.2)$$

$$\left(U_r(x_m,t) - U_t(x_m,t)\right)K_p(m) + \left(\dot{U}_r(x_m,t) - \dot{U}_t(x_m,t)\right)D_p(m) - \Big[\left(U_t(x_m,t) - U_b(x_m,t)\right)K_b(m) + \left(\dot{U}_t(x_m,t) - \dot{U}_b(x_m,t)\right)D_b(m)\Big] = M_t(m)\ddot{U}_t(x_m,t) \quad (4.3)$$

$$\left(U_t(x_m,t)-U_b(x_m,t)\right)K_b(m)+\left(\dot{U}_t(x_m,t)-\dot{U}_b(x_m,t)\right)D_b(m)-\Big[\left(U_b(x_m,t)-U_a(x_m,t)\right)K_b(m)+\left(\dot{U}_b(x_m,t)-\dot{U}_a(x_m,t)\right)D_b(m)\Big]=M_b(m)\ddot{U}_b(x_m,t) \quad (4.4)$$

where: $a_m(t)$ is the compression force at the mth tie between rail and support as a function of time; $b_m(t)$ is the compression force at the mth tie between support and asphalt beam as a function of time; $U_r(x_m,t)$ is the rail deflection at the mth tie as a function of time; $U_t(x_m,t)$ is the tie deflection at mth tie as a function of time; $U_b(x_m,t)$ is the ballast deflection (including deformation) at the mth tie as a function of time; $U_a(x_m,t)$ is the second beam deflection at the mth tie as a function of time; $K_p(m)$ is the stiffness of the mth pad; $D_p(m)$ is the damping of the mth pad; $K_b(m)$ is the stiffness of the ballast at the mth tie position; $D_b(m)$ is the damping of the ballast at the mth tie position; $M_t(m)$ is the mass of the mth tie; and $M_b(m)$ is the equivalent mass of ballast underneath the mth tie.

Fourier Transform is performed from time to frequency domain on these equations to express reaction forces in terms of rail and second beam deflections:

$$a_m(\omega)=A_mU_r(x_m,\omega)+B_mU_a(x_m,\omega) \quad (4.5)$$

$$b_m(\omega)=C_mU_r(x_m,\omega)+D_mU_a(x_m,\omega) \quad (4.6)$$

where:

$$A_m=DK_p(m)\left\{1-\frac{1}{\frac{DK_b(m)^2}{DK_p(m)MK_b(m)}-\frac{MK_t(m)}{DK_p(m)}}\right\};$$

$$B_m=\left\{\frac{1}{1-\frac{MK_t(m)MK_b(m)}{DK_b(m)^2}}\right\};$$

$$C_m = DK_b(m)\left\{\frac{1}{\frac{MK_t(m)MK_b(m)}{DK_p(m)DK_b(m)} - \frac{DK_b(m)}{DK_p(m)}}\right\};$$

$$D_m = -DK_b(m)\left\{1 + \frac{1}{\frac{MK_b(m)}{DK_b(m)} - \frac{DK_b(m)}{MK_t(m)}}\right\};$$

and: $DK_p(m) = K_p(m) + i\,\omega D_p(m)$; $DK_b(m) = K_b(m) + i\,\omega D_b(m)$; $MK_t(m) = M_t(m)\omega^2 - DK_p(m) - DK_b(m)$; $MK_b(m) = M_b(m)\omega^2 - 2DK_b(m)$.

Rail Beam

For rail, the following equation governs:

$$EIU_r(x,t)'''' + \rho U_r(\ddot{x},t) + \varepsilon U_r(\dot{x},t) + TU_r(x,t)'' =$$

$$f(t)\delta(x - vt) - \sum_m a_m(t)\delta(x - x_m) \qquad (4.7)$$

where: EI is the bending stiffness of rail; $U_r(x,t)$ is the rail deflection as a function of time; ρ is the unit mass of rail; ε is damping of rail itself which will be set to zero for convenience; T is the rail axial force caused by temperature increase; $f(t)$ is the wheel load function; δ is the delta function; x_m is the location of the mth tie; and v is the wheel speed.

Performing Fourier Transform both from time to frequency and from "x" coordinate to wave length on Equation (4.7) yields:

$$K(\lambda,\omega)U_r(\lambda,\omega) = f^t(\lambda v + \omega) - \sum_m a_m(\omega)e^{-ix_m\lambda} \qquad (4.8)$$

where f^t represents the Fourier Transformation from time to frequency; and $K(\lambda,\omega) = [EI\lambda^4 - T\lambda^2 - \omega^2\rho + i\varepsilon\omega]$. So:

$$U_r(\lambda,\omega)=\frac{1}{K(\lambda,\omega)}\left[f^t(\lambda v+\omega)-\sum_m a_m(\omega)e^{-ix_m\lambda}\right] \tag{4.9}$$

By applying Convolution Theorem and Inverse Fourier Transform, we obtain:

$$U_r(x,\omega)=\int_{-\infty}^{\infty} inv\left[f^t(\lambda v+\omega)-\sum_m a_m(\omega)e^{-ix_m\lambda}\right]K_r(x-y,\omega)dy \tag{4.10}$$

where

$$K_r(x,\omega)=inv\left[\frac{1}{K(\lambda,\omega)}\right]$$

and "inv" is the inverse Fourier transformation from wave length back to "x" coordinate.

Since

$$inv[f^t(\lambda v+\omega)]=\frac{1}{2\pi}\int_{-\infty}^{\infty} f^t(\lambda v+\omega)\,e^{ix\lambda}d\lambda \tag{4.11}$$

$$inv[f^t(\lambda v+\omega)]=\tfrac{1}{2\pi}\textstyle\int_{-\infty}^{\infty} f^t(Y)\frac{1}{v}e^{ixY/v}e^{-i\omega x/v}dY \tag{4.12}$$

So

$$inv[f^t(\lambda v+\omega)]=\frac{1}{v}f\left(\frac{x}{v}\right)e^{-\frac{i\omega x}{v}} \tag{4.13}$$

Also

$$inv\left[\sum_m a_m(\omega)e^{-ix_m\lambda}\right]=\sum_m a_m(\omega)\delta(x-x_m) \tag{4.14}$$

So,

$$U_r(x,\omega)=\int_{-\infty}^{\infty}\frac{1}{v}f(\frac{y}{v})e^{-i\omega y/v}K_r(x-y,\omega)dy$$

$$-\int_{-\infty}^{\infty}\sum_m a_m(\omega)\delta(y-x_m)K_r(x-y,\omega)dy \tag{4.15}$$

For $K_r(x,\omega)$,

$$K_r(x,\omega) = \frac{1}{2\pi}\int_{-\infty}^{\infty} \frac{e^{ix\lambda}}{EI\lambda^4 - T\lambda^2 - \omega^2\rho + i\varepsilon\omega} d\lambda \tag{4.16}$$

Use Residue Theorem and Jordan's Lemma and assume that "ε" becomes zero to solve this integral,

For $\omega > 0$:

$$K_r(x,\omega) = -\frac{1}{4EIR\sqrt{R^2 - r^2}}\left(\sqrt{R-r}\, e^{-|x|\sqrt{R+r}} + i\sqrt{R+r}\, e^{-i|x|\sqrt{R-r}}\right) \tag{4.17}$$

where $R = \sqrt{r^2 + \omega^2 l^2}$; $r = \frac{T}{2EI}$; $l = \sqrt{\frac{\rho}{EI}}$.

For $\omega < 0$, $K_r(x,\omega)$ is the complex conjugate of the previous solution.

The situation of $\omega = 0$ will be discussed later. To further solve this problem, the wheel load function $f(t)$ is assumed to have exponential behavior in a time period from 0 to l

$$f(t) = P_0(d - c\cos at); 0 < t < l \tag{4.18}$$

So the first term in Equation (4.15) becomes

$$\int_{-\infty}^{\infty} \frac{1}{v} f\left(\frac{y}{v}\right) e^{-\frac{i\omega y}{v}} K_r(x-y,\omega)$$

$$= \frac{P_0}{-4EIR\sqrt{R^2 - r^2}} \int_{-\infty}^{\infty} \frac{1}{v}\left(d - \frac{c}{2}e^{\frac{iay}{v}} - \frac{c}{2}e^{-\frac{iay}{v}}\right) e^{-\frac{i|\omega|y}{v}}\left(e^{-|x-y|\sqrt{R+r}}\right.$$

$$\left. + i\sqrt{R+r}\, e^{-i|x-y|\sqrt{R-r}}\right) dy \tag{4.19}$$

Further

$$\int_{-\infty}^{\infty} \frac{1}{v} f\left(\frac{y}{v}\right) e^{-\frac{i\omega y}{v}} K_r(x-y,\omega) dy$$

$$= \frac{P_0}{-4EIR\sqrt{R^2 - r^2}}\left[dg(0) - \frac{c}{2}\, g(a) - \frac{c}{2}\, g(-a)\right] \tag{4.20}$$

where

$$g(z) = \int_0^{vl} e^{\frac{izy}{v} - \frac{i|\omega|y}{v} - |x-y|\sqrt{R+r}} \sqrt{R-r}$$

$$+ ie^{\frac{izy}{v} - \frac{i|\omega|y}{v} - i|x-y|\sqrt{R-r}} \sqrt{R+r} dy \tag{4.21}$$

In the end, deflection of rail in the frequency domain can be expressed as:

$$U_r(x,\omega) = F(x,w) - \sum_m a_m(\omega) K_r(x - x_m, \omega) \tag{4.22}$$

where $F(x,w)$ is the result from Equation 4.20.

The Second Beam

For the second beam, the governing equation is shown as follows:

$$EI_a U_a(x,t)'''' + pU_a(\ddot{x},t) + cU_a(\dot{x},t) + kU_a(x,t) = \sum_m b_m(t)\delta(x - x_m) \tag{4.23}$$

where: EI_a is the bending stiffness of the second beam; p is the unit mass of the second beam; c is the damping of the second beam; and k is the subgrade modulus.

Similar to what was used in rail equation, Equation (4.23) can be transformed to

$$U_a(\xi,\omega) = \frac{1}{EI_a\xi^4 + k - p\omega^2 + ic\omega} \sum_m b_m(\omega) e^{-ix_m\xi} \tag{4.24}$$

Transforming Equation 4.24 back from wave length to "x" coordinate yields

$$U_a(x,\omega) = \sum_m b_m(\omega) K_a(x - x_m, \omega) \tag{4.25}$$

where

$$K_a(x,\omega) = \frac{1}{2\pi} \int_{-\infty}^{\infty} \frac{e^{ix\xi}}{EI_a\xi^4 + k - p\omega^2 + ic\omega} d\xi \tag{4.26}$$

Use Residue Theorem and Jordan's Lemma again to solve Equation 4.26

For $|\omega| < \sqrt{\frac{k}{p}}$:

$$K_a(x,\omega) = \frac{\sin(\Delta|x|) + \cos(\Delta|x|)}{8EI_a\Delta^3 e^{\Delta|x|}} \tag{4.27}$$

For $|\omega| > \sqrt{\frac{k}{p}}$:

$$K_a(x,|\omega|) = -\frac{e^{-|x|\nabla} + ie^{-i|x|\nabla}}{4EI_a\nabla^3} \tag{4.28}$$

$$K_a(x,-|\omega|) = -\frac{e^{-|x|\nabla} - ie^{i|x|\nabla}}{4EI_a\nabla^3} \tag{4.29}$$

where: $\Delta = \sqrt[4]{\frac{k-p\omega^2}{4EI_a}}$; $\nabla = \sqrt[4]{\frac{p\omega^2-k}{EI_a}}$. The situation when $|\omega| = \sqrt{\frac{k}{p}}$ will be explained later.

Model Assemble

It can be seen that deflection of rail and asphalt beam at any position are functions of force vectors $\{a_m\}$ and $\{b_m\}$ (see Equations 4.5, 4.6, 4.22 and 4.25). To solve these two vectors, deflections at each support need to be solved. By substituting deflections at each support into Equations 4.22 and Equation 4.25, they can be expressed in matrix forms:

$$\begin{Bmatrix} U_r(x_1,\omega) \\ U_r(x_2,\omega) \\ \vdots \\ U_r(x_{m,}\omega) \end{Bmatrix}$$

$$= \begin{Bmatrix} F(x_1,\omega) \\ F(x_2,\omega) \\ \vdots \\ F(x_m,\omega) \end{Bmatrix}$$

$$- \begin{bmatrix} A_1K_r(x_1-x_1,\omega) & A_2K_r(x_1-x_2,\omega) & \dots & A_mK_r(x_1-x_m,\omega) \\ A_1K_r(x_2-x_1,\omega) & A_2K_r(x_2-x_2,\omega) & \dots & A_mK_r(x_2-x_m,\omega) \\ \vdots & \vdots & \dots & \vdots \\ A_1K_r(x_m-x_1,\omega) & A_2K_r(x_m-x_2,\omega) & \dots & A_mK_r(x_m-x_m,\omega) \end{bmatrix} \begin{Bmatrix} U_r(x_1,\omega) \\ U_r(x_2,\omega) \\ \vdots \\ U_r(x_{m,}\omega) \end{Bmatrix}$$

$$- \begin{bmatrix} B_1K_r(x_1-x_1,\omega) & B_2K_r(x_1-x_2,\omega) & \dots & B_mK_r(x_1-x_m,\omega) \\ B_1K_r(x_2-x_1,\omega) & B_2K_r(x_2-x_2,\omega) & \dots & B_mK_r(x_2-x_m,\omega) \\ \vdots & \vdots & \dots & \vdots \\ B_1K_r(x_m-x_1,\omega) & B_2K_r(x_m-x_2,\omega) & \dots & B_mK_r(x_m-x_m,\omega) \end{bmatrix} \begin{Bmatrix} U_a(x_1,\omega) \\ U_a(x_2,\omega) \\ \vdots \\ U_a(x_{m,}\omega) \end{Bmatrix} \quad (4.30)$$

and

$$\begin{Bmatrix} U_a(x_1,\omega) \\ U_a(x_2,\omega) \\ \vdots \\ U_a(x_{m,}\omega) \end{Bmatrix}$$

$$= \begin{bmatrix} C_1K_a(x_1-x_1,\omega) & C_2K_a(x_1-x_2,\omega) & \dots & C_mK_a(x_1-x_m,\omega) \\ C_1K_a(x_2-x_1,\omega) & C_2K_a(x_2-x_2,\omega) & \dots & C_mK_a(x_2-x_m,\omega) \\ \vdots & \vdots & \dots & \vdots \\ C_1K_a(x_m-x_1,\omega) & C_2K_a(x_m-x_2,\omega) & \dots & C_mK_a(x_m-x_m,\omega) \end{bmatrix} \begin{Bmatrix} U_r(x_1,\omega) \\ U_r(x_2,\omega) \\ \vdots \\ U_r(x_{m,}\omega) \end{Bmatrix}$$

$$+ \begin{bmatrix} D_1K_a(x_1-x_1,\omega) & D_2K_a(x_1-x_2,\omega) & \dots & D_mK_a(x_1-x_m,\omega) \\ D_1K_a(x_2-x_1,\omega) & D_2K_a(x_2-x_2,\omega) & \dots & D_mK_a(x_2-x_m,\omega) \\ \vdots & \vdots & \dots & \vdots \\ D_1K_a(x_m-x_1,\omega) & D_2K_a(x_m-x_2,\omega) & \dots & D_mK_a(x_m-x_m,\omega) \end{bmatrix} \begin{Bmatrix} U_a(x_1,\omega) \\ U_a(x_2,\omega) \\ \vdots \\ U_a(x_{m,}\omega) \end{Bmatrix} \quad (4.31)$$

Equations 4.30 and 4.31 are simplified as

$$\begin{bmatrix} AK_r + I & BK_r \\ CK_a & DK_a - I \end{bmatrix} \begin{Bmatrix} U_r(x_{1\dots m},\omega) \\ U_a(x_{1\dots m},\omega) \end{Bmatrix} = \begin{Bmatrix} F(x_{1\dots m},\omega) \\ 0 \end{Bmatrix} \quad (4.32)$$

Solving Equation 4.32 yields deflections of rail at points of support. Deflections of rail at any position can be obtained by substituting results from Equation 4.32 into Equations 4.5, 4.6, 4.22 and 4.25. It is worth noting that the derivations so far are in the frequency domain. Fast Fourier Transform (FFT) needs to be performed to transform the solutions back to time domain.

In the situations when $|\omega| = 0 \; and \; |\omega| = \sqrt{\frac{k}{p}}$, deflection in frequency appears to be a delta function and can be treated as a constant value in time domain. This constant is calculated based on the assumption that after certain time all deflections of the track will fade to zero.

Force on Top of the Tie

With this derived solution, a computer program was developed and used to calculate the load profile applied on the top of each individual tie. The TTCI test track segment had 30 ties spaced at 0.508 m. The wheel load function $f(t)$ in this case is a constant (177187 N) representing a single wheel load computed from the self-weight of a 141750 kg (315 kip) car. The wheel load is moving at a speed of 17.8 m/s. The rail unit mass is 59 kg/m with a bending stiffness of 4.9 MN/m^2. Each of the pad, tie, and ballast were set to a typical pad stiffness value of 280 MN/m; pad damping value of 63 kNsec/m; ballast stiffness value of 70 MN/m; ballast damping value of 82 KNsec/m; tie mass of 45 kg; and equivalent ballast mass of 420 kg (half track). The bending stiffness of the second beam and the stiffness of the subgrade soil have been set to a very high value to represent the case of track on concrete bridge (TTCI test track MP 03-1745).

Figure 4.4 shows the loading profile on the top of a single tie. It is worth noting that the profile given in Figure 4.4 is the result after superposition of four running wheels which is equivalent to the traffic of one car passing.

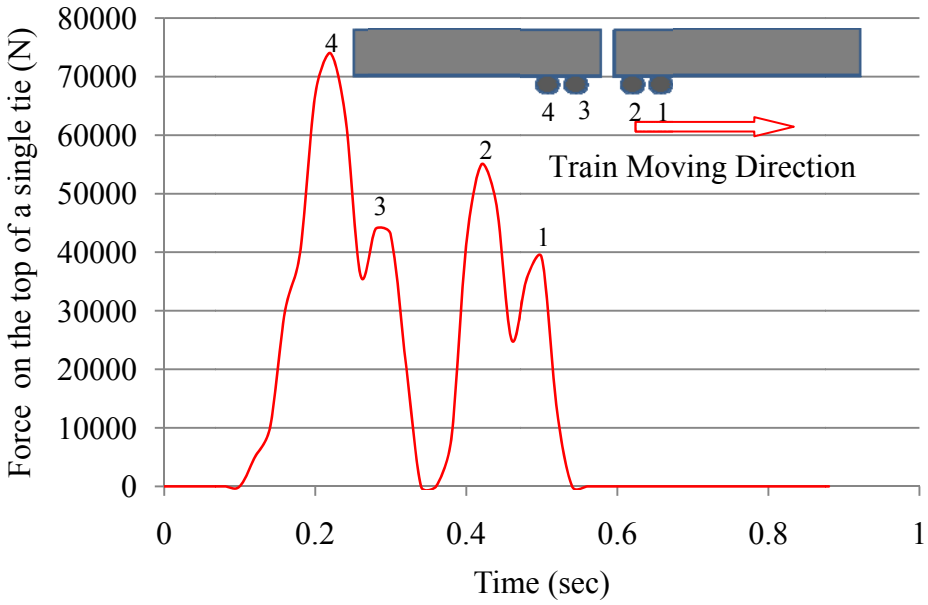

Figure 4.4 Load Profile on Top of a Single Tie under Moving Train Load

4.3 Half Track DEM Settlement Simulation under Repeated Moving Load

With the load profile on top of the single tie obtained from the interpretation results of the TTCI traffic data using dynamic track model it is time to generate the ballast DEM model and run the settlement simulation. To simulate the realistic aggregate size distribution and shape properties, a granite type of aggregate sample was also collected from the same TTCI Mile Post 03-1745 where the settlement was recorded. Aggregates were then scanned through the UIAIA to obtain the size distribution and shape properties. Figure 4.5 shows the size distribution of the ballast aggregate sample. Also, an average

AI of 521 and F&E ratio of 1.2:1 were obtained from the digital image analysis. Therefore, representative element shape from Library 2 (AI=570; F&E=1:1) is chosen to properly simulate the ballast aggregate shape.

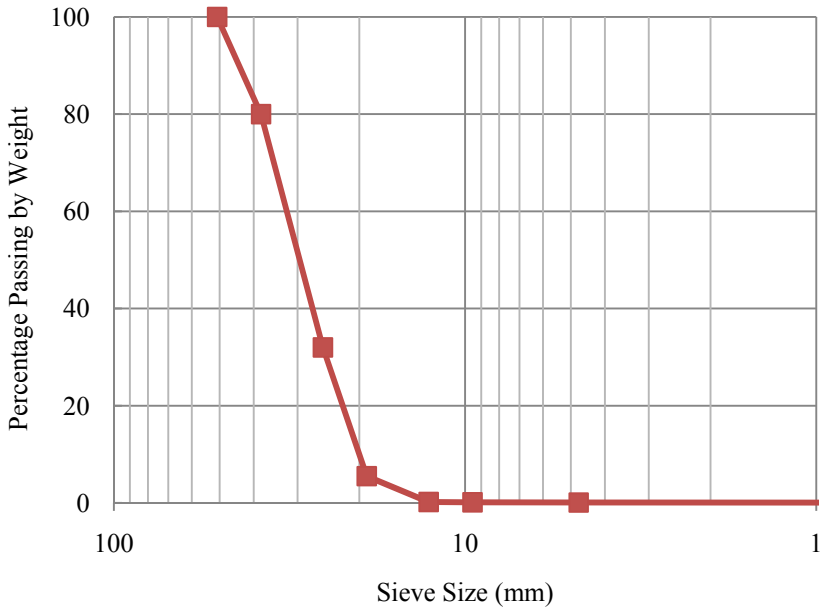

Figure 4.5 Gradation of Ballast Sample from TTCI HTL Test Track MP 03-1745

With all the pertinent data obtained including shape, size, loading profiles on the top of a single tie, the traffic within 4 months, and the DEM model parameter validated in Chapter 3 for granite ballast, half track DEM settlement simulation is conducted.

Half Track DEM Simulation and Results

The ballast box test proposed by Norman (1982) was originally used for ballast field strength and settlement testing purposes in the laboratory (Steward et al, 1985). Accordingly, a ballast box with similar dimensions was selected for a single tie-ballast effective contact area. In this study, the length of the ballast simulation domain was set

to be the same as the length of the ballast box which was equal to the tie spacing. Figure 4.6 shows the plan view of the simulation setup with the half tie length and a corresponding ballast width of 0.61 m assigned instead of 0.3 m used the in ballast box test by Norman. This way, the simulation adequately considered the ballast shoulder movement. Figure 4.7 shows the ballast settlement prediction setup using DEM program BLOKS3D. The ballast sample was compacted by creating a large DEM block element covering the top of the ballast and pushing downwards until an air voids content of 38% was achieved for the rigid bottom boundary case representing concrete bridge deck.

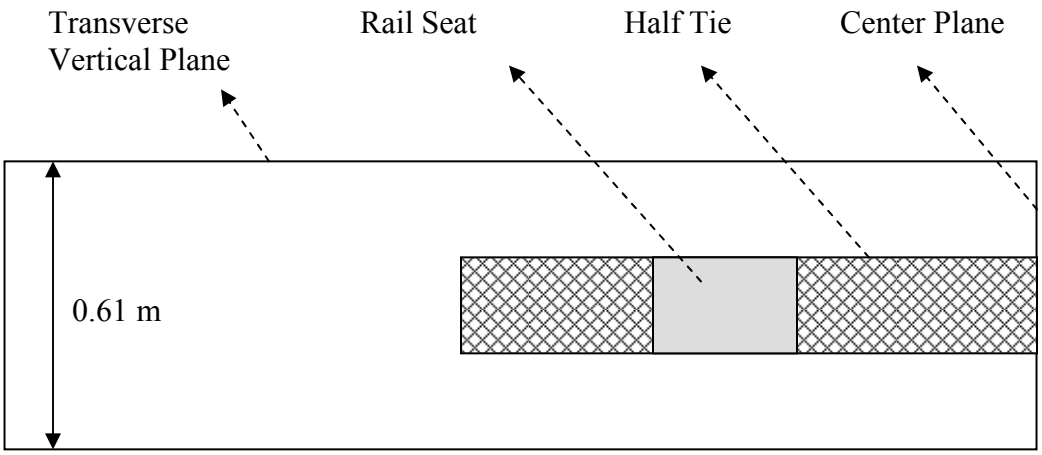

Figure 4.6 Plan View of Ballast Settlement DEM Simulation

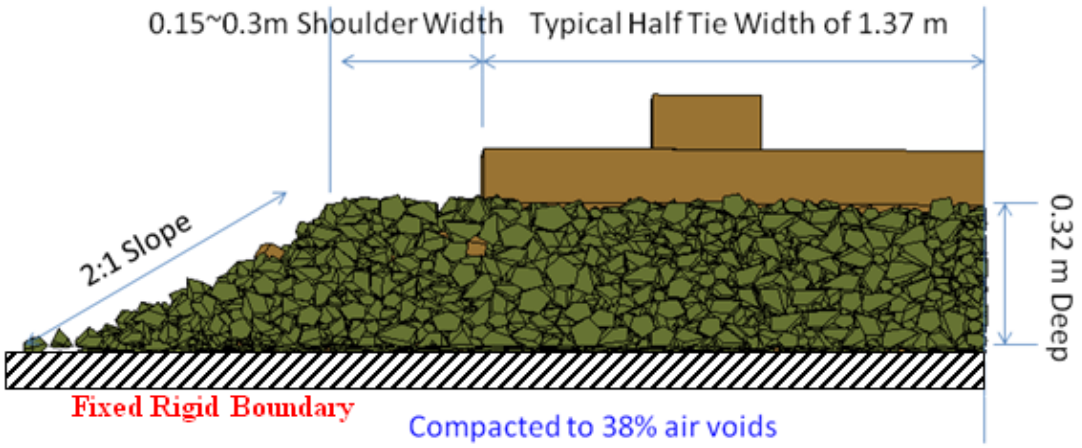

Figure 4.7 DEM Setup for TTCI Half Track Settlement Simulation

After setting up the half track ballast DEM model with similar aggregate shape, size distribution and the exact track geometry, load profile shown in Figure 4.4 is repeatedly applied on the top of the tie and the settlement of the tie is recorded.

Figure 4.8 shows the settlement or rutting profile accumulated in 1000 cycles. The trend line regressed by using commonly used "Rut Depth" power model has a very high coefficient of determination (R^2=0.999), which implies that the ballast settlement trend in the field can be accurately reflected by "Ballast DEM Model". Also, by extrapolating the accumulated settlement regression curve to the 4-months of traffic (678,528 cycles), one can predict an accumulated settlement (0.029 m) after 4-months traffic which is close to the field observation of 0.023 m (see Figure 4.2). However, the reliability and accuracy of the extrapolation is questionable since the extrapolation period is much longer than the data obtained from DEM. Therefore, a more detailed field ballast settlement record with many more individual settlement data points might be needed in the future to be able to better validate this "Ballast DEM Model" in the field.

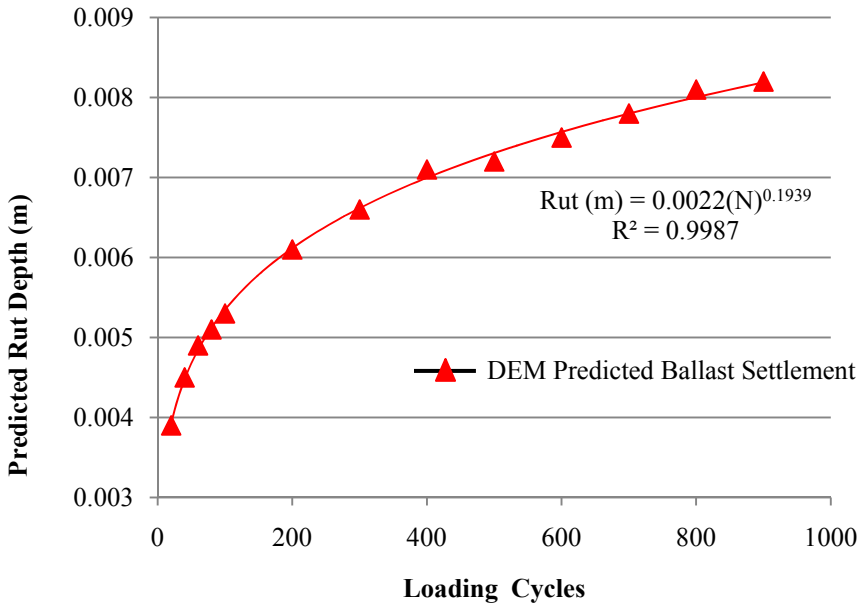

Figure 4.8 DEM Prediction of Ballast Settlement after 1000 cycles

4.4 Summary

In this chapter, the "Ballast DEM Model" was used to predict actual field ballast settlement using a DEM half track settlement simulation. Settlement records as well as traffic information including train weight, speed and volume were collected from Transportation Technology Center, Inc. (TTCI) Heavy Tonage Loop (HTL). The ballast aggregate sample was also collected and analyzed for size and shape properties using UIAIA. A dynamic track model was derived to link the traffic information to the load input on top of the tie for DEM simulation. The size and shape properties of the ballast aggregate sample quantified using UIAIA were utilized to determine the representative element shapes used in DEM settlement simulation. From the settlement results predicted by DEM, it is concluded that: 1) The "Ballast DEM Model" predicts the settlement trend

in the field reasonably, and 2) more frequent field settlement data collection will be needed to better validate the “Ballast DEM Model”.

5. EFFECT OF AGGREGATE GRADATION ON BALLAST PERFORMANCE

In this chapter, the validated "Ballast DEM Model" is used to evaluate the gradation effect on both ballast void space and load carrying performances. The effect of gradation on aggregate assembly volumetric properties is studied first. Full-scale ballast layers with common gradations listed in AREMA specifications for main line railroads are generated. Repeated train loading is simulated with the different AREMA gradation ballast layers to investigate the adequacy of drainage and structural performances by means of comparing ballast settlements occurred after application of a certain volume of traffic. More uniformly graded aggregate assemblies generally have larger air voids thus better drainage. However, such uniform particles at certain sizes might tend to dilate under loading thus creating an unstable ballast particle packing and void structure. The DEM approach is used effectively to identify differences in current ballast specifications in terms of drainage and structural support and provide insight into optimizing ballast layer aggregate gradations for improved railroad track performance.

5.1 Introduction

Railroad ballast is uniformly-graded coarse aggregate placed between and immediately underneath the crossties. The purpose of ballast is to provide drainage and structural support for the heavy loading applied by trains. Aggregate size distribution (gradation) and particle shape are two major considerations in ballasted railroad track design. Superior ballast aggregate shape properties such as by an angular crushed stone

have been proven to be critical for ballast strength and stability. Yet, impacts of different AREMA gradations on functional performance of ballast have not been fully explored. Such an investigation of proper ballast gradation design should require large enough voids for providing adequate drainage. At the same time, load carrying through contacting aggregate particles and related structural performance should not be compromised. By adjusting the percentages of aggregates at different sizes, ballast gradations can be optimized at the microstructure level for large enough void space and adequate structural performance.

5.2 Maximum Density and Characteristic Gradation Curves

It is usually assumed that the "preferred" gradation is one that produces the maximum density which creates more particle-to-particle contact and hence increase the structural stability. A widely used equation to describe a maximum density gradation was developed by Fuller and Thompson (1907) which, sometimes, is also referred to as Talbot Equation (Equation 2.1). Later, the FHWA introduced the standard gradation graph used in the HMA industry today. This graph uses n = 0.45 and is convenient for determining the maximum density line and adjusting gradation (Roberts et al., 1996). This graph shown in Figure 5.1 is slightly different than other gradation charts because it uses the sieve size raised to the n^{th} power (usually 0.45) as the x-axis units. Thus, the maximum density line appears as a straight line from zero to the maximum aggregate size for the mixture being considered (solid line in Figure 5.1). For railroad ballast, maximizing the density will obviously minimize the function of drainage. Nevertheless, maximum density gradation still provides a datum to start with.

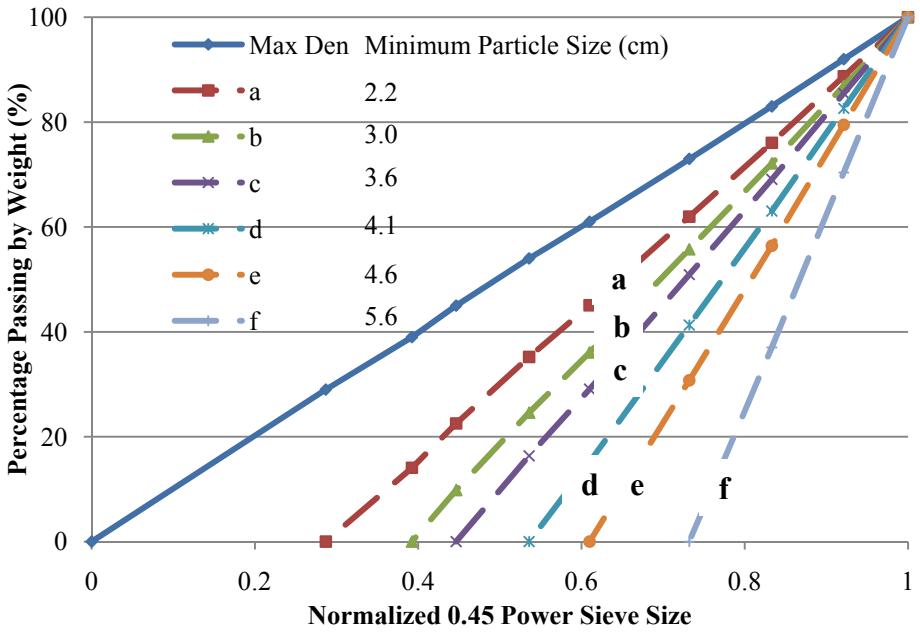

Figure 5.1 Normalized 0.45 Power Gradation Chart

The diagonal solid line in Figure 5.1 is the normalized gradation commonly considered as the gradation that produces the maximum density. From this maximum density line, one can calculate the weight percentage corresponding to any particles size, thus prepare sample with maximum density and stability.

For a sample with gradation of maximum density, it can be proven that if one eliminates all the particles smaller than a randomly chosen size, the gradation curve for the rest of the particles still remains a straight line plotted in the 0.45 power chart. However, depending on the minimum size chosen, the gradation line will have different slopes in the 0.45 power gradation chart (dashed lines in Figure 5.1). The slope of the gradation line increases with increasing of the minimum size. In other words, the

aggregate becomes more uniformly graded when the positive slope of the gradation line increases. These gradation lines with different minimum particle sizes are named as "characteristic gradation curves" in this paper. Their effects on aggregate assembly volumetric properties and the structural layer support characteristics will be further investigated in the following section.

5.3 Commonly Used Ballast Gradations

Although ballast is normally treated as uniformly graded material, there are different gradations for ballast around the world. Figure 5.2 shows typical ballast gradations used in Australia (RIC and Queensland), in France, and in the US, i.e. those of the AREMA No. 24, No. 3, and No. 4 gradations. Recent findings suggested a change from more uniform gradations towards well graded ones might reduce ballast settlement potentials (Indraratna and Salim, 2005).

From Figure 5.2, both RIC and Queensland of the Australian ballast gradations, the French gradation, and the AREMA No.3 are somewhat similar in terms of particle size distribution. AREMA No. 4 gradation falls on the left side to represent a similar size distribution with a smaller maximum size. On the other hand, AREMA No. 24 ballast is very different from other gradations; it has not only a different maximum particle size but also a different size distribution.

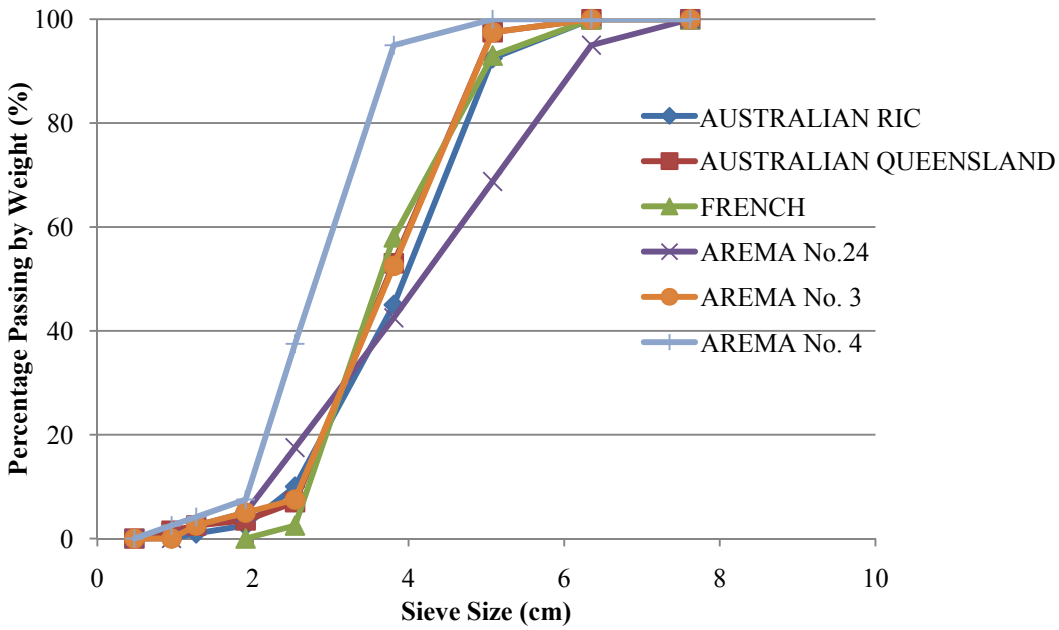

Figure 5.2 Common Ballast Gradations

Figure 5.3 shows the common gradations from Figure 5.2 this time plotted in the normalized 0.45 power gradation chart. The Queensland and AREMA No.4 gradations indeed have the same particle size distributions which are very close to the "characteristic gradation curve" "f" (see Figure 5.3). However, AREMA No.24 gradation has a different size distribution close to curve "e". It implies that No.24 is more densely graded than the other gradations. It is worth noticing that commonly existing gradations have small "tails" in the left (Figure 5.3) representing around 5% or less fine aggregates by weight, which is considered not significant since most of them will not affect the contacts among large aggregates. In the following section, "Ballast DEM Model" is used to investigate the effect of gradation on ballast volumetric properties and settlement performances in accordance with the introduced concept of "characteristic gradation curves."

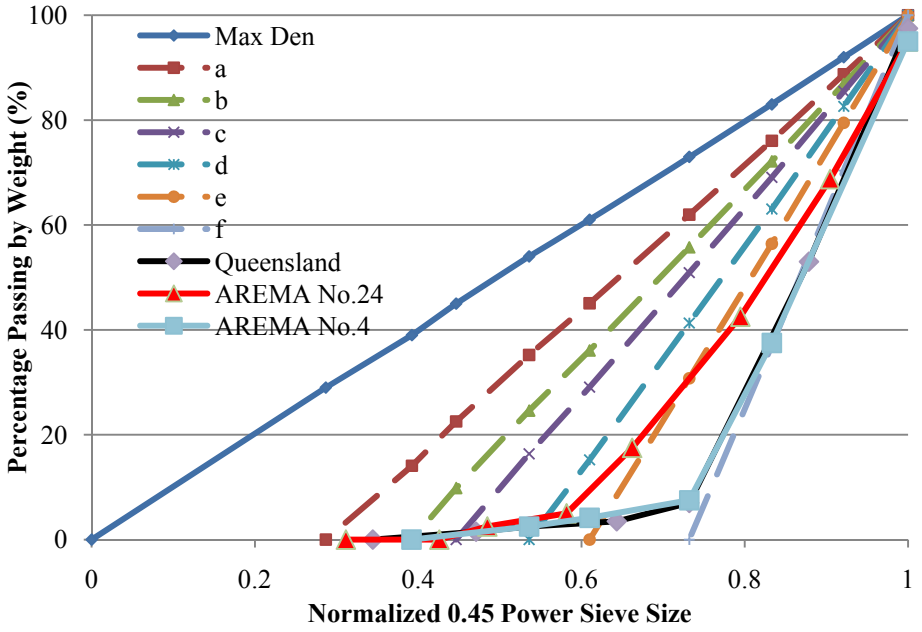

Figure 5.3 Common Gradations Plotted in the Normalized 0.45 Power Gradation Chart

5.4 DEM Simulations for Determining Air Voids Content

In BLOKS3D, a cylindrical container was generated with a diameter of 30.5 cm and 100 cm in height to conduct air void test DEM simulations. The maximum particle size considered was 7.6 cm for all samples with gradation curves represented from "a" to "f" for various minimum size categories. The ballast gradation samples were generated (see Figure 5.4) and tested in accordance to the following DEM test procedure:

1. Generate aggregate particles as discrete elements (Kn = 20MN/m; Ks = 10MN/m; $\theta = 31^{o}$) with the same angularity (AI=570, F&E Ratio = 1:1) and surface texture

properties and drop them in layers, using a gravity constant of 9.8 m/s^2, into the cylindrical container also generated as a discrete element;

2. Switch the gravity constant between "+" and "–" 9.8 m/s^2 a few times to obtain a uniformly packed assembly.
3. Change the gravity constant to -50 m/s^2 to compact samples.
4. Delete particles above the same height of 61 cm for all samples so that all the different aggregate characteristic gradation curves studied have samples with the same total volume of 0.046 m^3. Given the specific gravity of particles, compute the weight of the sample and the sample air voids content.

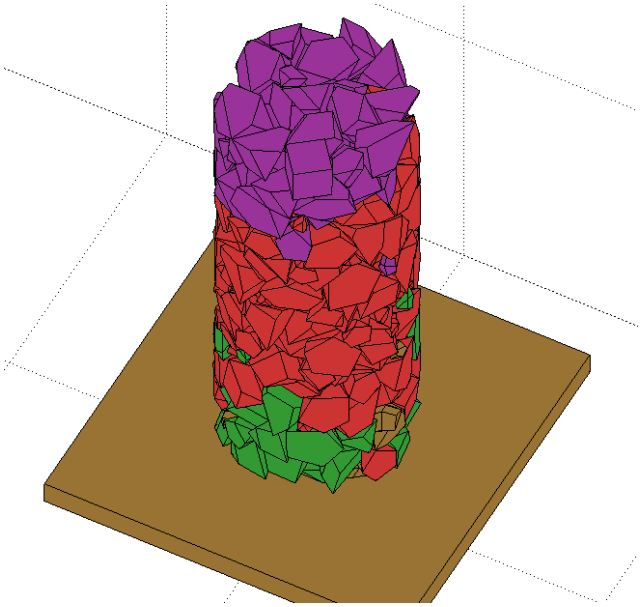

Figure 5.4 A Typical Cylindrical Sample for Air Voids Determination in DEM

For determining the sample air voids of each gradation, the DEM simulations were repeated twice. Accordingly, Table 5.1 lists the minimum particle sizes for samples with

gradations from “a” to “f” and the mean air voids for all 6 samples of these characteristic gradation curves.

From Table 5.1, it can be seen that gradation “f” yields the highest air voids content. It is also conceivable that when the minimum particle size decreases, i.e., gradation shifts from “f” to “c,” the air voids decreases due to the presence of the finer particles. It is worth noticing that a further decrease in the minimum particle size from gradation “c” to “a,” this time, increases the air voids content. This phenomenon can be explained by the illustration on particle packing scenarios in Figure 5.5 corresponding to different gradations. Scenario (1) represents more or less uniform gradation, i.e. gradation “f”. It is obvious that this packing form would yield the largest air voids. When gradation shifts from “f” to “c” this gradually introduces finer particles and the resulting air voids content gets smaller (scenario 2). Further adding finer particles, as in scenario (3), the contacts among larger particles are severed and those large particles are separated apart by finer particles filling the matrix thus causing an expansion or increase in the void space. This is believed to be the reason why gradations “a” and “b” generated higher air voids than gradations “c” to “f.” As shown in Figure 6, it is also reasonable to rate scenario (3) as an “unstable” packing and void structure stage which may be susceptible to ballast particle rearrangement under applied train loading. In any case, scenario (4) represents the case of the maximum density at which stage fine particles fill a considerable portion of the void structure created by larger particles and hence yields the densest packing.

Table 5.1 Minimum Particle Size and Air Voids for Ballast with Characteristic Gradations

Characteristic Gradation Curve	Minimum Particle Size (cm)	Mean * Air Voids Content
a	2.2	0.3514
b	3.0	0.3508
c	3.6	0.3463
d	4.1	0.3539
e	4.6	0.3573
f	5.6	0.3669

* Average of 2 test simulations

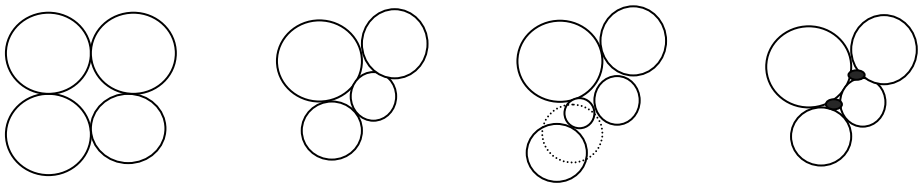

(1) (2) (3) (4)

Figure 5.5 Particle Packing Scenarios (spherical particles sketched for simplicity)

5.5 DEM Simulations for Ballast Layer Settlement

To evaluate the structural performances of full-scale ballast layers with different gradations, DEM settlement simulations were conducted next using the BLOKS3D

program. In the railroad track DEM model, half track simulations were prepared by constructing the ballast layer with aggregate particles having the same shape properties but at different gradations. The dimension of the half track model is set to be the same as the half track model described in Chapter 4 (see Figure 4.7). The ballast layer was then compacted by the same compaction effort. This was accomplished by creating a DEM block element covering the top of the ballast and pushing downward with a force of 100 kN until no particle movement was observed. The railroad tie was then generated and placed on top of the ballast. Loads derived from the dynamic track model with the profile shown in Figure 4.4 are applied on the top of the tie.

Figure 5.6 shows the settlement predictions of the six different ballast characteristic gradation curve samples graphed with repeated loading cycles. Note that gradation "d" yields the least amount of settlement after 300 cycles of repeated loading. When gradation becomes more uniform, i.e., as it moves from "d" to "f," the ballast produces more and more settlement. It is interesting to note that the ballast with gradation "c" has more or less the same settlement as the ballast with gradation "d." On the other hand, the ballasts with gradations "a" and "b" clearly yield higher settlements than gradation "d" under repeated loading and have less structural support. This result is consistent with the volumetric properties reported previously. Hence, gradation curve "c" falls at the boundary with its minimum particle size of 3.6 cm (see Table 5.1) beyond which ballast may become structurally undesirable and prone to settlement.

These results are consistent with conclusions drawn from laboratory research concluded by Indraratna et al. (2004). It was concluded from their research that "uniformly-graded ballast materials gave higher settlement and were also more

vulnerable to breakage than well-graded ballast" (Indraratna et al. 2004; Indraratna and Salim, 2005). A broader gradation than the standard Australian gradation was even recommended by Indraratna and Salim (2005) to give considerably lower settlement without significantly affecting the drainage.

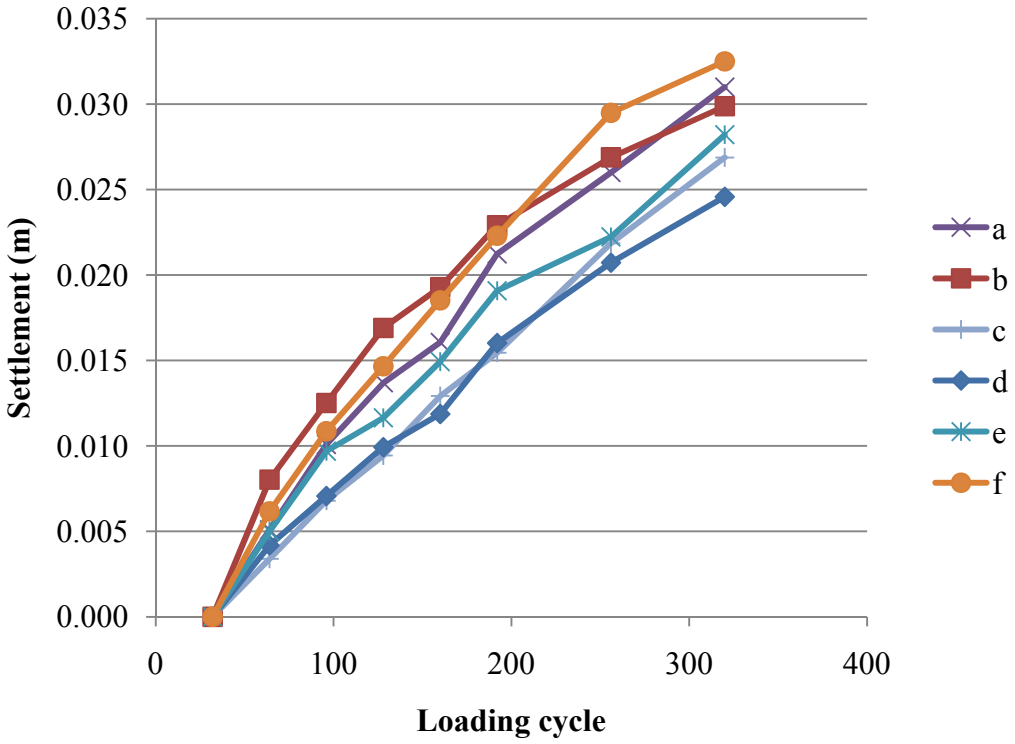

Figure 5.6 DEM Ballast Settlement Predictions for Different Characteristic Gradation Curves

AREMA No. 4, AREMA No. 3, and Queensland gradations currently in use happen to be similar to the characteristic gradation curve "f" (see Figures 5.2 and 5.3). Likewise, AREMA No. 24 gradation currently in use closely resembles the characteristic gradation curve "e" (see Figures 5.2 and 5.3). Therefore, the settlement performances of these

gradations can be also deduced from the DEM simulation findings highlighted in Figure 5.6. Accordingly, AREMA No. 24 gradation is expected to yield the least amount of settlement. Having said that, it is also possible to further engineer AREMA ballast gradation specifications based on such DEM simulation results in an effort to possibly improve the structural support and resistance to settlement by shifting the gradations towards the characteristic gradation curve "d" (see Figure 5.3).

5.6 Summary

This chapter investigated the effect of gradation on ballast settlement using the validated image aided particle shape generation DEM method and the "Ballast DEM Model". Mechanical behavior of ballast layers with different aggregate gradations, including those of AREMA gradations currently in use, was simulated using a full-scale track DEM model. Following the concept of 0.45-power maximum density gradation charts, "characteristic gradation curves" were generated for different minimum aggregate sizes. The AREMA No. 3, No. 4 and No. 24 gradations fall into the categories of some of these "characteristic gradation curves." An investigation on the air void contents of ballast characteristic gradation curves revealed that more uniformly gradated aggregate assemblies generally had larger air voids but higher tendencies to produce permanent deformation under repeated train loading. Although large voids are desirable for better drainage, having particles as small as 3.6 cm can still maintain large voids for drainage and provide better stability and improved resistance to permanent deformation accumulation, i.e. decreased settlement. In view of the DEM study findings, it was concluded that AREMA No.24 gradation would yield the least amount of settlement

among all the existing gradations. According to the DEM methodology, there is also room to further engineer current specifications, including AREMA No. 24 gradation, by optimizing the ballast aggregate sizes for a minimum allowable particle size of 3.6 cm. This would accommodate large enough air voids for drainage and also minimize the overall settlement potential of the ballast layer.

6. AGGREGATE SHAPE EFFECTS INFLUENCING BALLAST BEHAVIOR

In the previous chapter, DEM approach is used to investigate the gradation effect on ballast performance. It is concluded that AREMA No.24 gradation provides the best settlement resistance among all existing mainline ballast gradations. In the current AREMA ballast specifications, beside aggregate size distribution, there is also aggregate shape requirement. Angular and cubical ballast aggregates with crushed faces are preferred. Using digital image technology, aggregate shape properties such as angularity and surface texture can be better quantified. With the image aided particle shape generation DEM method and using the "Ballast DEM Model", aggregate shape effects on ballast performances can thus be quantified and better understood.

In this chapter, the effect of aggregate shape properties including angularity and surface texture on aggregate strength will be studied first. Then, the effects of angularity and surface texture on ballast settlement and lateral stability are investigated by conducting half track DEM simulations. In the end, performance of a textured tie, as one of the means to improve track lateral stability, is evaluated in DEM by tie lateral pullout simulations.

6.1 Preliminary Study of Aggregate Shape Effects on Assembly Strength

To investigate the effect of aggregate angularity and surface texture, direct shear box DEM simulations were performed. Two AI values: 570 and 390 (corresponding to aggregate shapes of Library 2 and 4, respectively) are chosen to represent in DEM the

cases of angular and rounded aggregate shapes. Two surface friction angles: 35 and 15 degrees are chosen to identify the rough and smooth textured aggregates, respectively. Four different samples were generated with the following combinations: angular and rough, angular and smooth, rounded and rough, and rounded and smooth. Accordingly, aggregate shape library 2 with surface friction angles of 35^o and 15^o and aggregate shape library 4 with surface friction angles of 35^o and 15^o were used in the DEM simulations. Only aggregates with F&E Ratio of 1:1 were used because flat and elongated particles can break in actual direct shear box test while elements used in this research are unbreakable. To avoid the influence of the particle size distribution, elements were generated with more or less uniform sizes from 4.75 to 9.5 mm. A square box with 100 mm width and 30 mm depth was utilized in DEM simulation.

For performing the DEM simulations, normal and shear contact stiffness values were set to Kn = 30 kN/m and Ks = 10 kN/m. All samples were compacted at approximately the same void ratios (ranging from 0.5 to 0.6 corresponding to the air voids of 33% to 38%). Samples were prepared in such an accelerated way that aggregates were preset to be absolutely smooth (surface friction angle θ equals to zero) followed by changing gravity force from 9.8 m/s^2 to 50 m/s^2 for a certain amount of time until it reaches the required void ratio. After the system equilibrium was reached, the aggregate surface friction and the gravity constant were set back to the original values. To make sure the system reaches equilibrium at different normal force levels before shearing, the sum of reaction forces acting on the vertical loading plate was also tracked. Only when the system reached equilibrium at different normal force levels before shearing, i.e., the sum of reaction forces became equal to the applied normal force, was the constant

displacement rate of the shear box bottom plate initiated. The shear displacement was applied at a constant speed of 0.15 mm/s. Normal forces of 2000N, 4000N, and 6000N, corresponding stresses of 200kPa, 400kPa, and 600kPa respectively, were applied.

Figure 6.1 shows the maximum shear reaction forces predicted by DEM under the applied normal forces of 2000N, 4000N, and 6000N. As the applied normal force increased, the shear force also increased primarily influenced by the shape effects of aggregate angularity and surface texture. The highest shearing friction angle (from slopes of Mohr-Coulomb envelopes in Figure 6.1) was about 29 degrees obtained from the granular assembly with the highest surface friction angle of 35 degrees and AI of 570, angular and rough in Figure 6.1. When aggregate surfaces are smooth (15-degree surface friction angle in Figure 6.1), the shear strength decreases quite drastically. Yet, a rough-surfaced rounded particle had shear strength higher than that of a smooth-surfaced angular particle (see Figure 6.1).

To further visualize the effects of aggregate angularity and surface texture on mobilizing the shear strength, Figure 6.2 shows the contact force vector plots obtained from the four aggregate samples tested under an applied normal force of 6000N. All contact forces are shown for the same time step when the first peak forces were recorded in the shear box DEM simulations. The maximum resultant shear forces generated in the horizontal direction are also indicated by "Rx" in Figures 6.2a-d to clearly indicate similar trends seen in Figure 6.1. From Figures 6.2a and b, aggregate samples having rough surfaces somewhat indicate a clear, narrow contact force band compared to the relatively wider and scattered contact force bands observed for the samples with smooth aggregate surfaces, as shown in Figures 6.2c and 6.2d. This can be interpreted as the

effect of surface texture; as the aggregate surface gets rougher, the more localized and obvious the shear plane becomes. Whereas, comparing Figures 6.2a and 6.2c of the angular aggregates with those of the rounded ones in Figures 6.2b and 6.2d, the contact force bands turn from a straight single line orientation in the direction of "shear force path" into a bilinear type localized failure zones for the rounded aggregates. The fact that rounded gravel particles have less aggregate interlock compared to crushed angular aggregate to transfer shear force can be explained by the bilinear contact force paths for the rolling and climbing up of the rounded particles.

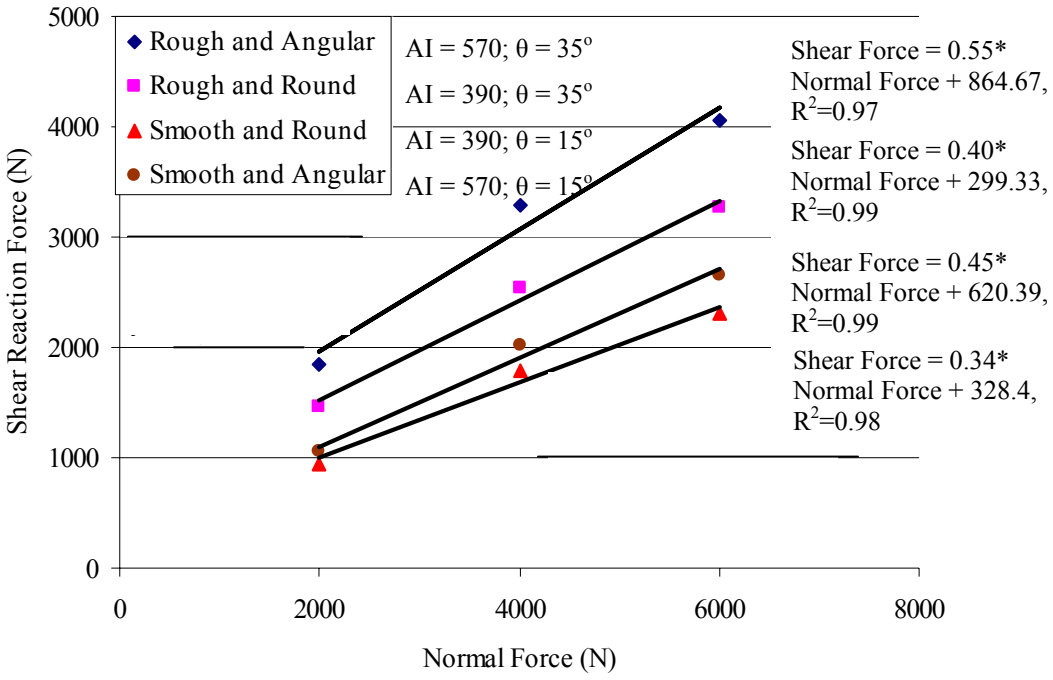

Figure 6.1 Shear Strength DEM Predictions for Round and Angular Aggregates Having Smooth to Rough Surface Texture

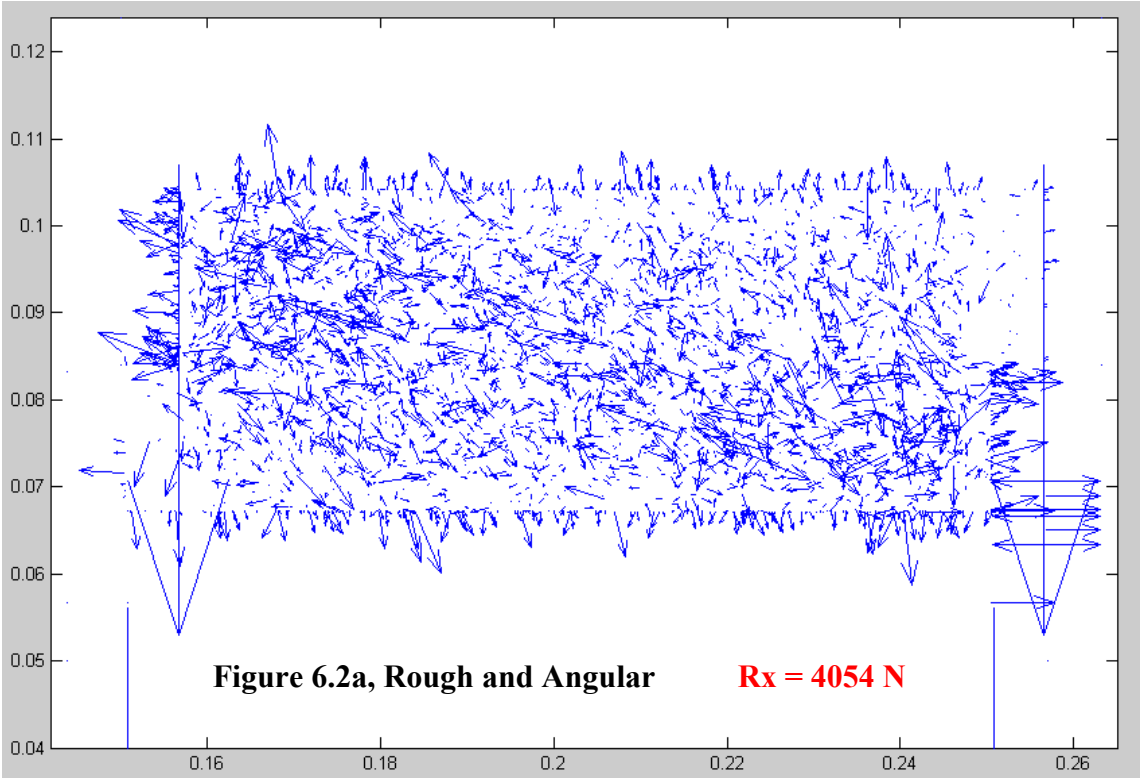

Figure 6.2a, Rough and Angular **Rx = 4054 N**

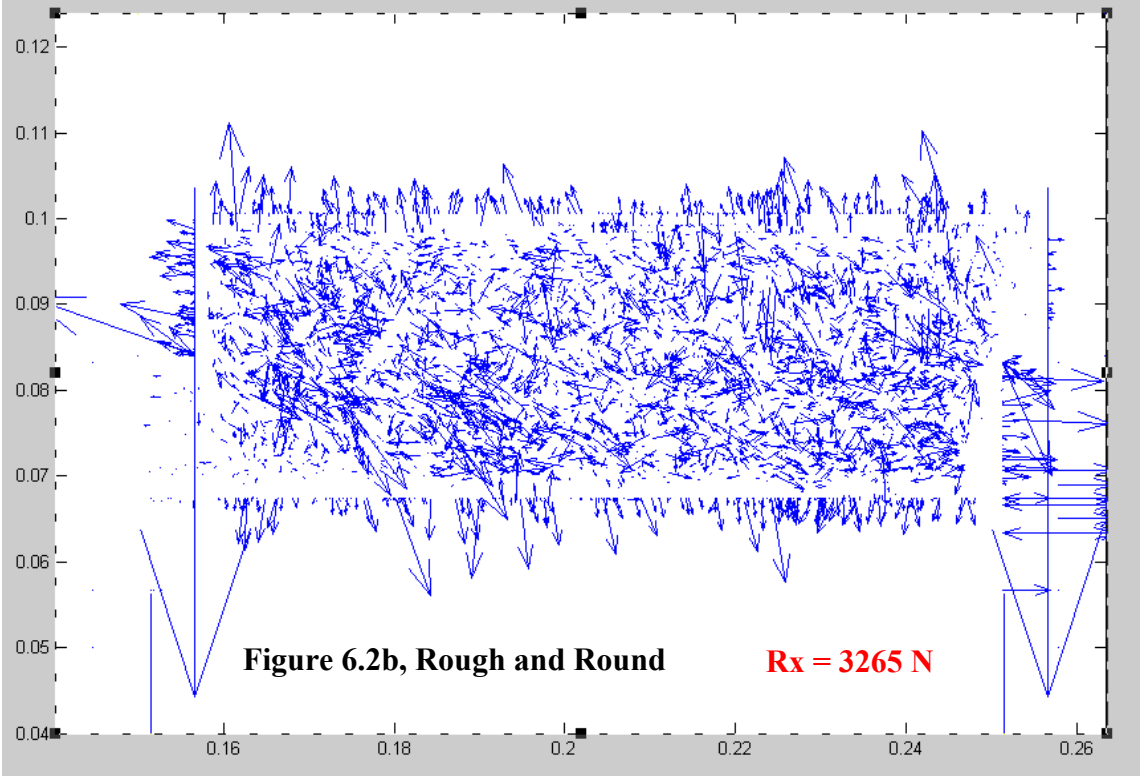

Figure 6.2b, Rough and Round **Rx = 3265 N**

Figure 6.2 Contact Forces Predicted in Direct Shear Box DEM Simulations (Normal Force = 800N)

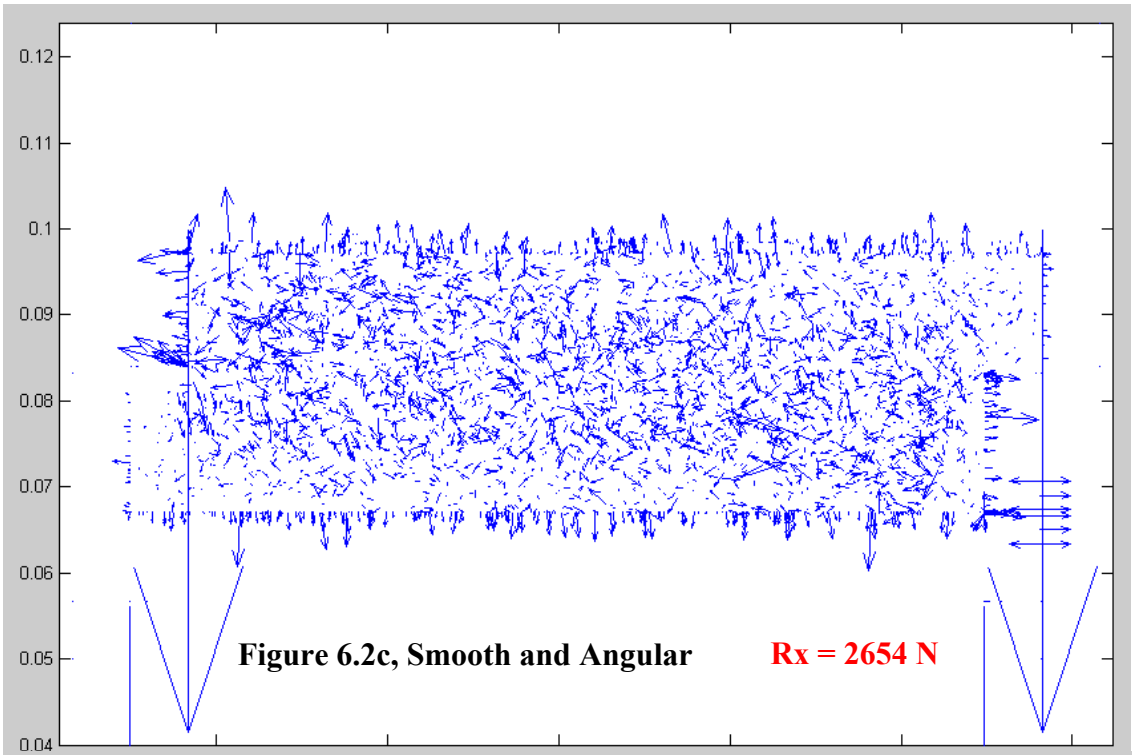

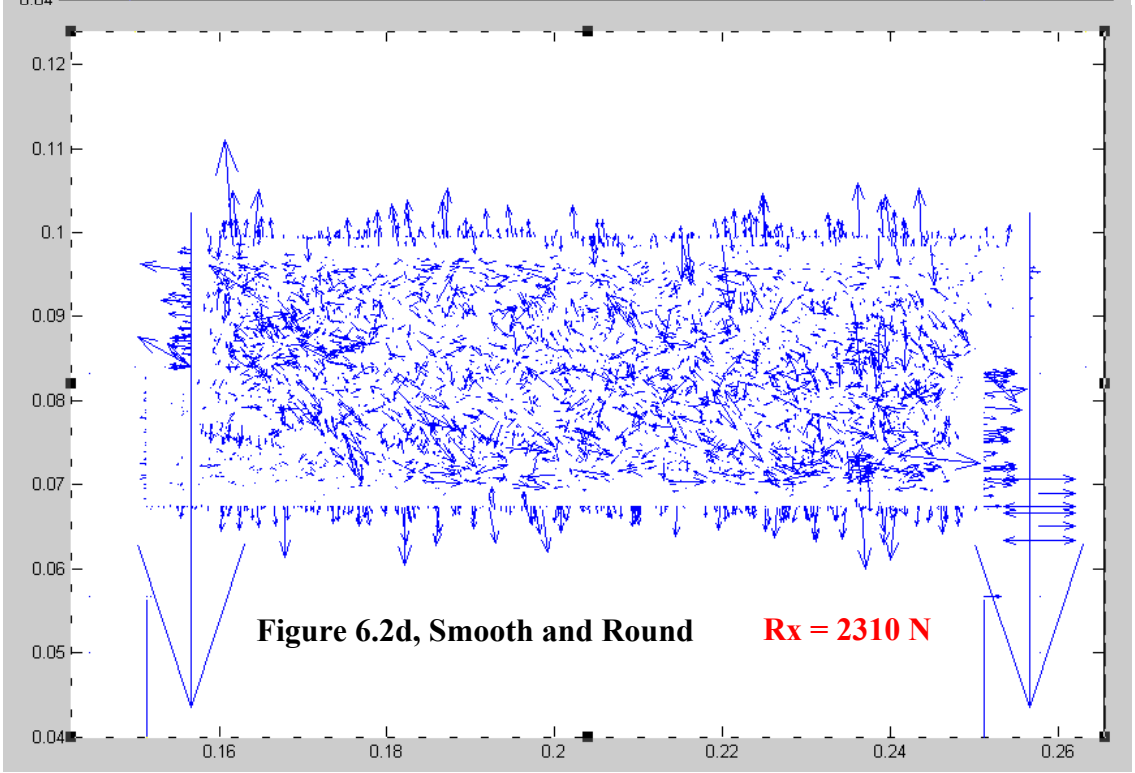

Figure 6.2 (cont.) Contact Forces Predicted in Direct Shear Box DEM Simulations (Normal Force = 800N)

Table 6.1 lists typical railroad ballast shape properties collected from major Northern American Railroads operating in the US. It can be seen from Table 6.1 that all aggregate shapes fall into the AI range from shape library 2 (AI=570) to library 4 (AI=391).

Table 6.1 Common Ballast Aggregate Shape Properties Collected from Railroad Industry in the US

Aggregate Source	Angularity Index *	Flat & Elongated Ratio *	Surface Texture Index *
BNSF(granite)	550	1.3	2.1
BNSF(limestone)	563	1.4	2
BNSF(mix of crushed and uncrushed gravel)	391	1.3	1.1
TTCI(granite)	547	1.2	2.2
TTCI (used granite)	521	1.2	1.9
CSX (granite)	441	2.1	2.3
CSX (dolomite)	451	2.2	1.8
UP(granite)	571	4.8	2.4
UP(limestone)	509	3.6	2.8
NS (limestone)	472	1.9	1.5

* AI and ST indices obtained from UIAIA

All F&E ratio values are between 1:1 and 1:3, i.e. cubical particles. Surface texture index ranges from 1.1 to 2.8. Among the limited sources of ballast aggregates evaluated using UIAIA in this study, BNSF granite sample may have more favourable shape properties since the majority of the aggregate particles are cubical and angular with relatively rough surfaces (see Table 6.1).

6.2 Aggregate Shape Effects on Ballast Settlement

Ballast settlement usually leads to rough track and uneven ride caused by excessive dynamic loading and other track substructure problems. Proper selection of ballast aggregate type, gradation, angularity, and surface texture properties and proper construction and compaction in the field primarily influence ballast layer recoverable (elastic) and permanent (inelastic) deformation trends under repeated train loading. It was clearly shown in Chapter 5 that gradation has a significant impact on ballast settlement performance. Recent laboratory and field research studies have shown that frequency of loading or load pulse duration as a result of trafficking speed might also have a significant impact on the increased rate of settlement of unbound aggregate layers (Kim and Tutumluer, 2006). As for aggregate shape, AREMA specifications require ballast aggregate to be cubical with crushed faces which would ideally correspond to shape library 1. It is believed to be the best aggregate, such as crushed stone, with high strength, superior load distribution and ballast performance. Aggregate shape library 3 represents sub-angular to round particles which often correspond to crushed or uncrushed gravel type of aggregate. To study ballast deformation trends for the different extreme conditions of aggregate shape properties, aggregate shape libraries 1 and 3 were chosen

in this section as the representative aggregate sources to construct and subject the ballast layer in DEM simulations to repeated loading.

AREMA No. 24 ballast gradation was used for all ballast aggregate samples with different shapes. It was assumed that ballast aggregates were non-breakable and no abrasion was tolerated to ensure that all ballast samples were of the same solid shape throughout the DEM simulation process. This way, any difference in simulation results between different ballast samples would be only attributed to the aggregate shape effects. In this section, the previously calibrated DEM model parameters for the granite type of ballast aggregates (Kn = 20 MN/m; Ks =10 MN/m; $\theta = 31^{o}$) were also used.

Loading Magnitude and Frequency

Dynamic loading on top of a tie is determined by un-sprung excitation and train speed. Assuming that there is no excitation coming from the train itself and the track is perfectly smooth; the load magnitude and duration (or frequency) on top of the tie is determined by the train weight and speed. Exact load magnitude and duration underneath the rail, i.e., on top of the tie, can be obtained from the dynamic track model derived in Chapter 4. However, in this section, half sine functions with different magnitudes and periods (frequencies) are used as the loading profile since the primary focus was to study the loading frequency effect on ballast settlement. It is also reasonable since any continuous function can be decomposed into series of trigonometric functions. Figure 6.3 shows the typical loading profile on top of a tie representing a 160,000-kg train car moving on the track. Since the load pulse shown in Figure 6.3 is of a half-sine wave shape with the

second half portion considered for 0.5-second rest period, it is considered as a 1 Hz load pulse in this study.

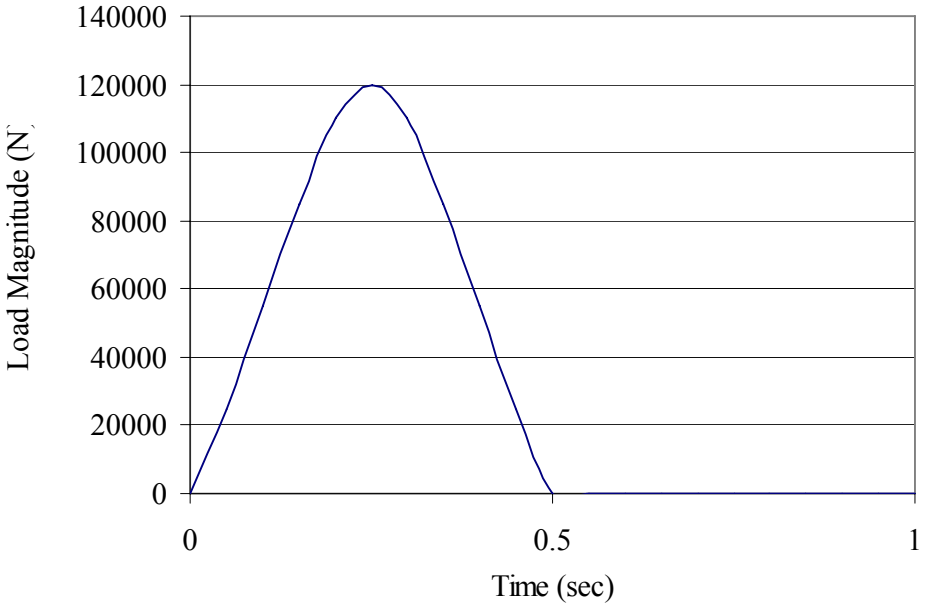

Figure 6.3 Single Tie Load Pulse of a 160-Mg Car Applying Loading at 1-Hz Frequency

DEM Simulation Results and Analyses

After the half ballast section simulation was developed, a half tie was generated and placed on top of the ballast layer followed by the applications of individual dynamic loading profiles and the load pulse shapes shown in Figure 6.3. Different combinations of DEM simulations were performed to consider a total of one load magnitude (120 kN), three load frequencies (1 Hz, 5 Hz, and 10 Hz), and two ballast aggregate shapes, i.e., libraries 1, and 3. All ballast samples including both the angular and rounded particles were compacted to the same air void content of 38%. Ballast settlement, i.e., permanent

deformation or rut depth, was recorded with the number of load cycles for all the DEM simulations. Each repeated loading test was performed up to 100 cycles but not up to commonly tested three log cycles due to intense computational needs of DEM simulations.

For the ballast layer with cubical and angular shaped aggregates (shape library 1), Figure 6.4 shows settlement under the moving train load graphed with load cycles investigated at all three frequencies for aggregate shape 1. It can be clearly seen that train speed has a significant impact on ballast settlement as obtained from these DEM simulations. The faster the train goes (higher loading frequency or shorter pulse durations) the higher are the permanent deformations accumulated under the same load magnitude for the same ballast aggregate material.

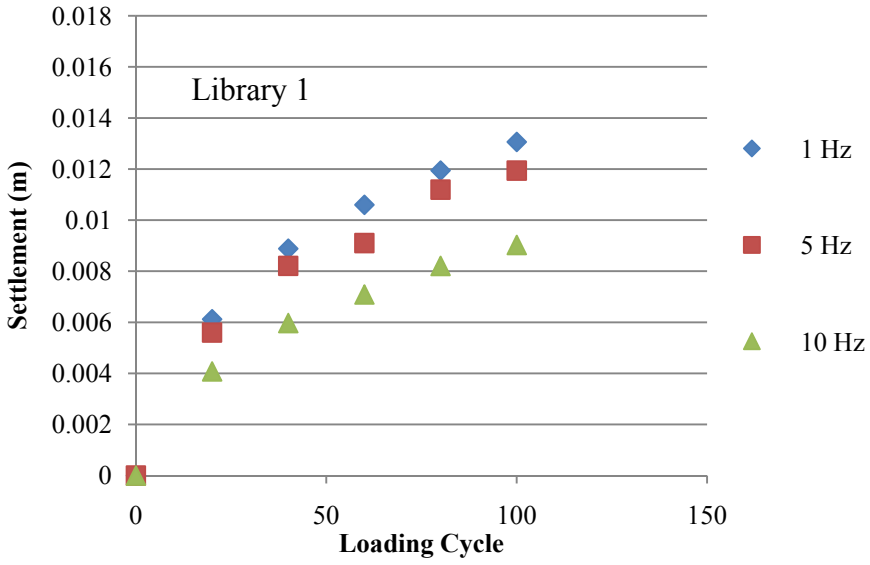

Figure 6.4 Loading Frequency Effect on Ballast Settlement

Kim and Tutumluer (2006) reported similar findings on unbound aggregate permanent deformation trends from both laboratory repeated load triaxial testing of compacted aggregate specimens and full-scale field testing of thick airport granular layers. It is indeed encouraging to see the similar trends obtained here from the DEM simulations.

Figure 6.5 shows the aggregate angularity effect on ballast settlement. It is shown that a ballast layer with angular aggregate particles (library 1) yields less settlement than the ballast with rounded aggregate particles (library 3). This result also implies that at the same air voids, ballast with angular aggregate particles has higher settlement resistance than ballast with rounded aggregate particles.

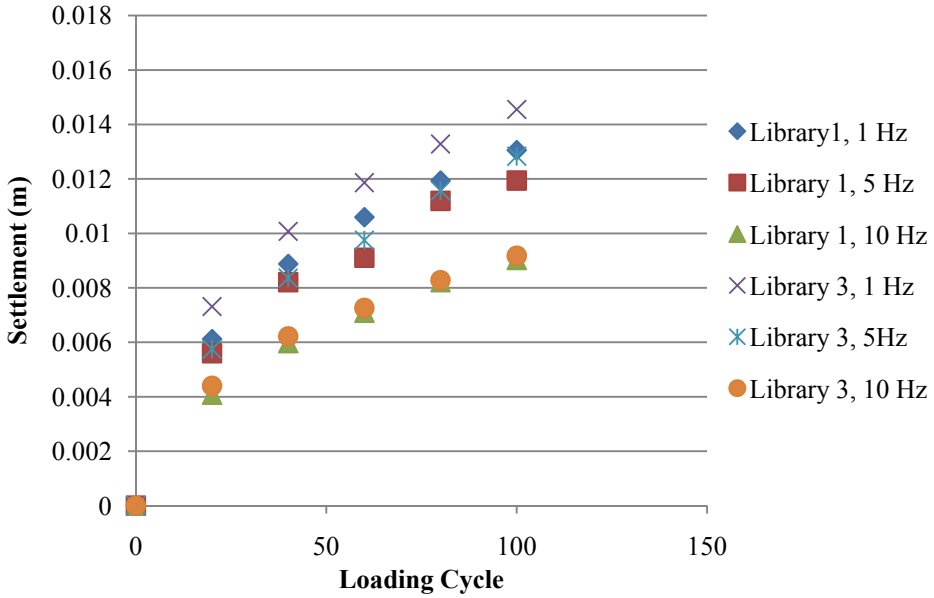

Figure 6.5 Particle Angularity Effect on Ballast Settlement

Although DEM simulations have yielded encouraging results, the computing time using existing stiffness values (Kn = 20 MN/m, Ks = 10 MN/m) has been very long. Accordingly, in the rest of the simulations the contact stiffness values are reduced to Kn

= 2 MN/m and Ks = 1 MN/m in order to save computing time of the remaining simulations discussed in this chapter.

Additional DEM simulations were performed for different combinations to consider again one load magnitude (120 kN), three load frequencies (1 Hz, 5 Hz, and 10 Hz), and two ballast aggregate shapes, this time using libraries 1 and 8 with adjusted DEM model parameters (Kn = 2 MN/m, Ks= 1 MN/m, and $\theta = 31^{o}$). Shape library 8 represents a flat and elongated type of aggregate particle which is less favorable in railroad engineering practice since it is low load bearing and has the tendency to more easily break and degrade. Each repeated loading test was performed again up to 100 cycles.

For the ballast layer with cubical and angular shaped aggregates (shape library 1), Figure 6.6 shows settlement under the moving train load graphed with load cycles investigated at all three train speeds (frequencies). It can be clearly seen that train speed, as previously proven, still shows a significant impact on ballast settlement. The faster the train goes (higher loading frequency or shorter pulse durations) the higher are the permanent deformations accumulated under the same load magnitude for the same ballast aggregate material. Note that shorter the load pulse durations are, the less is the effect of the sustained load for the case of 1 load application per second simulated in this study.

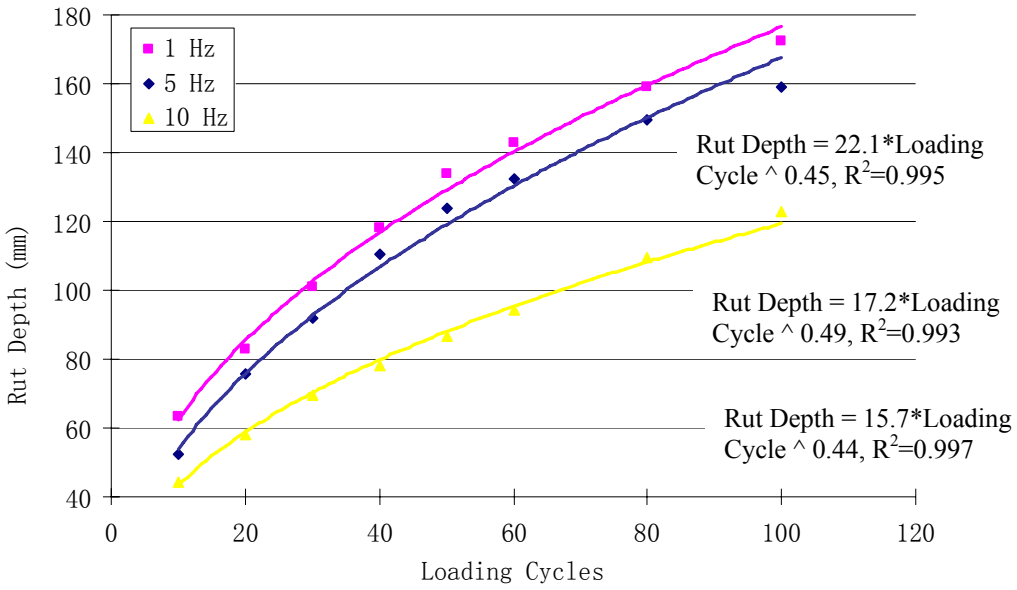

Figure 6.6 Settlement Predictions of Ballast with Aggregate Shape Library 1 (Cubical – Angular) at Three Different Loading Frequencies

Figure 6.7 indicates for the library 1 aggregate shape permanent deformations produced by a static loading (zero frequency) and the same magnitude dynamic loads applied at different frequencies. It can be observed that the settlement produced by the static load is lower than the permanent deformation due the 1-Hz dynamic loading. As the loading frequency increases, the settlement is estimated to peak at a frequency between 1 and 5-Hz loadings, then, it decreases to a rut accumulation less than the starting value due to the static loading. Therefore, there might exist a frequency analogous to a natural frequency, possibly of the track structure simulated here, which could produce the maximum settlement.

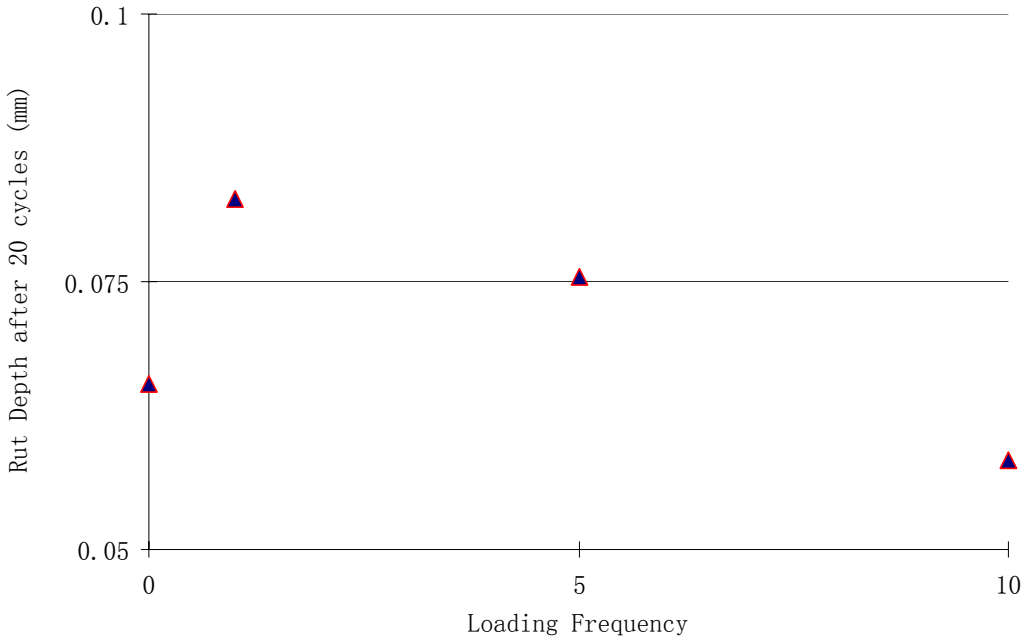

Figure 6.7 A Conceptual Line of Permanent Deformation Produced by the Static Load and the Same Magnitude Dynamic Loads Applied at Different Frequencies

In Figure 6.8, comparison is made between the performances of the ballast layers with the cubical-angular shaped library 1 aggregate and the elongated and rounded shaped library 8 aggregate. Because the elongated aggregate yields smaller settlement than the cubical one should not imply that the ballast layer with the flat and elongated aggregate particles can outperform the ballast with the cubical-angular library 1 aggregate. Note that in the DEM simulations the flat and elongated particles were not allowed to break although in reality they tend to easily break and degrade under heavy wheel loading.

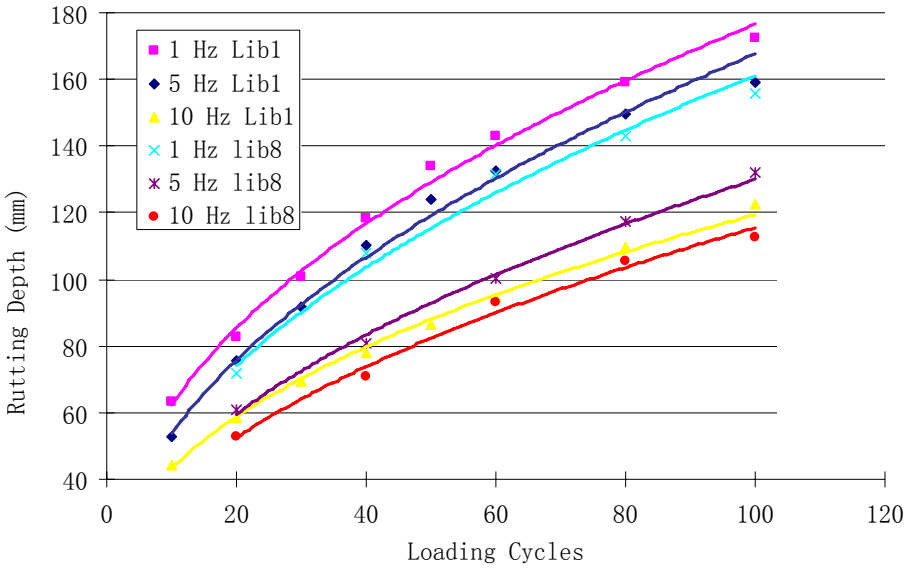

Figure 6.8 Comparisons of Ballast Settlement Predictions between Aggregate Shape Library 1 (Cubical – Angular) and Shape Library 8 (Elongated – Rounded) at Three Loading Frequencies

Figure 6.9 shows the recorded residual forces acting on the transverse vertical plane for the library 1 (angular) aggregate shape. The residual force decreases with the increase of loading cycle which conforms reasonably well to the previous research findings (Norman and Selig, 1983). The relatively fast trend of the decrease in residual forces, however, suggests that the confinement effect from the rigid transverse vertical plane needs to be adjusted by possibly including more ties in the train moving direction in future "half-track" DEM simulations.

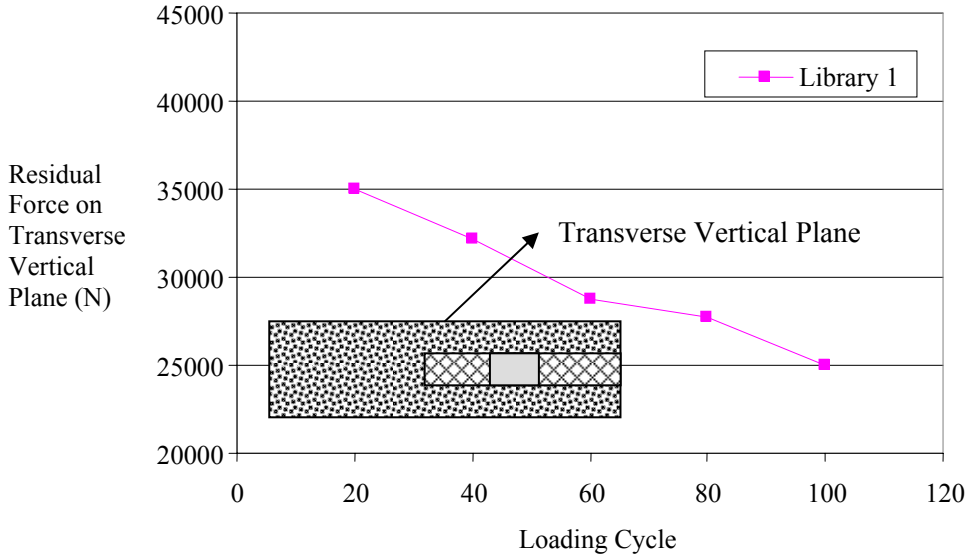

Figure 6.9 Residual Forces Crated on the Transverse Vertical Plane (The Middle Plane between Two Ties)

6.3 Aggregate Shape Effect on Ballast Lateral Stability

Track lateral stability is a key factor for railway safety. Derailment disasters due to track buckle are typical results of losing track lateral stability. Buckle is a phenomenon normally associated with large axial rail forces. It usually takes place in the hot season when increasing temperature induces large thermal stresses in the rail. Analysis of track lateral stability or track buckle resistance is usually performed by assuming a sinusoidal buckled shape with a magnitude of "A" as shown in Figure 6.10 (Esveld 2001). Then, the buckled rail can be represented as a side supported Euler beam with fixed displacement at the ends.

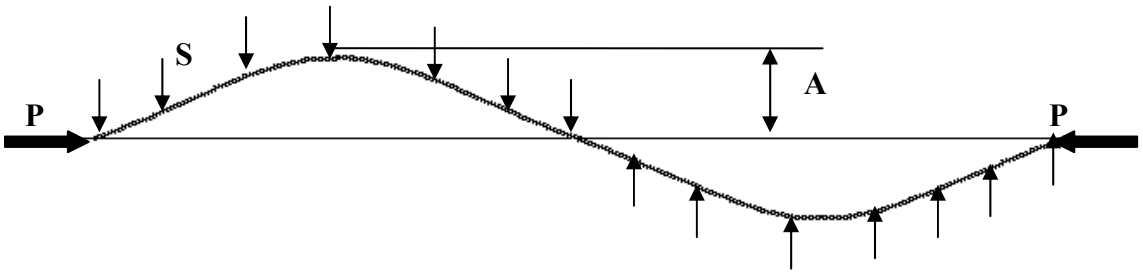

Figure 6.10 Rail Shape and Forces Acting during Rail Buckle

"S" is the tie-ballast lateral resistance which is constant along the rail. It can be derived from the reaction force at the rail ends, i.e., buckle resistance force is in the form of:

$$P = \frac{4\pi^2 EI}{L^2} + \frac{SL^2}{A\pi^3} \tag{6.1}$$

where P is the buckle resistance force; EI is the moment of inertia of the rail; L is the rail length; S is the tie-ballast lateral resistance; and A is the magnitude of the sinusoidal rail wave shape.

Equation 6.1 implies that rail buckle resistance mainly consists of two parts: resistance from the rail lateral rigidity (Euler buckling load) and the resistance from tie-ballast lateral resistance. When the rail material and the cross-section geometry are set, the rail length and the tie ballast lateral resistance becomes of great importance to the track lateral stability.

Track Lateral Stability Supplied by Ballast

There are many factors which may influence the ballast lateral resistance. Aggregate shape and maintenance activities are among the most important factors. Under repeated wheel loading, railroad ballast is gradually consolidated gaining strength from aggregate interlocking. Meanwhile, the ballast layer accumulates permanent deformation after certain amount of traffic which often causes rough track profile. Maintenance activities such as tamping aims to raise the ballast layer and correct the track profile. During tamping, tie is raised followed by inserting the tamping arms; squeezing and vibrating the ballast. Usually railroad profile can be corrected by one to several rounds of tamping. However, tamping dramatically decreases the ballast strength and stability by disturbing the consolidated ballast. Tie lateral pull out tests show that ballast could lose up to 60% of its original lateral resistance to tie right after tamping.

In this section, tie pull out tests are simulated in DEM before and after tamping using 11 half-scale railroad track sections each containing one of the previously defined 11 ballast aggregate shape libraries.

DEM Sample Preparation

In this section, half ballast sample was used due to the symmetry of the railroad track to the longitudinal middle plane. In the longitudinal direction, a 508-mm segment was chosen which represents the typical tie spacing. A half section of a tie with 178 mm X 203 mm X 2591 mm dimension was used. The ballast gradation was No.4 and was chosen to be at 457 mm considering a typical tamping depth of 305 mm. Model

parameters including: Kn = 2 MN/m; Ks = 1MN/m; and θ = 35^{o} were used in this section. The simulation procedure also shown in Figure 6.11 is as follows:

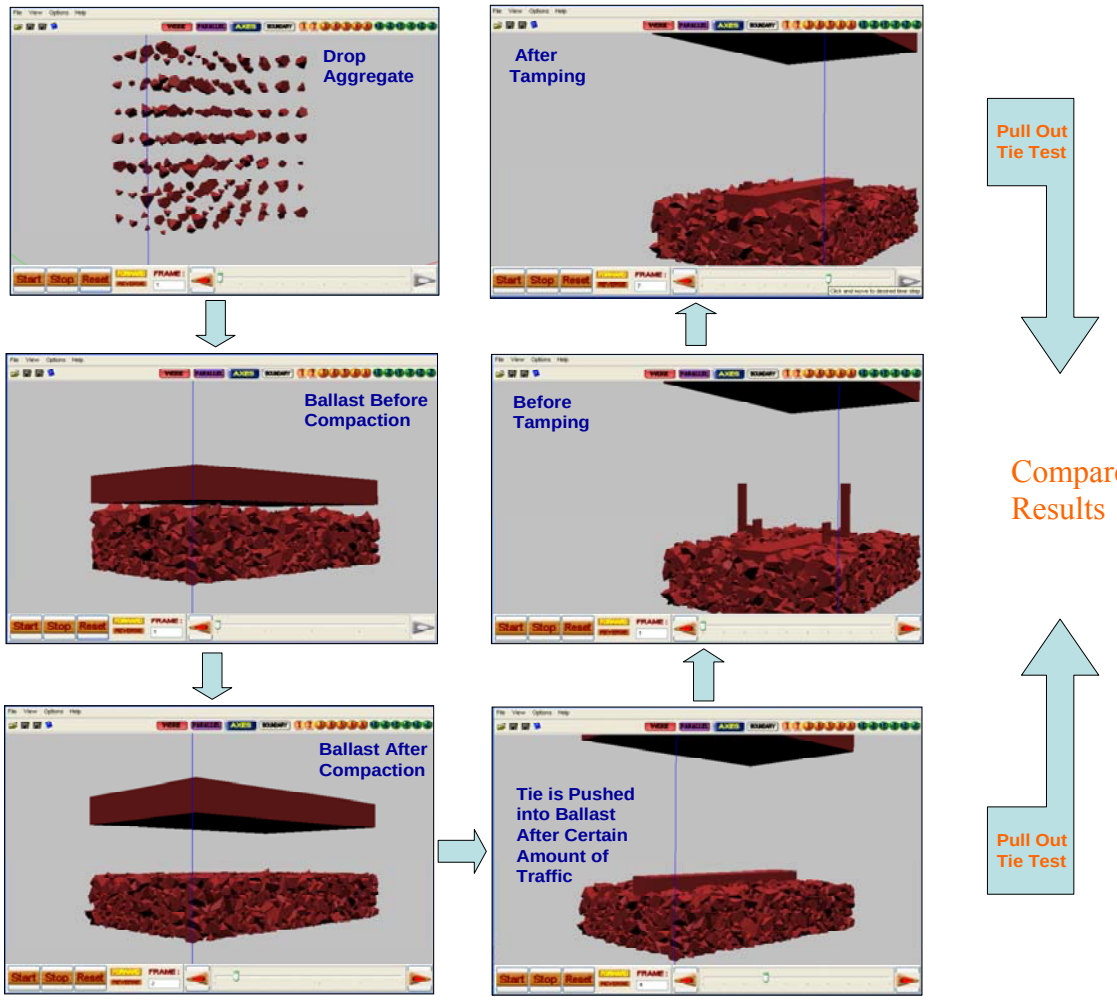

Figure 6.11 Tie Pull Out Test Procedure

1. Generate a layer of aggregates, typically 76 mm to 127 mm, in the gradation of No.4 from one library. Let aggregate fall down into a space described before and generate the second layer until the first layer stabilizes. Repeat the process until enough ballast depth is reached. Assign material and environment constants such

as: density, surface friction angle, gravity and etc. Totally 11 ballast layers were generated using aggregates from 11 libraries.

2. Compact each ballast sample by first decreasing aggregate surface friction angle to 0 i.e. aggregate surface is absolutely smooth and then generating a rigid block and pressing down until no more vertical displacement is observed.
3. In the field, tie will be pushed into the ballast layer and stabilized when the traffic accumulates to a certain point. Meanwhile the ballast portion under tie gains maximum interlock strength. In the laboratory, it is normally checked by monitoring the residual stress in the ballast layer. It is assumed in this study that the ballast and tie stabilize when the residual stress reaches maximum. Since this process is very time consuming, an alternative method is utilized. After placing the tie on the top of the ballast layer, the gravity constant is increased to 50 m/s^2 and the aggregate surface is kept smooth from step 2. The tie-ballast structure "Equilibrium Status" is checked by using residual stress method (Steward et al, 1985). The aggregate surface friction angle is then changed back to its normal value, in this study 35 degrees. A consolidated tie-ballast sample is thus prepared.
4. Raise the tie up and insert tamping arms into the ballast layer at the position of the rail-tie crossing squeezing and vibrate at a frequency of 35 Hz for 2 seconds.
5. Place the tie back on the top of the tamped ballast layer.
6. Apply 3000 N vertical force on the tie followed by 25mm lateral displacement to the tie for the same sample but one in step 3 and one in step 5. Record the mobilized lateral resistance forces for all 11 samples.

Test Results and Conclusions

Tie lateral resistance forces before and after tamping for all 11 different shaped ballast aggregates are shown in Figure 6.12. The ballast samples with aggregates of higher AI values show significantly higher lateral resistance to the tie than ballast samples with lower AI value both before and after tamping. Tamping has a large impact on the shear resistance especially for aggregates with high angularity index. The lateral stability decreases as much as 40% (Bar No.1 in Figure 6.12) for aggregate with AI of 670. However, for aggregates with low AI (round aggregates) tamping has a relatively low impact on the lateral stability (Bar No.4 in Figure 6.12), which implies that round aggregates have weak interlocks. For ballast with flat & elongated aggregates, it is worth noticing that the same trend still applies but in a less significant manner (Bar No. 5-11 in Figure 6.12). Some flat and elongated aggregates are even not affected by tamping. It however does not suggest that flat & elongated aggregates are better than cubical aggregates. When flat & elongated aggregates are loaded they are very susceptible to breaking and will degrade rapidly, which could not be shown in this study because discrete elements were non-breakable.

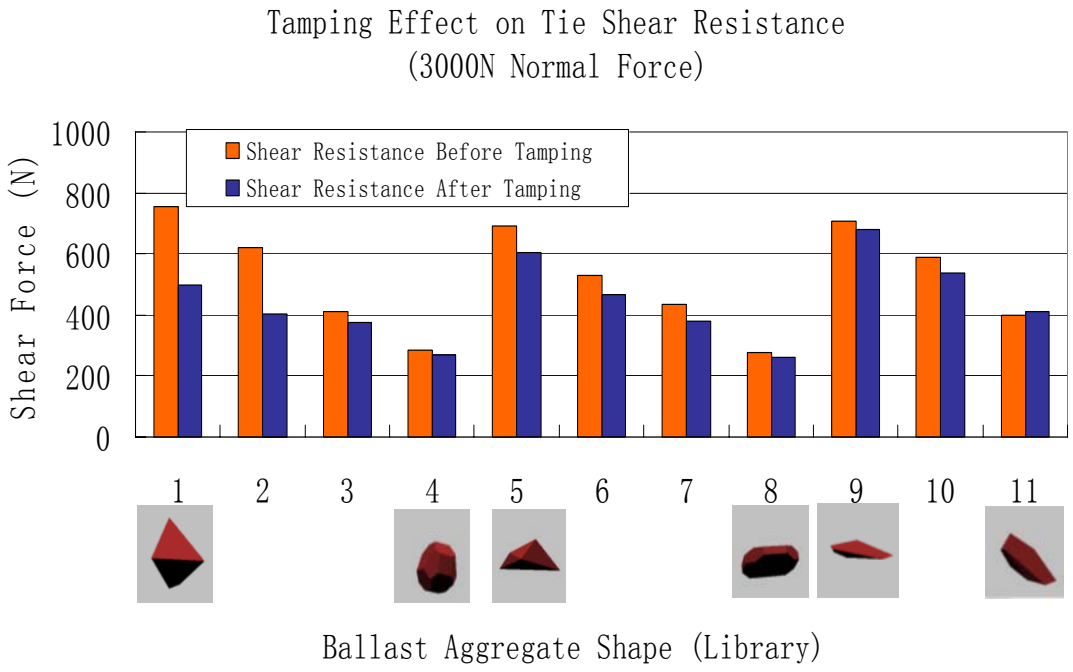

Figure 6.12 Tie Lateral Resistance Results from Pull out tests for 11 Aggregate Shapes

Textured Tie Simulation

To improve track lateral stability, manufactured crossties, plastic or other recycled materials usually textured on the surfaces, are often considered as part of field research studies to investigate added shear friction on the crosstie surface. DEM tie pull out simulations are conducted in this section for both smooth and textured crossties to evaluate the effects of the crosstie texture. Figure 6.13 shows a 3D drawing of the checkerboard patterned surface textured crosstie used in the DEM simulations.

The same half ballast section was generated for analysis since the track structure is symmetrical. Angular aggregates with rough surfaces (AI=630, F&E ratio=1 to 1, and θ=35 degrees) were used representing clean and high quality crushed stone ballast conditions. The two textured and smooth surfaced crossties (see Figure 6.13) were then

generated in the BLOKS3D library as individual block elements. Only track structures before any maintenance activities were considered. During the pull-out process, a vertical force of 5000 N was applied on the top of the crosstie followed by a lateral force pushing the tie at a constant speed of 0.01m/s until a total displacement of 0.2 m was reached.

During the tie pull-out tests, the lateral forces resisting the crosstie movement were continuously measured with the maximum force recorded and defined as the tie-ballast lateral resistance. For the smooth non-textured crosstie, a lateral resistance of S=1297N was obtained; while for the textured tie, a much higher resistance of S=3537N was recorded. By substituting these tie-ballast lateral forces (S) into Equation 6.1, with typical rail material, cross section parameters, and rail lengths listed in Table 6.2, different track buckle resistance forces (P) were computed. Comparing the calculated buckle resistance forces (P), it shows that a textured tie can improve the track lateral stability, in this example, by 45% to 88% more when compared the smooth crosstie.

Table 6.2 Improvement in Lateral Stability by Using Textured Crosstie

A (m)	EI (Nm^2)	S (N)	Actual Rail Length (m)	Buckle Resistance Force	Improvement in Lateral stability
0.025	8.00E+06	1297	16	1662042	45%
0.025	8.00E+06	3537	16	2401815	
0.025	8.00E+06	1297	21	1454047	88%
0.025	8.00E+06	3537	21	2728421	

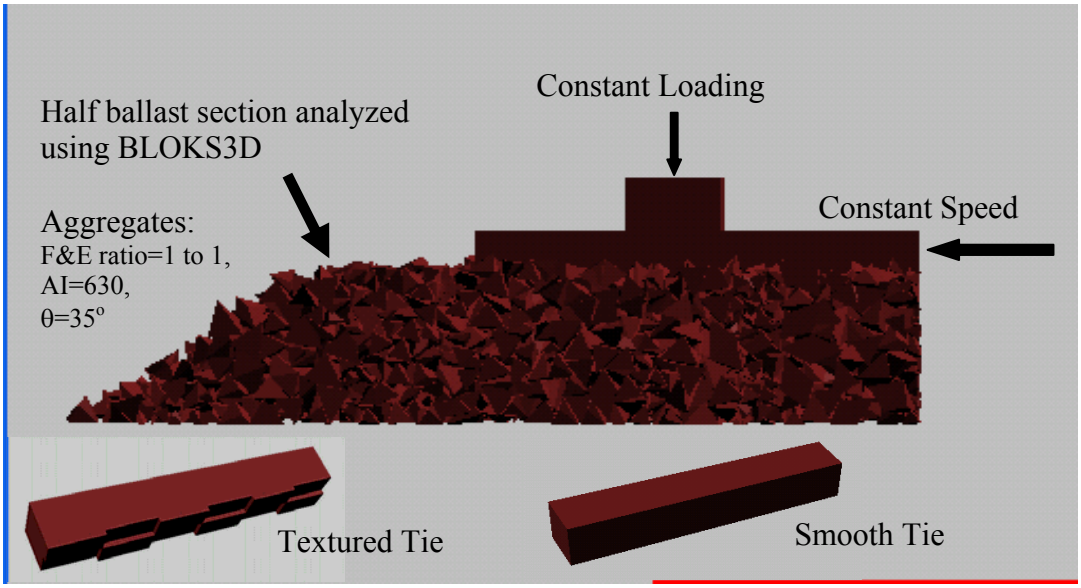

Figure 6.13 Tie Lateral Pull-Out Test Simulations with Smooth (Non-Textured) and Textured Crossties

6.4 Summary

In this chapter, the effect of aggregate angularity and surface texture on aggregate assembly strength is investigated by DEM shear box simulations. Test results show that aggregates with higher angularity (AI) showed higher strength than rounded particles. Surface texture was found to play a predominant role in controlling strength. When assigned very smooth or polished surface texture, even highly angular aggregates, such as crushed stone, indicated quite poor shear strength characteristics. From the plotted contact forces between aggregates, one may conclude that angular particles will form a straight force band within the shear zone and thus supply tougher resistance to shear whereas round particles form two bands due to lack of particle interlock and have weak resistance to shear. Finally, surface texture may even be more important than aggregate

angularity since angular particles with smooth surfaces have lower strength properties than rounded particles with rough surfaces.

Load frequencies or load pulse durations governing the various train speeds and ballast aggregate shape properties, cubical versus elongation and angular versus rounded aggregates, were the two main factors studied in the context of settlement or permanent deformation accumulation trends. From the DEM simulations for up to 100 repeated load applications, it was found that reducing the train speed, such as in the slow orders, (or decreasing the applied loading frequency by increasing the load pulse durations) often resulted in a significant increase in the rut accumulation. However, static loading induced smaller permanent deformations than the 1-Hz loading. Therefore, a critical loading frequency to give the highest deformation could be realized between 1 and 5 Hz loadings.

Effects of ballast aggregate shape was found to influence ballast settlement. The DEM simulations that considered single tie tests resulted in lower ballast settlements for angular aggregate particles. For future ballast settlement simulations, it will be worthwhile to consider a modified ballast box for the half tie and half ballast width railroad track geometry with at least three ties included to properly model longitudinal confinement and movement of ballast aggregate.

Tie lateral resistance forces predicted before and after tamping for all 11 different shaped ballast aggregates showed that ballast samples with aggregates of higher AI values have significantly higher lateral resistance to the tie than ballast samples with lower AI value both before and after tamping. Tamping has a large impact on the shear resistance especially for aggregates with high angularity index. The lateral stability decreases as large as 40% for aggregate with AI of 670. However, for aggregates with

low AI index (round aggregates) tamping has relatively weak impact on the lateral stability, which implies that round aggregate has weak interlock. For ballast with flat & elongated aggregates, it is worth noticing that the same trend still applies but in a less significant manner. Some flat and elongated aggregates are even not affected by tamping. It however does not suggest that flat & elongated aggregates are better than cubical aggregates. When flat & elongated aggregates are loaded, they are very susceptible to breaking and will degrade rapidly. This study has not shown that because discrete elements used were un-breakable.

The benefits of using manufactured crossties with textured surfaces on ballast strength improvement were also investigated using the "Ballast DEM Model". Typical tie lateral pull-out test DEM simulations were undertaken using a checkerboard patterned textured tie. Pullout test simulations successfully proved that the textured crosstie provided more lateral stability for the track than non-textured smooth crosstie to improve track stability and mitigate rail buckle problems in the field. Future research could potentially focus on selection and optimization of ballast aggregate properties and manufactured crosstie texture designs using DEM approach.

7. CONCLUSIONS AND RECOMMENDATIONS

This research has focused on developing a better understanding through an advanced modeling approach for railroad ballast behavior subjected to train loading. Ballast consists of aggregate particles with mostly uniform size distributions and shape properties such as angularity, flatness and elongation, and surface texture. It is necessary to quantify the effects of aggregate morphological characteristics on the railroad ballast performances to better engineer and optimize use of ballast materials. This is to design ballast with desired structural and functional properties by adjusting ballast morphological characteristics such as size and shape properties.

A digital image aided particle shape generation method for Discrete Element Method (DEM) is proposed in this research to study effects of aggregate size and morphological characteristics on ballast performance. “Ballast DEM Model” developed based on this approach is validated by both laboratory and field experiments. Using this model, influence of ballast gradation on ballast settlement potential is investigated first. Aggregate shape effects on ballast strength, settlement, and lateral stability are then studied using this “Ballast DEM Model”. Important findings and recommendations for future research are summarized in the following sections.

7.1 Research Findings

DEM is a time domain iterative solution for problems involving particle dynamic interactions. The research focus of discrete element modeling of railroad ballast mainly considered an imaging based aggregate size and morphology characterization. A unique

approach of creating discrete elements from scanned images of individual aggregate particles was introduced. After validating the approach using laboratory and field experiments, effects of aggregate particle size distribution and shape properties on performances of ballast are investigated. Major findings are highlighted as follows:

1. In Discrete Element Modeling, the controlling model parameter was identified as the surface friction angle (θ). Contact stiffnesses in normal and shear directions, Kn and Ks, were found to have only negligible impact on the DEM simulation results. Proper stiffness values shall be chosen based on the following principles: 1) Normal contact stiffness Kn must be large enough to prevent elements excessively penetrating into each other; 2) contact stiffnesses also need to be as small as possible to minimize the computing time per iteration.
2. By statistically comparing the Mohr-Coulomb strength envelopes of DEM shear box simulations and laboratory test results, it is concluded that the "Ballast DEM Model" can predict railroad ballast deformation behavior reasonably accurately.
3. Simulation results from this validated approach reveal that more uniformly graded aggregate assemblies generally have larger air voids but increased tendencies to produce greater permanent deformation under repeated train loading. Although large voids are desirable for better drainage, having particles as small as 3.6 cm (1.4 in.) can still maintain large voids for drainage and provide better stability and improved resistance to permanent deformation accumulation.
4. In view of the DEM study findings, it is concluded that AREMA No.24 gradation would yield the least amount of settlement among all the existing AREMA

gradations. According to the DEM methodology, there is also room to further engineer current specifications, including AREMA No. 24 gradation, by optimizing the gradation for maintaining drainage and at the same time minimizing the overall settlement potential of the ballast layer.

5. Shear box DEM simulation results for aggregates with different morphological characteristics showed that angular aggregates give higher shear strength than rounded aggregates due to better interlock. Also it was found that aggregates with rough surfaces give higher shear strength properties than aggregates with smooth surfaces. Further, aggregate surface roughness was indicated to be even more dominating than aggregate angularity in terms of its impact on the shear strength.
6. DEM settlement simulation results showed that reducing the train speed, such as in the slow orders (or decreasing the applied loading frequency by increasing the load pulse durations), resulted in a significant increase in the rut accumulation. Also, DEM settlement simulation results for ballast aggregates with different morphological characteristics showed that ballast size aggregate particles with angular shapes have less settlement potential than ballast with less angular aggregate particles.
7. Tie lateral pull out DEM simulation results showed that ballast samples with more angular particles provide significantly higher lateral resistance for the tie than ballast samples with rounded particles both before and after tamping. Tamping has a large impact on the shear resistance especially for aggregates with high angularity index.

8. Using a checkerboard patterned textured tie in the tie lateral pull-out test DEM simulations, it was demonstrated that the textured tie provides more lateral stability for the track than non-textured smooth tie.

7.2 Recommendations for Future Research

The conclusions drawn from this research study on the developed "Ballast DEM Model" findings are just the beginning for an improved understanding of ballast behavior. The recommended future research areas are listed as follows:

1. Additional laboratory and field experiments are needed to further validate the "Ballast DEM Model" by studying effects of aggregate size distributions and morphological characteristics and matching them with DEM predictions for settlement and lateral stability performances.
2. The effects of aggregate size distribution and shape properties on the ballast constructability and compact-ability can be studied. It has been proven that angular particles perform better than rounded particles in terms of both strength and stability. This is, however, based on the fact that all samples were actually compacted to more or less the same air voids. The same air voids condition may not be achieved easily since it is known that angular particles tend to have larger voids than rounded particles under field compaction effort. It is suggested to further investigate the optimum combination of aggregate angularity and compact-ability. To that end, how to optimize aggregate shape properties and the size distribution needs to be focused.

3. New and more advanced DEM capabilities need to be developed to consider more realistic railroad ballast conditions such as particle breakage. It will be also more realistic in the future be able to account for the pore water pressure in the DEM simulation. With such DEM capabilities, ballast fouling can be more comprehensively and realistically investigated.
4. Similarly, new and more advanced DEM capabilities are needed to model bonded or glued aggregate particles and investigate their influence on railroad ballast behavior.
5. DEM is an ideal tool to study the interaction between unbound aggregates and geosynthetics for mechanical stabilization such as the aggregate interlock established when geogrids are used. Geogrids have been widely used in pavement subgrade stabilization and in some applications of railroad ballast reinforcement. DEM can be utilized to 1) study the geogrid opening size or aperture and the corresponding aggregate size and shape properties for providing the best reinforcement through interlock, 2) study the confining mechanism, which will provide insight into layered analysis of the geogrid reinforced railroad track structures.

REFERENCES

AASHTO PROVISIONAL STANDARDS, TP 56-03, "Uncompacted Void Content of Coarse Aggregate (As Influenced by Particle Shape, Surface Texture, and Grading)," Washington, D.C., American Association of State Highway and Transportation Officials, 2003.

Achenbach, J.D. and Sun, C.T., "Moving Load on A Flexible Supported Timoshenko Beam," International Journal of Solids and Structures, Vol. 1, pp. 353-370, 1965.

Alameddin, A.N. and S.J. Luzik, "Coal Dust Explosions in the Cement Industry," Industrial Dust Explosions, ASTM STP 958, Philadelphia, PA, pp. 217-233, 1987.

Allen, J., "The Effect of Non-constant lateral Pressures of the Resilient Response of Granular Materials," PhD report, University of Illinois at Urbana Champaign, 1973.

Ammann, O. and C. V. Gruenewaldt, "Tests of the Effect of Axial Forces in the track," Organ fur die Fortschritte des Eisenbahnwesens, Heft 6, 1933.

Andersson, C. and Oscarsson, J., "Dynamic Train/Track Interaction Including State-Dependent Track Properties and Flexible Vehicle Components," Vehicle System Dynamics, Supplement 33, pp. 47-58, 1999.

Andrianov, E.I. and N.I. Mogilko, "Measurement of the Tensile Strength of Pulverized and Powdered Materials," Journal of Applied Chemistry, Vol. 61, Issue 5, pp. 1058-1063, 1988.

Antony, S. J., R. Moreno-Atanasio, and A. Hassanpour, "Influence of Contact Stiffnesses on the Micromechanical Characteristics of Dense Particulate Systems Subjected to Shearing," Applied Physics Letters, Vol. 89. 2006.

ASTM D 4791-99, "Standard Test Method for Flat Particles, Elongated Particles, or Flat and Elongated Particles in Coarse Aggregate," Annual Book of ASTM Standards, Vol. 04.03, American Society for Testing and Materials, Philadelphia, PA, 1999.

ASTM D 5821-95, "Standard Test Method for Determining the Percentage of Fractured Particles in Coarse Aggregate," Annual Book of ASTM Standards, Vol. 04.03, American Society for Testing and Materials, Philadelphia, PA, 1999.

Barbosa, R. E., "Discrete Element Models for Granular Materials and Rock Mass," PhD Thesis, University of Illinois at Urbana Champaign, 1990.

Barksdale, R. D., "Compressive Stress Pulse Time in Flexible Pavements for Use in Dynamic Testing," Highway Research Record 345, Highway Research Board, 1971.

Barksdale, R. D., "Laboratory Evaluation of Rutting in Basecourse Materials," Proc., 3rd Int. Conf. on Struct. Des. of Asphalt Pavement, pp 161-174, 1972.

Barksdale, R. D., "Performances of Crushed Stone Base Courses", Transportation Research Record, (TRB), National Research Council, Washington, D.C., No. 954, pp. 78-87, 1984.

Barksdale, R. D. and S. Y. Itani, "Influence of Aggregate Shape on Base Behavior", Transportation Research Record (TRB), National Research Council, Washington, D.C., No. 1227, pp. 173-182, 1989.

Barksdale, R. D., C. O. Pollard, T. Siegel, and S. Moeller, "Evaluation of the Effects of Aggregate on Rutting and Fatigue of Asphalt," Research Report, Georgia DOT Project 8812, GA Tech Project E20-835, Georgia Institute of Technology, 1992.

Barber, J. R., "The Solution of Elasticity Problems for the Half Space by the Method of Green and Collins," Appl. Sci. Res., 40, pp135-157, 1983.

Bejarano, M. and M.R. Thompson, "Subgrade Soil Evaluation for the Design of Airport Flexible Pavements," FAA Center of Excellence for Airport Pavement Research Final Report No. 8, Department of Civil Engineering, University of Illinois at Urbana-Champaign, Urbana, Illinois, September, 1999.

Benson, F. J., "Effects of Aggregate Size, Shape, and Surface Texture on the Properties of Bituminous Mixtures – A Literature Review," Highway Research Board Special Report 109, pp. 12-21, 1970.

Bentz, D. P. and E. J. Garboczi, "Digital Image Based Computer Modeling and Visualization of Cement-Based Materials," Transportation Research Record, No. 1526, pp. 129-134, 1996.

Birmann, F. and F. Raab, "To the Development of the Continuously Welded track," Eisenbahntechnische Rundschau, August, 1960.

Bishop, C., "Some Vibration and Repeated Loading Tests on Railway Ballast," Undergraduate Report, Queen's Univeristy, Kingston, Ontario, 1975.

Blazek, C., "The Role of Chemicals in Controlling Coal Dust Emissions," PRB Coal Use: Risk Management Strategies and Tactics, American Coal Council, Michigan, 2003.

Bonskowski, R., Watson, W.D., and F. Freme, "Coal Production in the United States - A Historical Overview," Energy Information Administration, Office of Coal, Nuclear, Electric and Alternate Fuels, 2006.

Bromberg, E.M., "The Stability of the Jointless track," Izd. Transport, 1966.

Brown, S. F. and A. F. L. Hyde, "Significance of Cyclic Confining Stress in Repeated Load Trixial Testing of Granular material," Transportation Research record 537, Transportation Research Board, pp 47-58, 1975.

Cable, J. K. and V. J. Marks, "Proceedings for the Automated Pavement Distress Data Collection Equipment Seminar," Ames, Iowa, June 12-15, 1990.

Cai, Z. and Raymond, G.P., "Modeling the Dynamic Response of Railway Track to Wheel/Rail Impact Loading," Structural Engineering and Mechanics, Vol.2, No.1, pp. 95-112, 1994

Chang, C. S., C. W. Adegoke, and E. T. Selig, "GEOTRACK Model for Railroad Track Performance," Journal of Geotechnical Engineering Div, ASCE, 106(GT11):1201-1218, 1980.

Chang, L., Y. Abdelrazig, and P. Chen, "Optical Imaging Method for Bridge Painting Maintenance and Inspection," Final Report, FHWA/IN/JTRP-99/11, Joint Transportation Research Program, Purdue University, 2000.

Cheung, L.W. and A.R. Dawson, "Effects of Particle and Mix Characteristics on the performance of some Granular materials," Transportation Research Record, No. 1787, pp. 90-98, 2002.

Chiang, C. C., "Effects of Water and Fines on Ballast Performance in Box Tests," Master of Science Degree Project Report No. AAR89-366P. University of Massachusetts, 1989.

Choubane B., C. L. Wu, and M. Tia, "Coarse Aggregate Effects on Elastic Moduli of Concrete," Transportation Research Record (TRB), No. 1547, National Research Council, Washington, D.C., pp. 29-34, 1996.

CN (Canadian National) Rail. "Ballast Performance in Concrete Tie Track," Prairie Region. Edmonton. CN, Geotechnical Service. Internal Report, 1987.

Collingwood, B. I., "An Investigation of the Cause of Railroad Ballast Fouling," Master of Science Degree Project Report No. AAR88-350P. University of Massachusetts, 1988.

Corn, M., Stein, F., Hammad, Y., Manekshaw, S., Freedman, R., and A.M. Hartstein, "Physical and Chemical Properties of Respirable Coal Dust from Two United States Mines," Pittsburgh Mining and Safety Research Center, U.S. Bureau of Mines, Pittsburgh, Pennsylvania, 1972.

Collop, A. C., G. R. McDowell, and Y. Lee, "Use of the Distinct Element Method to Model the Deformation Behavior of an Idealized Asphalt Mixture," The International Journal of Pavement Engineering, Vol. 5(1), pp.1-7, 2004

Cundall, P. A., "A Computer Model for Simulating Progressive, Large Scale Movements in Blocky Rock Systems," International Symposium on Rock Fracture, I.S.R.M., Nancy, France, 1971.

Cundall, P. A. and O. D. L. Strack, "A Discrete Numerical Model for Granular Assemblies," Geotechnique, 29(1), pp 47-65, 1979.

Cundall, P. A. "Formulation of a Three-Dimensional Distinct Element Model -- Part I. A Scheme to Detect and Represent Contacts in a system Composed of Many Polyhedral Blocks," Int. J. Rock Mech., Min. Sci. & Geomech. Abstr., 25(3), pp 107-116, 1988.

Cundall, P. A. and R. D. Hart, "Numerical Modeling of Discontinua," Engr. Comp., 9(2), 101-103, 1992.

Crawford, S., Murray, M., and J. Powell, "Development of a Mechanistic Model for the Determination of Track Modulus," In Proceedings of the 7th International Heavy Haul Conference, Brisbane, Australia, 2001.

Dawson, A. R., N. H. Thom, and J. L. Paute, "Mechanical Characteristics of Unbound Granular Materials as a Function of Condition," Flexible Pavements, Proc., Eur. Symp. Euroflex 1993, A.G. Correia, ed., Balkema, Rotterdam, The Netherlands, pp35-44, 1996.

de Larrard and, F., and Sedran, T., "Optimization of Ultra-High-Performance Concrete by the Use of a Packing Model," Cement and Concrete Research, Vol. 24, 1994.

Diana, G. and Cheli, F., "A Numerical Method to Define the Dynamic Behavior of A Train Running on A Deformable Structure," Meccanica, Vol. 23, pp. 242, 1988.

EIA (Energy Information Administration), "Domestic Distribution of U.S. Coal by Origin State, Customer, Destination and Method of Transportation, 2004," http://www.eia.doe.gov/cneaf/coal/page/coaldistrib/2004/d_04state.pdf, Washington D.C., U.S. Department of Energy, 2006a.

EIA (Energy Information Administration), "Annual Energy Outlook 2006 with Projections to 2030", Washington D.C., U.S. Department of Energy. http://www.eia.doe.gov/oiaf/archive/aeo06/pdf/0383(2006).pdf, 2006b

El-Mitiny, M. R., "Material Characterization for Studying Flexible Pavement Behavior in Fatigue and Permanent Deformation," PhD Report, Ohio State University, 1980.

Esveld, C., "Modern Railway Track," Second Edition, MRT-Productions, theNetherland, 2001.

Fitch, J., “A Much Closer Look at Particle Contamination,” Practicing Oil Analysis Magazine, Issue Number 200509, 2005

Fuller, W and Thompson, S. E, “The laws of proportioning concrete,” Transactions of theAmerican Society of Civil Engineers. Paper no 1053, pp 67-143, 1907.

Freedman, R.W. and A.G. Sharkey, Jr., “Recent Advances in the Analysis of Respirable Coal Dust for Free Silica, Trace Elements and Organic Constituents,” Annals of the New York Academy of Sciences, vol. 200, pp. 7-16, 1972.

Gaalaas, T., “Update on PRB Coal Transportation: Still a Hot Issue,” http://www.paceglobalcom/paceglobal/pdfs/publications/Recurring%20Articles/CA_pg32-35-June%202006.pdf, Marketwatch, 2006.

Ghaboussi, J and Barbosa, R. (1990), "Three-dimensional discrete element method for granular materials", International Journal for Numerical and Analytical Methods in Geomechanics,Vol.14,pp.451-72.

Gillette, W., “Railroads Work to Control Coal Dust,” Brotherhood of Locomotive Engineers and Trainmen, http://www.ble.org/pr/news/headline.asp?id=18974, 2007.

Glaser, S. D. and M. K. Haud, “Active Imaging of Sub-Millimeter-Scale Fractures in Rocks,” In Symposium Proceedings on Nondestructive and Automated Testing for Soil and Rock Properties, ASTM Committee D18 on Soil and Rock, San Diego, CA, January 15-16, 1998.

Goltermann, P., Johanson, V., and Palbol, L., “Packing of Aggregates: An Alternative Tool to Determine the Optimal Aggregate Mix,” ACI Material Journal, September-October, 1997.

Grassie, S.L. and Cox, S.J., “The Dynamic Response of Railway Track with Flexible Sleepers to High Frequency Vertical Excitation. Proceedings of the Institution of Mechanical Engineers, 198D, pp.117-124, 1984.

Han, X. and E. T. Selig, “Effects of Fouling on Ballast Settlement,” Proceeding of the 6th International Heavy Haul Railway Conference, Cape Town, South Africa, April, 1997.

Han, X. D., “Evaluation of Ballast Materials Based on Ballast Particle Characteristics and Functions,” PhD thesis, University of Massachusetts, 1998.

Hashash, Y. M. A., E. Nezami, Z. Dawei and J. Ghaboussi, “DBLOCK3D: A 3-D discrete element analysis code for simulation of granular media and soil-machine interaction,” NASA Workshop on Granular Materials in Lunar and Martian Exploration, Kennedy Space Center, Florida, 2005.

Hay, W.W., H.C. Peterson, D.E. Plotkin, and P.T. Bakas, "Lateral Stability of Ballast," Report for FRA, DOT-FR-30038, Washington, D.C., 1977.

Haynes, J. H. and E. J. Yoder, "Effects of Repeated Loading on Gravel and Crushed Stone base material used in the AASHTO Road Test," Highway Research Record 39, pp 82-86, 1963.

Heath, D. L. and M. J. Shenton, "The Behavior of Track Ballast under Repeated Loading Conditions," British Railway Report No. E.610D, 1968.

Herrin, M. and W. H. Goetz, "Effect of Aggregate Shape on Stability of Bituminous Mixes," Proceedings, Highway Research Board, Vol.33, 1945.

Hertz, H., "Ueber die Beruehrung Elastischer Koerper (On Contact between Elastic Bodies)," in Gesammelte Werke (Collected Works), Vol. 1, Leipzig, Germany, 1895.

Hills, D. A., D. Nowell, and A. Sackfield, "Mechanics of Elastic Contact," Butterworth-Heinemann Ltd, 1993.

Holubec, I. and E. D'Appolonia, "Effect of Particle Shape on the Engineering Properties of Granular Soils," ASTM STP 523, pp. 304-318, 1973.

Holtz, R.D. and W.D. Kovacs, *An Introduction to Geotechnical Engineering*, Prentice Hall, Englewood Cliffs, New Jersey, 1981.

Huang, E.J., "A Test for Evaluating the Geometric Characteristics of Coarse Aggregate Particles," Proceeding, Vol.62, ASTM, Philadelphia, PA, 1962.

Huang, E.Y., Squirer, L.R., and Triffo, R.P., "Effect of Geometric Characteristics of Coarse Aggregate on Compaction Characteristics of Soil-Aggregate Mixture," Highway Research Record, 22, 1963.

Huang, E.Y., Auer, A., and Triffo, R.P., "Effect of Geometric Characteristics of Coarse Aggregate on Strength of Soil-Aggregate Mixtures," Proceedings, Vol. 64, ASTM, Philadelphia, PA, 1964.

Huang, H., Dombrow, W., and Tutumluer, E., "Laboratory Characterization of Fouled Railroad Ballast Behavior," accepted for publication by Transportation Research Record, 2009.

Huang, H., Tutumluer, E., Hashash, Y.M.A., and Gharboussi, J., "Contact Stiffness Affecting Discrete Element Modeling of Unbound Aggregate Granular Assemblies," Advances in Transportation Geotechnics, Taylors & Francis, London, 2008.

Huang, Y. H., Lin, C., Deng, X., and Rose, J., KENTRACK, A Computer Program for Hot-Mix Asphalt and Conventional Ballast Railway Trackbeds. Asphalt Institute (Publication RR-84-1) and National Asphalt Pavement Association (Publication QIP-105), 164 pages, 1984.

Indraratna, B., Khabbaz, H., Salim, W., Lackenby, J. and Christie, D., "Ballast Characteristics and the Effects of Geosynthetics on Rail Track deformation," Int. Conference on Geosynthetics and Geoenvironmental Engineering, Mumbai, India, 2004.

Indraratna, B., and Salim, W., Mechanics of Ballasted Rail Tracks – A Geotechnical Perspective. Taylors & Francis, London, UK, 2005.

Ishibashi, I., Y. C. Chen, and J. T. Jenkins, "Dynamic Shear Modulus and Fabric: Stress Reversal," Geotechnique, 38, No. 1, pp. 33-37, 1988.

Jankovic, Slobodanka, "Mechanical Properties of Light Compositive Biobriquettes", Facta Universitatis, Working and Living Environmental Protection Series, vol. 1, no.2, pp. 59-64, 1997.

Jezequel, L., "Response of Periodic System to A Moving Load," Journal of Applied Mechanics, Vol. 48, pp.613-618, 1981.

Johansen, V., and Andersen, P.J., "Particle Packing and Concrete Properties," Materials Science of Concrete II, The American Ceramic Society, 1990.

Johnson, K. L., "Contact Mechanics," Cambridge University Press, 1987.

Kalker, J. J., "Three-dimensional elastic bodies in rolling contact," Kluwer Academic Publishers, Dordrecht/Boston/London, 1990.

Kalker, J.J., "Discretely Supported Rails Subjected to Transient Loads," Vehicle System Dynamics, Vol. 25, pp. 71-88, 1996.

Kerr, A. D., "The Lateral Buckling of Railroad Tracks Due to Constrained Thermal Expansions," FRA Report DOT-FR-40017, 1975.

Khedr, S., "Deformation Characteristics of Granular Base Course in Flexible Pavement," Transportation Research Record, 1043, pp.131-138, 1985.

Kim, I.T. and Tutumluer, E., "Field Validation of Airport Pavement Granular Layer Rutting Predictions," In Transportation Research Record 1952, Journal of the Transportation Research Board, National Research Council, Washington, D.C., pp. 48-57, 2006.

Kish, A. and G. Samavedam, “Dynamic Buckling Test Analyses of a High Degree CWR Track,” FRA Report DOT/FRA/ORD-90/13, 1991.

Kish, A., D. Clark, and W. Thompson, “Recent Investigations on the Lateral Stability of Wood and Concrete Tie Tracks,” AREA Bulletin, Vol. 96, Bulletin 752, October 1995.

Knothe, K.L. and Grassie, S.L., “Modeling of Railway Track and Vehicle/Track Interaction at High Frequencies,” Vehicle System Dynamics, Vol. 22, pp. 209, 1993.

Knutson, R. M., “Factors Influencing the Repeated Load Behavior of Railway Ballast,” PhD Thesis, University of Illinois, Urbana, 1976.

Koerner, R. M., “The Behavior of Cohesionless Soils Formed from Various Minerals,” PhD thesis, Duke University, 1968.

Kose, S., M. Guler, H. U. Bahia, and E. Masad, “Distribution of Strains within Hot-Mix Asphalt Binders: Applying Imaging and Finite-Element Techniques,” Transportation Research Record No. 1728, National Research Council, Washington, D.C., pp. 21-27, 2000.

Li, D. and D. Davis, “Transition of Railroad Bridge Approaches,” ASCE Journal of Geotechnical and Geoenvironmental Engineering, 1392, 2005.

Li, M. C. and I. Kett, “Influence of Coarse Aggregate Shape on the Strength of Asphalt Concrete Mixtures,” Highway Research Record No. 178, pp. 93-106, 1967.

Lourens, J. P., “Towards Improved Understanding of Surface, Base, and Tyre Interaction for Low Cost pavement Design,” South Africa DOT Report No. RR93/559, Pretoria, South Africa.

Love, A. E. H., “A treatise on the mathematical theory of elasticity,” Cambridge University Press, Cambridge, 1927.

Marsal, R. J., “Mechanical Properties of Rockfill,” Embankment Dam Engineering, Casagrande Vol., New York, Wiley, pp. 109-200, 1973.

Masad, E., B. Muhunthan, N. Shashidhar, and T. Harman, "Internal Structure Characterization of Asphalt Concrete Using Image Analysis," Journal of Computing in Civil Engineering, Vol. 13, pp. 88-95, 1998.

Masad, E., B. Muhunthan, N. Shashidhar, and T. Harman, "Quantifying Laboratory Compaction Effects on the Internal Structure of Asphalt Concrete," Transportation Research Record (TRB), National Research Council, No. 1681, Washington, D.C., pp. 179-185, 1999.

Masad, E., D. Olcott, T. White, and L. Tashman, “Correlation of Imaging Shape Indices of Fine Aggregate with Asphalt Mixture Performance,” Presented at the 80th Annual Meeting of the Transportation Research Board, National Research Council, Washington D.C., 2001.

Masad, E., T. Al-Rousan, J. Button, D. Little, and E. Tutumluer, “Test Methods for Characterizing Aggregate Shape, Texture and Angularity, NCHRP 4-30A Final Report, Report Number 555, National Cooperative Highway Research Program, National Research Council, Washington, D.C., 2005.

Monismith, C. L., “Influence of Shape, Size, and Surface Texture on the Stiffness and Fatigue Response of Asphalt Mixtures,” Highway Research Board Special Report No. 109, pp. 4-11, 1970.

Monismith, C. L., N. Ogawa, C. R. Freeme, “A Permanent Deformation Characteristics of Subgrade Soils due to Repeated loading,” Transportation research Record 537, pp. 1-17, 1975.

Morrison, M.B., “Transportation of U.S. Western Coal: The Impact of Deregulation on Unit Train Rates,” Energy Policy, June 1985, pp. 243-252, 1985.

National Coal Council, “Coal: America's Energy Future, Volumes I,” National Coal Council, Washington D.C., pp. 132, 2006,

National Stone Association, “The Aggregate Handbook,” Edited by R.D. Barksdale, 1991.

National Institute of Standards and Technology, “Sulfur, Mercury and Chlorine in Coal,” Standard Reference Material No. 2682b, Gaithersburg, Maryland, 2007.

Nezami. E. G., D. Zhao, Y. M. A. Hashash, and J. Ghaboussi, "A Fast Contact Detection Algorithm for 3-D Disrecte Element Method," Computers and Geotechnics, Vol 31, pp. 575-587, 2004.

Nezami, E. G., Y. M. A. Hashash, D. Zhao, and J. Ghaboussi, “Shortest link method for contact detection in discrete element method,” International Journal for Numerical and Analytical Methods in Geomechanics 30(8): 783 – 801, 2006.

Nezami, E. G., Y. M. A. Hashash, D. Zhao, and J. Ghaboussi, “Simulation of front end loader bucket-soil interaction using discrete element method,” International Journal for Numerical and Analytical Methods in Geomechanics, 31(9), pp. 1147 – 1162, 2007.

Norman, G. M., “Ballast Box Experiments for Evaluating Ballast Field Performance,” FRA report 82-291 P, 1982.

Norman, G. M., and Selig, E. T., "Ballast Performance Evaluation with Box Tests," AREA Bul. 692, Vol. 84, 207-239, 1983.

Ng, T. T.,"Input parameters of Discrete Element Method," ASCE Journal of Engineering Mechanics, Vol. 132, pp. 723-729, 2006.

Plotkin, D. and D. Davis, "Bridge Approaches and track Stiffness," FRA Report DOT/FRA/ORD/08-01, 2008.

Puzinauskas, V. P., "Influence of Mineral Aggregate Structure on Properties of Asphalt Paving Mixtures," Highway Research Record No. 51, pp. 1-18. 1964.

Pan, T., E. Tutumluer, and S. H. Carpenter, "Effect of Coarse Aggregate Morphology on Resilient Modulus of Hot-Mix Asphalt," Transportation Research Record, 1929, pp. 1-9, 2005.

Pan, T., E. Tutumluer, and J. Anochie-Boateng, "Aggregate Morphology Affecting Resilient Behavior of Unbound Granular Materials," Transportation Research Record, 1952, 2006.

Powers, T.C., "Geometric Properties of Particles and Aggregates," Journal of the PCA Research and Development Laboratories, Portland Cement Association, Vol.6, 1964.

Pullen, E.M., Pullen, M.D., and C. Pullen, "Fluid, Formulation and Method for Coal Dust Control," U.S. Patent No. 944089, 1994.

Raab, F., "The Stability of the Railway from New View Points," Zeitschrift des Vereins Deutscher Ingenieure, Vol. 78, 1934.

Rao, C., E. Tutumluer, and J. A. Stefanski, "Coarse Aggregate Shape and Size Properties Using a New Image Analyzer," ASTM Journal of Testing and Evaluation, JTEVA, Vol 29 (No.5), pp. 79-89, 2001.

Rao, C., E. Tutumluer, and I. T. Kim, "Quantification of Coarse Aggregate Angularity based on Image Analysis," Transportation Research Record (TRB), National Research Council, No. 1787, Washington, D.C., pp. 117-124, 2002.

Raschke, S. A., "Automated Imaging Approach for Soil GSD Analysis," In Proceedings of the Symposium on Nondestructive and Automated Testing for Soil and Rock Properties, ASTM Committee D18 on Soil and Rock, San Diego, CA, January 15-16, 1998.

Raymond, G. P., "Design for Railroad Ballast and Sub grade Support," Journal of the Geotechnical Engineering Division, January, 1978.

Raymond, G. P., “Railroad Ballast Load Ranking Classification,” Journal of geotechnical Engineering Division, October, 1979.

Raymond, G. P., “Track and Support Rehabilitation for a Mine Company Railroad,” Canadian Geotechnical Journal, Vol. 37, 2000.

Raymond, G. P., “Reinforced Ballast Behavior Subjected to Repeated Load,” Geotextiles and Geomemberanes, Vol.20, pp. 39-61, 2002.

Raymond, G. P. and I.Ismail, “The Effect of Geogrid Reinforcement on Unbound Aggregates,” Geotextiles and Geomemberanes, Vol.21, pp. 355-380, 2003.

Rice, G.S. and H.P. Greenwald, “Coal Dust Explosibility Factors Indicated by Experimental Mine Investigations 1911 to 1929”, U.S. Bureau of Mines Technical Paper 464, pp. 44, 1929.

Roberts, F., Kandle, P., Brown, E.R., Lee, D., and Kennedy, T. Hot Mix Asphalt Materials, Mixture Design and Construction. NAPA Research and Education Foundation, Second Edition, 1996.

Rose, J., Su, B., and Long, W.B., “KENTRACK: A Railway Trackbed Structural Design and Analysis Program,” AREMA Conference, 2003.

Roy, D.M., Scheetz, B.E., and Silsbee, M.R., “ Processing of Optimized Cements and Concretes Via Particle Packing,” MRS Bulletin, March, 1993.

Samavedam, G., F. Blader, D. Wormley, M. Snyder, and D. Thomson, “Analyses of Track Shift Under High Speed Vehicle-Track Interaction,” FRA Report DOT/FRA/ORD-97/02, 1997.

Samavedam, G., A. Kanaan, J. Pietrak, A. Kish, and A. Sluz, “Wood Tie Track Resistance Characterization and Correlations Study,” FRA Report DOT/FRA/ORD - 94/07, Final Report, 1995.

Santamarina, J. C. and G. C. Cho, “Soil Behavior: the Role of Particle Shape,” Proceedings of Skempton Conference, London, 2004.

Sapko, M.J., Cashdollar, K.L., and G.M. Green, “Coal Dust Particle Size Survey of U.S. Mines,” National Institute of Occupational Safety and Health, Pittsburgh, Pennsylvania, 2006.

Selig, E. T. "Tensile Zone Effects on Performance of Layered Systems," Geotechniqe, Vol 37, No.3, pp 247-254, 1987.

Selig, E. T., V. DelloRusso, and K. J. Laine, “Sources and Causes of Ballast Fouling,” Report No.R-805. Association of American Railroad (AAR), Technical Center, Chicago, 1992.

Selig, E.T., B. I. Collingwood, and S. W. Field, “Causes of Fouling in Track,” AREA Bulletin 717, 1988.

Selig, E. T. and J. M. Waters, “Track Geotechnology and Substructure Management,” Thomas Telford Publications, London, 1994.

Shilstone, J.M., “High Performance Concrete Mixtures for Durability,” High Performance Concrete, 1990.

Stewart, H.E., Selig, E.T., and Norman, G.M., “Failure Criteria and Lateral Stresses in Track Foundations,” Transportation Research Record, 1022, pp 59-64, 1985.

Tayabji, S. D. and M. Thompson, “Consideration in the Analysis of Conventional Railway Track Support System,” ASCE Transportation Engineering Journal, 103(TE2):279-292, 1977.

Terzaghi, K., Peck, R.B., and G. Mesri, *Soil Mechanics in Engineering Practice*, 3rd edition, Wiley-Interscience Publication, 1996.

Thom, N. H., and S. F. Brown, “Effect of Grading and Density on the Mechanical Properties of a Crushed Dolomite Limestone,” Proc., 14th ARRB Conf., Part 7, pp94-100, 1988.

Thompson, M. R. and D. Nauman, “Rutting Rate Analysis of the AASHO Road Test Flexible Pavement,” Transportation Research Record, 1384, pp. 36-48, 1993.

Thornton, C. and D. J. Barmes, "Computer Simulated Deformation of Compact Granular Assemblies," Acta Mechanica, Vol 64, pp. 45-61, 1986.

Tien, J.C. and J. Kim, “Respirable Coal Dust Control Using Surfactants,” Fuel and Energy Abstracts, Elsevier Publications, Vol. 39, No.3, pp. 224, 1998.

Toufar, W., Born, M., and Klose, E., “Beitrag zur Optimierung der Packungsdichte Polydisperse Korniger Systeme,” Freiberger Forschungsheft A 588, VEB Deutscher Verlag fur Grundstoffindustrie, 1976.

Tseng, K. H., and R. L. Lytton, “Prediction of Permanent Deformation in Flexible Pavement Material. Implication of aggregate in Design, Construction, and Performance of Flexible Pavements,” ASTM STP 1016, 1987.

Tutumluer, E., "Prediction Behavior of Flexible Pavements with Granular Bases," PhD Thesis, Georgia Institute of Technology, 1995.

Tutumluer, E., H. Huang, Y. M. A. Hashash, and J. Ghaboussi, "Aggregate Shape Effects on Ballast Tamping and Railroad Track Lateral Stability," AREMA Conference, 2006.

Tutumluer, E., H. Huang, Y. M. A. Hashash, and J. Ghaboussi, "Discrete Element Modeling of Railroad Ballast Settlement," AREMA Conference, 2007.

Tutumluer, E., H. Huang, Y. M. A. Hashash, and J. Ghaboussi, "Contact Stiffness Affecting Discrete Element Modeling of Unbound Aggregate Granular Assemblies," 7th UNBAR Conference, Nottingham, 2008.

Ullidtz, P., "Stresses and Strains in A Two-Dimensional Particulate Material," Paper No: 950142, Transportation Research Board, 74th Annual Meeting, National Research Council, Washington D.C., 1995.

Vallerga, B. A., H. B. Seed, C. L. Monismith, and R.S. Cooper, "Effect of Shape, Size, and Roughness of Aggregate Particles on the Strength of Granular Materials," Special Technical Publication, No.212, ASTM, 1957.

Vavrik, W.R. Asphalt Mixture Design Concepts to Develop Aggregate Interlock, PhD Thesis, University of Illinois at Urbana-Champaign, July 2000.

Van Niekerk, A. A., "Mechanical Behavior and performance of Granular Bases and Subbases in Pavements." PhD Report, Technische Universiteit Delft, Delft, the Netherlands, 2002.

Werkmeister, S., A. R. Dawson, and F. Wellner, "Permanent Deformation Behavior of Granular Materials and the Shakedown Theory," Transportation Research Record, 1757, pp75-81, 2001.

Wilson, J. D., L. D. Klotz, and C. Nagaraj, "Automated Measurement of Aggregate Indices of Shape," Particulate Science and Technology, Vol. 15, pp. 13-35, October 1997.

Wong, R. C. T., "One Dimensional Repeated Loading Test of Railway Ballast," M.S. Thesis, Queen's University, Kingston, Ontario, 1975.

Yeggoni, M., J. W. Button, and D. G. Zollinger, "Influence of Coarse Aggregate Shape and Surface Texture on Rutting of Hot Mix Asphalt," Research Report 1244-6, Texas Transportation Institute, Texas A&M University System, October 1994.

Yue, Z. Q., W. Bekking, and I. Morin, "Application of Digital Image Processing to Quantitative Study of Asphalt Concrete Microstructure," Transportation Research Record (TRB), National Research Council, No. 1492, pp. 53-60, 1995.

Zhai, W., "The Vertical Model of Vehicle-Track System and Its Coupling Dynamics (in Chinese)," Journal of the China Railway Society 14(3), pp. 21-29, 1992.

Zhao, D., E. G. Nezami, Y. M. A. Hashash, and J. Ghaboussi, "Three-dimensional Discrete Element Simulation for granular Materials," Engineering Computations, 23(7), pp.749-770, 2006.

APPENDIX

A. EXAMPLE – DIRECT SHEAR BOX SIMULATION

1. Current functions of BLOCKS3D are listed as below.

1) CNFG
Change configuration variables from their default values.
2) INIT
Initialize global variables.
3) RRST
Read a restart file and set global variables.
4) WRST
Write to a restart file.
5) GENB
Generate individual particles from the input file or use particle prototypes in library, and back up all the information in the initial restart file.
6) GENM
Generate master blocks from the input file or use master prototypes in library, and back up all the information in the initial restart file.
7) CHNG
Change control parameters like time step length, contact properties, gravity, damping ratio, contact detection tolerance, etc.
8) ZVEL
Reset all particles' velocities to be zero.
9) RUNN
Run the program for the number of time steps specified by the user.
10) ABND
Add boundaries.
11) EBND
Eliminate boundaries.
12) MBND
Move boundaries according to the boundary condition specified by the user.
13) MBLK
Move blocks according to the boundary condition specified by the user.
14) CBLK
Copy a large number of blocks to the place specified by the user.
15) AMAT
Add new material types.
16) AFRC
Add constant force or moment to a rigid individual block at specified time step.
17) EHBK
Delete blocks whose any corner is higher than a user-specified threshold.
18) SKCT
Skip contact between specific material groups during contact detection.

2. Example of Direct Shear Box Simulation

```
//          njobs
4
//Initialization
INIT
//          number of materials
3
//          modulus; poison's ratio; density
97900000 0.25 30000
97900000 0.25 30000
97900000 0.25 30000
//contact stiffnesses and surface friction angle
2000000 1000000 0 (contact 1 to 1)
2000000 1000000 0 (contact 1 to 2)
2000000 1000000 0 (contact 1 to 3)
2000000 1000000 0 (contact 2 to 2)
2000000 1000000 0 (contact 2 to 3)
2000000 1000000 0 (contact 3 to 3)
//          gravity constant
0.0 0.0 -9.8
//          minimum edge size; maximum edge size; minimum block size; maximum block size;
0.002 0.04445 0.01334 0.02
//  Gradation data
//
//    gradation
4
0.01778 0
0.02667 0.38
0.03540 0.82
0.04445 1
//          local damping; global damping; fraction number, POWER2
0.4 0.0 0.15 3
//          simulation domain size; (IXBOXES, IYBOXES, IZBOXES, BSIZE (m))
24  12  40  0.1
//          generating boundary
ABND
6
1
0.9       0.9       0.05
0.0       0.0       1.0
0
1
0.35      0.9       0.05
1         0.0       0
0
1
0.746240.9        0.05
```

-1 0.0 0
0
1
0.9 0.05 0.05
0.0 1 0
0
1
0.9 0.395440.05
0.0 -1 0
0
1
0.9 0.9 0.55
0.0 0.0 1.0
0
//
GENB
LIBRARY
//
72
// For all particles, use the same material type:
0
// For every particle:
// Centroid (generation point)
0.45 0.15 0.7
0.55 0.15 0.7
0.65 0.15 0.7
……
0.45 0.25 1.8
0.55 0.25 1.8
0.65 0.25 1.8
// motion
RUNN
// NCYCLE, NPRINT, NPLOT, NRESTART
200000 200000 200000 200000
//Copy Particles
3
RRST
rsts7a_200000
CBLK
0 71
0 0 1
RUNN
// NCYCLE NPRINT NPLOT NRESTART
200000 200000 200000 200000
//Copy more particles
3
RRST
rsts7b_200000
CBLK
0 143
0 0 1

RUNN
// NCYCLE NPRINT NPLOT NRESTART
200000 200000 200000 200000
//Create a close space for mixing
3
RRST
rsts7d_200000
ABND
1
1
0.9 0.9 1.8
0.0 0.0 -1.0
0
RUNN
// NCYCLE NPRINT NPLOT NRESTART
100000 100000 10000 100000
//Mixing
3
RRST
rsts7dd_100000
CHNG
GRAVITY
0 0 9.8
RUNN
// NCYCLE NPRINT NPLOT NRESTART
100000 100000 100000 100000
//Generate shear boxes
4
RRST
rsts7dd4_100000
GENM
LIBRARY
4
//
11 1 1
0.0253
0 0 0
0.54812 0.22272 0.15
2
1 0 0
1 0 0
0 0
1 0 1
0 1 0
0 0
//
12 1 1
0.01016
0 0 0
0.54812 0.22272 0.1128
2

1 0 0
1 0 0
0 0
1 0 2
0 0 1
0 0
//
5 1 1
0.01016
0 0 0
0.57352 0.22272 0.294
2
1 0 1
0 1 0
0 0
1 0 2
0 0 1
0 0
//
9 1 1
0.1883
0 0 0
0.3754 0.22272 0.32
2
1 0 2
0 0 1
0 0
1 0 1
0 1 0
0 0
EBND
2
5
6
RUNN
// NCYCLE NPRINT NPLOT NRESTART
200000 200000 200000 200000
//Apply normal presure
4
RRST
rsts7dddddd1_2000
SKCT
1
1 2
AFRC
576 0
FORCE
0 0 20000
RUNN
// NCYCLE NPRINT NPLOT NRESTART
10000 10000 10000 10000

//Start shearing
5
RRST
rsts7f_2000
SKCT
1
1 2
EBND
1
2
MBLK
1
1
3
1
1
0
-1
1 0 0
0.09 0.000212
RUNN
// NCYCLE NPRINT NPLOT NRESTART
600000 600000 600000 600000

B. BLOKS3D LIBRARIES

Cube

```
//        Every particle has unit volume
//        Number of corners; Number of faces; Number of edges
//        Corner coordinates relative to the centroid.
//        Number of corners on every face
//        Order of corners in anti-clockwise order when facing the face normal
//        Start from 0
//        Every node's neighbor nodes information, start from 0
//        Largest distance from centroid to the farest corner
 8        6         12
-0.5     -0.5     -0.5
 0.5     -0.5     -0.5
 0.5      0.5     -0.5
-0.5      0.5     -0.5
-0.5     -0.5      0.5
 0.5     -0.5      0.5
 0.5      0.5      0.5
-0.5      0.5      0.5
4 0 1 5 4
4 1 2 6 5
4 3 7 6 2
4 0 4 7 3
4 0 3 2 1
4 4 5 6 7
3 1 3 4
3 2 0 5
3 3 1 6
3 7 0 2
3 5 0 7
3 1 4 6
3 7 2 5
3 4 3 6
0.866026
//
```

Library 1

```
              6           7          11
-0.1694608235820270     1.0878172809084900     -0.0113619645125291
-0.7845655908198820     -0.4499446386861430    0.6037428037253250
-0.1694608235820270     -0.4499446386861430    -0.9340191158693110
1.0607487128936800      -0.4499446386861430    0.6037428037253250
-0.4001251106712230     0.5111565621855030     -0.3573583961463220
0.2918677525963630      0.5111565621855030     -0.3573583961463220
3 0 1 3
3 2 3 1
3 0 4 1
3 4 2 1
4 0 5 2 4
3 0 3 5
3 3 2 5
4 4 5 3 1
4 0 3 2 4
4 3 5 4 1
4 0 5 2 1
3 0 1 2
```

3 0 2 3
1.30082411679601
//
Library 2
10 9 17
-0.2465620095971660 -0.3923464486607380 0.6635139110531050
0.6138246537971790 -0.3923464486607380 0.6635139110531050
0.9006202082619610 -0.3923464486607380 -0.1968727533412390
0.0402335448676159 -0.3923464486607380 -0.7704638622708030
0.4957323663705040 0.1137633534535820 -0.4667979806022110
-0.5554187616361600 0.2694894455656820 -0.3733623249349510
-0.2465620095971660 1.0416313236631700 0.0899228021235415
-0.4759984531689910 0.4680402147336070 0.3193592456953670
0.6547954471492910 -0.0850654975199005 0.5406015299967700
-0.8201531185267290 -0.3923464486607380 -0.1968727533412390
5 0 1 8 6 7
3 1 2 8
4 2 4 6 8
3 2 3 4
4 4 3 5 6
3 0 7 9
4 5 9 7 6
3 3 9 5
5 0 9 3 2 1
3 7 1 9
3 0 8 2
4 3 1 8 4
4 5 9 2 4
3 6 3 2
3 6 9 3
4 8 7 5 4
3 0 9 6
3 1 6 2
4 0 3 5 7
1.0741856214615000
//
Library 3
28 16 42
0.4070750071833960 0.4477104520710910 -0.3895540720475940
0.2503922649931950 0.6043931942612920 -0.2328713318573900
-0.2503184240642680 0.6043931942612920 -0.2328713318573900
-0.4070011652544700 0.4477104520710910 -0.3895540720475940
-0.6043743472794320 0.2503372700461280 -0.1409231583590680
-0.6043743472794320 -0.2503734190113340 -0.1409231583590680
-0.3625562910334160 -0.4921914752573510 0.3800772251692200
-0.2503184240642680 -0.6044293432264980 0.2678393572000730
0.2503922649931950 -0.6044293432264980 0.2678393572000730
0.3626301329623420 -0.4921914752573510 0.3800772251692200
0.6044481892083580 -0.2503734190113340 -0.1409231583590680
0.6044481892083580 0.2503372700461280 -0.1409231583590680
0.3626301329623420 0.4921553252921460 0.3800772251692200
0.2503922649931950 0.6043931942612920 0.2678393572000730
-0.2503184240642680 0.6043931942612920 0.2678393572000730
-0.3625562910334160 0.4921553252921460 0.3800772251692200
-0.2503184240642680 0.2503372700461280 0.6218952814152360
-0.2503184240642680 -0.2503734190113340 0.6218952814152360

0.2503922649931950 -0.2503734190113340 0.6218952814152360
0.2503922649931950 0.2503372700461280 0.6218952814152360
0.2503922649931950 0.2503372700461280 -0.5869272540725560
-0.2503184240642680 0.2503372700461280 -0.5869272540725560
-0.2503184240642680 -0.2503734190113340 -0.5869272540725560
0.2503922649931950 -0.2503734190113340 -0.5869272540725560
0.4070750071833960 -0.4477466020362960 -0.3895540720475940
0.2503922649931950 -0.6044293432264980 -0.2328713318573900
-0.2503184240642680 -0.6044293432264980 -0.2328713318573900
-0.4070011652544700 -0.4477466020362960 -0.3895540720475940
6 0 11 10 24 23 20
5 10 9 8 25 24
6 9 10 11 12 19 18
5 0 1 13 12 11
4 1 2 14 13
6 12 13 14 15 16 19
4 16 17 18 19
6 6 7 8 9 18 17
4 7 26 25 8
6 23 24 25 26 27 22
4 23 22 21 20
6 0 20 21 3 2 1
5 2 3 4 15 14
6 4 5 6 17 16 15
5 5 27 26 7 6
6 3 21 22 27 5 4
3 1 20 11
3 2 0 13
3 14 3 1
3 4 21 2
3 15 5 3
3 27 4 6
3 17 7 5
3 8 26 6
3 9 25 7
3 10 8 18
3 9 11 24
3 0 10 12
3 13 11 19
3 12 14 1
3 13 15 2
3 14 16 4
3 19 17 15
3 18 6 16
3 9 17 19
3 12 18 16
3 0 21 23
3 20 3 22
3 23 21 27
3 24 20 22
3 10 23 25
3 8 24 26
3 25 27 7
3 22 5 26
0.7198692650340250
//

Library 4

28 18 44

0.4254514979111890 0.4106636864106340 0.4149508885978020
0.5684762836292130 0.3280882876319440 0.3323754918191100
0.5684762836292130 -0.3283734251788300 0.3323754918191100
0.4254514979111890 -0.4109488219575220 0.4149508885978020
-0.0000362362424167 -0.6566042805842190 -0.0105368442558058
-0.4069085993778770 -0.4216964118784300 -0.4174092086912640
-0.5685487555140470 -0.3283734231788330 -0.3240862209916650
-0.5685487555140470 0.3280882876319440 -0.3240862209916650
-0.4069085993778770 0.4214112753315430 -0.4174092086912640
-0.0000362362424167 0.6563191440373320 -0.0105368442558058
0.5684762836292130 0.3280882876319440 -0.3240862209916650
0.5684762836292130 -0.3283734231788330 -0.3240862209916650
0.4068361274930420 -0.4216964118784300 -0.4174092086912640
0.1268671643942450 -0.3283734231788330 -0.5790493638274360
-0.1269396372790780 -0.3283734231788330 -0.5790493638274360
-0.0000362362424167 0.0371246810048347 -0.6523170763970530
-0.1269396372790780 0.3280882876319440 -0.5790493638274360
0.1268671643942450 0.3280882876319440 -0.5790493638274360
0.4068361274930420 0.4214112753315430 -0.4174092086912640
0.1777253035751180 0.3280882876319440 0.5579756743158260
-0.0000362362424167 0.0371246810048347 0.6606063472244980
0.1777253035751180 -0.3283734231788330 0.5579756743158260
-0.1777977764599510 -0.3283734231788330 0.5579756743158260
-0.4255239707960220 -0.4109488219575220 0.4149508885978020
-0.5685487555140470 -0.3283734231788330 0.3323754918191100
-0.5685487555140470 0.3280882876319440 0.3323754918191100
-0.4255239707960220 0.4106636864106340 0.4149508885978020
-0.1777977764599510 0.3280882876319440 0.5579756743158260
5 0 1 10 18 9
5 8 9 18 17 16
5 8 7 25 26 9
5 0 9 26 27 19
4 1 2 11 10
7 15 17 18 10 11 12 13
3 15 16 17
3 13 14 15
7 5 6 7 8 16 15 14
4 6 24 25 7
7 24 23 22 20 27 26 25
3 20 19 27
3 21 20 22
7 0 19 20 21 3 2 1
5 2 3 4 12 11
5 4 5 14 13 12
5 4 23 24 6 5
5 4 3 21 22 23
3 1 19 9
3 0 10 2
3 11 3 1
3 21 2 4
4 12 5 23 3
3 14 6 4
3 7 24 5
3 8 25 6

3 9 7 16
4 0 26 8 18
3 18 11 1
3 10 12 2
3 11 13 4
3 15 14 12
3 15 5 13
4 16 14 13 17
3 8 15 17
3 16 15 18
3 9 17 10
3 0 20 27
4 22 27 19 21
3 22 20 3
3 20 21 23
3 24 22 4
3 25 23 6
3 7 26 24
3 9 27 25
3 26 19 20
0.7359009851934920
//

Library 5

6 7 11

-0.2365388599877310	-0.5913431349693270	0.5744676919702020
-1.0474991269456700	-0.5913431349693270	-0.2364925739877330
-0.2365388599877310	1.4360575299255100	-0.2364925739877330
1.3853816719281400	-0.5913431349693270	-0.2364925739877330
0.5744214049702050	0.4223571979780920	0.1689875589912350
-0.6420189939666980	0.4223571979780920	0.1689875589912350

3 0 1 3
3 1 2 3
3 0 3 4
3 2 4 3
4 0 4 2 5
3 0 5 1
3 1 5 2
4 1 5 4 3
4 0 3 2 5
4 3 4 5 1
4 0 4 2 1
3 0 2 3
3 0 1 2
1.5247615609468600
//

Library 6

12 9 19

0.6611939819294730	-0.6336338989324120	0.3632122219612570
0.6611939819294730	-0.6336338989324120	-0.3686187889606810
0.7869774369160560	0.6242006509334190	-0.1170518799875140
-0.0706370289924654	1.1959436268724300	-0.0027032839997117
-1.0507678458879200	0.5425230819421310	0.1279808249863490
-1.0729273258855500	0.3209282889657680	0.1722997829816210
-0.4365525339534340	-0.6336338989324120	0.3632122219612570
0.9426674468994490	0.2107864979775160	0.1943281419792720
0.9094937889029870	0.5425230819421310	0.1279808249863490

-0.4365525339534340 -0.6336338989324120 -0.3686187889606810
-0.8670413639075160 0.0120993449987094 -0.2394721409744560
-0.9282514949009870 0.6242006509334190 -0.1170518799875140
7 0 7 8 3 4 5 6
6 1 9 10 11 3 2
4 0 6 9 1
3 0 1 7
4 1 2 8 7
3 2 3 8
3 3 11 4
4 11 10 5 4
4 10 9 6 5
3 7 1 6
4 0 7 2 9
3 3 1 8
4 4 11 2 8
3 5 11 3
3 6 10 4
3 0 9 5
3 0 8 1
3 3 2 7
3 10 6 1
3 11 5 9
3 3 4 10
1.1980309078926400
//
Library 7
22 14 34
-0.5183115004607050 0.6442156917570250 0.2057284418526500
-0.0469227524366286 0.9163721118825800 0.0489124483596769
0.5688798802595780 0.5608382956954320 0.2537703315585970
0.7467125822514060 0.4581665374714740 -0.0483570352185918
0.7467125822514060 -0.4582446113507370 -0.0483570352185918
0.5911122118785400 -0.5480805284245940 -0.2415402094717860
-0.0469227524366286 -0.9164501857618430 0.0489124493596754
-0.5845856609714810 -0.6060303608084700 -0.1958478371324440
-0.8405580881246620 -0.4582446113507370 -0.0483570352185918
-0.8405580881246620 0.4581665374714740 -0.0483570352185918
-0.5845856529714930 0.6059522919292000 -0.1958478411324380
-0.3823525127135570 0.4581665434714650 -0.3123741719310860
0.5911122068785480 0.5480024555453300 -0.2415402154717770
0.5340586351086560 0.4581665434714650 -0.3123741719310860
0.5340586351086560 -0.4582446063507450 -0.3123741719310860
-0.3823525127135570 -0.4582446063507450 -0.3123741719310860
-0.3823525127135570 0.4581665434714650 0.3129295910721620
0.5340586351086560 0.4581665434714650 0.3129295910721620
0.5340586351086560 -0.4582446063507450 0.3129295910721620
0.5688798832595740 -0.5609163685746970 0.2537703265586040
-0.3823525127135570 -0.4582446063507450 0.3129295910721620
-0.5183115064606960 -0.6442937626362930 0.2057284378526570
4 0 1 10 9
5 1 12 13 11 10
4 1 2 3 12
5 0 16 17 2 1
6 7 8 9 10 11 15
6 8 21 20 16 0 9

4 11 13 14 15
6 3 4 5 14 13 12
6 2 17 18 19 4 3
4 16 20 18 17
5 6 7 15 14 5
4 7 6 21 8
4 5 4 19 6
5 6 19 18 20 21
3 1 16 9
4 0 10 12 2
3 3 17 1
3 12 4 2
3 5 19 3
3 14 6 4
4 7 21 19 5
3 15 8 6
3 9 21 7
3 0 8 10
3 9 11 1
3 10 15 13
3 1 13 3
3 11 14 12
3 15 5 13
3 7 14 11
3 0 17 20
3 2 18 16
3 17 19 20
3 4 6 18
3 18 21 16
3 6 8 20
0.9585741631188000
//

Library 8

32 18 48

-0.8374110048787260	-0.3468051989497760	-0.1150814849833340
-0.5921525329142450	-0.5920636689142570	-0.1983524749712750
-0.3468940619497630	-0.8373221408787390	-0.1150814849833340
-0.3468940619497630	-0.8373221408787390	0.1081315879843400
0.3468016499497760	-0.8373221408787390	0.1081315879843400
0.5920601209142580	-0.5920636689142570	0.1964867619715450
0.8373185928787400	-0.3468051989497760	0.1081315879843400
0.8373185928787400	0.3468905139497630	0.1081315879843400
0.5920601209142580	0.5921489859142450	0.1964867619715450
0.3468016499497760	0.8374074558787270	0.1081315879843400
0.3468016499497760	0.8374074558787270	-0.1150814849833340
-0.3468940619497630	0.8374074558787270	-0.1150814849833340
-0.5921525329142450	0.5921489859142450	-0.1983524749712750
-0.8374110048787260	0.3468905139497630	-0.1150814849833340
-0.8374110048787260	-0.3468051989497760	0.1081315879843400
-0.5921525329142450	-0.5920636689142570	0.1964867619715450
-0.3468940619497630	-0.3468051989497760	0.2848419359587490
0.3468016499497760	-0.3468051989497760	0.2848419359587490
0.3468016499497760	0.3468905139497630	0.2848419359587490
-0.3468940619497630	0.3468905139497630	0.2848419359587490
-0.3468940619497630	0.8374074558787270	0.1081315879843400
-0.5921525329142450	0.5921489859142450	0.1964867619715450

-0.8374110048787260 0.3468905139497630 0.1081315879843400
-0.3468940619497630 -0.3468051989497760 -0.2816234649592150
0.3468016499497760 -0.3468051989497760 -0.2816234649592150
0.3468016499497760 0.3468905139497630 -0.2816234649592150
-0.3468940619497630 0.3468905139497630 -0.2816234649592150
0.5920601209142580 -0.5920636689142570 -0.1983524749712750
0.3468016499497760 -0.8373221408787390 -0.1150814849833340
0.8373185928787400 -0.3468051989497760 -0.1150814849833340
0.8373185928787400 0.3468905139497630 -0.1150814849833340
0.5920601209142580 0.5921489859142450 -0.1983524749712750
6 0 1 2 3 15 14
4 0 14 22 13
6 11 12 13 22 21 20
6 14 15 16 19 21 22
6 0 13 12 26 23 1
6 3 4 5 17 16 15
4 16 17 18 19
6 21 19 18 8 9 20
4 9 10 11 20
6 11 10 31 25 26 12
4 25 24 23 26
6 1 23 24 27 28 2
4 3 2 28 4
6 5 6 7 8 18 17
6 30 31 10 9 8 7
6 24 25 31 30 29 27
6 4 28 27 29 6 5
4 6 29 30 7
3 14 1 13
3 0 2 23
3 28 1 3
3 4 2 15
3 5 28 3
3 6 4 17
3 7 29 5
3 8 30 6
3 9 7 18
3 10 8 20
3 11 31 9
3 20 12 10
3 13 26 11
3 0 12 22
3 0 22 15
3 3 14 16
3 17 15 19
3 18 5 16
3 8 17 19
3 18 16 21
3 21 11 9
3 19 22 20
3 14 13 21
3 24 26 1
3 27 25 23
3 31 26 24
3 25 12 23
3 29 24 28

3 4 27 2
3 6 30 27
3 7 31 29
3 10 25 30
0.9136924909105350
//
Library 9
8 6 12
-1.2042273675620200 -1.2688455449033400 -0.0343086327936389
-1.2858405249497400 -0.7791666025770630 0.0473045235940752
0.0199699882536787 1.1795491667280600 0.3737571521449290
0.0199699882536787 1.1795491667280600 -0.2383415252629230
1.4890068152325200 -0.2894876602507820 0.1289176809817880
0.8361015581308140 -1.2688455449033400 -0.0343086327936389
-1.0682054392491700 -0.4527139740262100 -0.1703305621064940
-0.3880957966848890 0.5674504883202090 -0.3403579714975650
3 0 1 6
5 3 7 6 1 2
4 0 6 7 5
4 3 4 5 7
3 2 4 3
5 0 5 4 2 1
3 1 5 6
3 0 6 2
3 3 4 1
3 4 2 7
3 3 5 2
3 0 4 7
3 0 7 1
3 3 6 5
1.7496598674858500
//
Library 10
10 9 17
-1.6449800249643600 0.2519580634938950 0.1677648167839150
0.1990933144429870 0.8666491756296770 0.1677648167839150
1.4284755407145500 0.2519580634938950 0.1677648167839150
0.8137844275787690 -0.9774241637776670 0.1677648167839150
-0.7229433547606850 -0.9774241637776670 0.1677648167839150
-1.0302889118285800 -0.5676300876871460 -0.0371322202613460
0.1990933144429870 0.2519580634938950 -0.4469262963518670
-0.7229433547606850 0.5593036185617870 -0.1395807392839760
0.8137844275787690 0.5593036185617870 -0.1395807392839760
1.0186814656240300 -0.5676300876871460 -0.0371322202613460
4 0 7 6 5
5 4 5 6 9 3
3 0 1 7
4 1 8 6 7
4 8 2 9 6
3 2 3 9
3 1 2 8
3 0 5 4
5 0 4 3 2 1
4 1 4 5 7
4 0 7 8 2
4 1 8 9 3

3 2 9 4
3 0 3 5
3 0 4 6
4 7 5 9 8
3 0 6 1
3 1 6 2
3 6 3 2
1.6725989304199200
//
Library 11
16 11 25
-0.7982475567367890 0.6414450407884920 -0.1365260379549820
-1.1799849316109200 0.4505763538514280 -0.0092802459969400
-1.1799849316109200 -0.5885976138059180 -0.0092802459969400
-0.5861712358067180 -0.6628243247814420 0.2876266019051590
1.1952698496058800 -0.8855044617080170 0.0331350179890742
1.4921766975079700 0.3021229299003790 -0.0092802459969400
0.7796002627429370 0.5396484068220580 -0.1874243549381990
0.3045493068995790 0.3021229299003790 -0.3061870938990390
-0.2892643889046190 0.3021229299003790 -0.3061870938990390
-0.2892643889046190 0.8959366247045770 -0.0092802459969400
-0.8830780847088170 0.5990297768024780 0.1391731779541090
-0.5861712358067180 0.3021229299003790 0.2876266019051590
0.5329391898242700 0.6218687647949470 0.1277536839578750
-0.9763916656780480 -0.6140467727975260 -0.0771446679745626
1.1952698496058800 -0.8855044617080170 -0.0092802459969400
1.2546512185863000 -0.6479789827863380 -0.0686616159773597
4 0 1 10 9
5 0 9 6 7 8
5 1 2 3 11 10
4 9 10 11 12
4 5 6 9 12
5 3 4 5 12 11
5 0 8 13 2 1
5 7 15 14 13 8
4 6 5 15 7
5 2 13 14 4 3
4 4 14 15 5
3 1 8 9
3 0 10 2
3 3 13 1
3 4 2 11
3 5 14 3
4 12 6 15 4
3 9 7 5
3 6 8 15
3 0 13 7
4 0 6 12 10
3 1 9 11
3 12 3 10
3 11 9 5
3 14 8 2
3 4 15 13
3 5 7 14
1.5224833937758300
//

Master 1: Tie

```
1 8
8 6 0
  -0.6477     -0.1016     -0.0889
   0.6477     -0.1016     -0.0889
   0.6477      0.1016     -0.0889
  -0.6477      0.1016     -0.0889
  -0.6477     -0.1016      0.0889
   0.6477     -0.1016      0.0889
   0.6477      0.1016      0.0889
  -0.6477      0.1016      0.0889
4         0         1         5         4
4         1         2         6         5
4         3         7         6         2
4         0         4         7         3
4         0         3         2         1
4         4         5         6         7
3         1         3         4
3         2         0         5
3         3         1         6
3         7         0         2
3         5         0         7
3         1         4         6
3         7         2         5
3         4         3         6
0.661620027
0 1 2 3 4 5 6 7
0.0                 0.0                 0.0
//
```

Master 2: bucket

```
5 28
8 6 0
-0.17     0.0217556         -0.04629829
-0.172    0.0217556         -0.04629829
-0.172    -0.0882444        -0.04629829
-0.17     -0.0882444        -0.04629829
-0.17     0.0502276         0.01764971
-0.172    0.0502276         0.01764971
-0.172    -0.0131624        0.09499171
-0.17     -0.0131624        0.09499171
4         0         1         5         4
4         1         2         6         5
4         3         7         6         2
4         0         4         7         3
4         0         3         2         1
4         4         5         6         7
3         1         3         4
3         2         0         5
3         3         1         6
3         7         0         2
3         5         0         7
3         1         4         6
3         7         2         5
3         4         3         6
0.09191773
4 16 17 5 8 18 19 9
```

-0.171 -0.01330363 0.0069159
8 6 0
-0.17 0.0217556 -0.04829829
-0.17 -0.0882444 -0.04829829
0.17 -0.0882444 -0.04829829
0.17 0.0217556 -0.04829829
-0.17 0.0217556 -0.04629829
-0.17 -0.0882444 -0.04629829
0.17 -0.0882444 -0.04629829
0.17 0.0217556 -0.04629829
4 0 1 5 4
4 1 2 6 5
4 3 7 6 2
4 0 4 7 3
4 0 3 2 1
4 4 5 6 7
3 1 3 4
3 2 0 5
3 3 1 6
3 7 0 2
3 5 0 7
3 1 4 6
3 7 2 5
3 4 3 6
0.178678482
0 1 2 3 4 5 6 7
0 -0.0332444 -0.04729829
8 6 0
0.172 0.0217556 -0.04629827
0.17 0.0217556 -0.04629829
0.17 -0.0882444 -0.04629829
0.172 -0.0882444 -0.04629829
0.172 0.0502276 0.01764971
0.17 0.0502276 0.01764971
0.17 -0.0131624 0.09499171
0.172 -0.0131624 0.09499171
4 0 1 5 4
4 1 2 6 5
4 3 7 6 2
4 0 4 7 3
4 0 3 2 1
4 4 5 6 7
3 1 3 4
3 2 0 5
3 3 1 6
3 7 0 2
3 5 0 7
3 1 4 6
3 7 2 5
3 4 3 6
0.09191773
20 7 6 21 22 11 10 23
0.171 -0.01330363 0.0069159
8 6 0
-0.17 0.0502276 0.01764971
-0.17 -0.0131624 0.09499171

0.17 -0.0131624 0.09499171
0.17 0.0502276 0.01764971
-0.17 0.05179645 0.01893556
-0.17 -0.01159355 0.09627756
0.17 -0.01159355 0.09627756
0.17 0.05176545 0.01893556
4 0 1 5 4
4 1 2 6 5
4 3 7 6 2
4 0 4 7 3
4 0 3 2 1
4 4 5 6 7
3 1 3 4
3 2 0 5
3 3 1 6
3 7 0 2
3 5 0 7
3 1 4 6
3 7 2 5
3 4 3 6
0.177203412
8 9 10 11 12 13 14 15
0 0.01931702 0.05696364
8 6 0
-0.17 0.02356005 -0.0471017
-0.17 0.0217556 -0.04629829
0.17 0.0217556 -0.04629829
0.17 0.02356005 -0.0471017
-0.17 0.05203205 0.0168463
-0.17 0.0502276 0.01764971
0.17 0.0502276 0.01764971
0.17 0.05203205 0.0168463
4 0 1 5 4
4 1 2 6 5
4 3 7 6 2
4 0 4 7 3
4 0 3 2 1
4 4 5 6 7
3 1 3 4
3 2 0 5
3 3 1 6
3 7 0 2
3 5 0 7
3 1 4 6
3 7 2 5
3 4 3 6
0.173568361
25 4 7 24 27 8 11 26
0 0.03689382 -0.01472599
//
Master 3: Tamper (left)
3 22
8 6 0
-1.365384615 0.5 -2.653846154
-1.365384615 -0.5 -2.653846154
-0.365384615 -0.5 -2.653846154

-0.365384615 0.5 -2.653846154
-1.365384615 0.5 5.346153846
-1.365384615 -0.5 5.346153846
-0.365384615 -0.5 5.346153846
-0.365384615 0.5 5.346153846
4 0 1 5 4
4 1 2 6 5
4 3 7 6 2
4 0 4 7 3
4 0 3 2 1
4 4 5 6 7
3 1 3 4
3 2 0 5
3 3 1 6
3 7 0 2
3 5 0 7
3 1 4 6
3 7 2 5
3 4 3 6
4.062019202
4 7 6 5 0 3 2 1
-0.865384615 0 1.346153846
8 6 0
-0.365384615 0.5 -2.653846154
-0.365384615 -0.5 -2.653846154
1.634615385 -0.5 -2.653846154
1.634615385 0.5 -2.653846154
-0.365384615 0.5 -1.653846154
-0.365384615 -0.5 -1.653846154
1.634615385 -0.5 -1.653846154
1.634615385 0.5 -1.653846154
4 0 1 5 4
4 1 2 6 5
4 3 7 6 2
4 0 4 7 3
4 0 3 2 1
4 4 5 6 7
3 1 3 4
3 2 0 5
3 3 1 6
3 7 0 2
3 5 0 7
3 1 4 6
3 7 2 5
3 4 3 6
1.224744871
5 6 9 8 13 12 11 10
0.634615385 0 -2.153846154
8 6 0
1.634615385 1 -3.653846154
1.634615385 -1 -3.653846154
2.134615385 -1 -3.653846154
2.134615385 1 -3.653846154
1.634615385 1 -0.653846154
1.634615385 -1 -0.653846154
2.134615385 -1 -0.653846154

2.134615385 1 -0.653846154
4 0 1 5 4
4 1 2 6 5
4 3 7 6 2
4 0 4 7 3
4 0 3 2 1
4 4 5 6 7
3 1 3 4
3 2 0 5
3 3 1 6
3 7 0 2
3 5 0 7
3 1 4 6
3 7 2 5
3 4 3 6
1.820027472
14 17 16 15 18 21 20 19
1.884615385 0 -2.153846154
//
Master 4: Tamper (right)
3 22
8 6 0
0.365384615 0.5 -2.653846154
0.365384615 -0.5 -2.653846154
1.365384615 -0.5 -2.653846154
1.365384615 0.5 -2.653846154
0.365384615 0.5 5.346153846
0.365384615 -0.5 5.346153846
1.365384615 -0.5 5.346153846
1.365384615 0.5 5.346153846
4 0 1 5 4
4 1 2 6 5
4 3 7 6 2
4 0 4 7 3
4 0 3 2 1
4 4 5 6 7
3 1 3 4
3 2 0 5
3 3 1 6
3 7 0 2
3 5 0 7
3 1 4 6
3 7 2 5
3 4 3 6
4.062019202
7 4 5 6 3 0 1 2
0.865384615 0 1.346153846
8 6 0
-1.634615385 0.5 -2.653846154
-1.634615385 -0.5 -2.653846154
0.365384615 -0.5 -2.653846154
0.365384615 0.5 -2.653846154
-1.634615385 0.5 -1.653846154
-1.634615385 -0.5 -1.653846154
0.365384615 -0.5 -1.653846154
0.365384615 0.5 -1.653846154

4 0 1 5 4
4 1 2 6 5
4 3 7 6 2
4 0 4 7 3
4 0 3 2 1
4 4 5 6 7
3 1 3 4
3 2 0 5
3 3 1 6
3 7 0 2
3 5 0 7
3 1 4 6
3 7 2 5
3 4 3 6
1.224744871
8 9 4 7 10 11 12 13
-0.634615385 0 -2.153846154
8 6 0
-2.134615385 1 -3.653846154
-2.134615385 -1 -3.653846154
-1.634615385 -1 -3.653846154
-1.634615385 1 -3.653846154
-2.134615385 1 -0.653846154
-2.134615385 -1 -0.653846154
-1.634615385 -1 -0.653846154
-1.634615385 1 -0.653846154
4 0 1 5 4
4 1 2 6 5
4 3 7 6 2
4 0 4 7 3
4 0 3 2 1
4 4 5 6 7
3 1 3 4
3 2 0 5
3 3 1 6
3 7 0 2
3 5 0 7
3 1 4 6
3 7 2 5
3 4 3 6
1.820027472
15 21 20 14 16 18 19 17
-1.884615385 0 -2.153846154
//
Master 5: Plate
1 8
8 6 0
-15 -15 -0.5
15 -15 -0.5
15 15 -0.5
-15 15 -0.5
-15 -15 0.5
15 -15 0.5
15 15 0.5
-15 15 0.5
4 0 1 5 4

4 1 2 6 5
4 3 7 6 2
4 0 4 7 3
4 0 3 2 1
4 4 5 6 7
3 1 3 4
3 2 0 5
3 3 1 6
3 7 0 2
3 5 0 7
3 1 4 6
3 7 2 5
3 4 3 6
21.21909517
0 1 2 3 4 5 6 7
0.0 0.0 0.0
//

Master 6: Upper Part of small Shear Box

4 24
8 6 0
-17 -15 -6
-15 -15 -6
-15 15 -6
-17 15 -6
-17 -15 6
-15 -15 6
-15 15 6
-17 15 6
4 0 1 5 4
4 1 2 6 5
4 3 7 6 2
4 0 4 7 3
4 0 3 2 1
4 4 5 6 7
3 1 3 4
3 2 0 5
3 3 1 6
3 7 0 2
3 5 0 7
3 1 4 6
3 7 2 5
3 4 3 6
16.18641406
8 7 6 5 4 3 2 1
-16 0 0
8 6 0
-17 -17 -6
17 -17 -6
17 -15 -6
-17 -15 -6
-17 -17 6
17 -17 6
17 -15 6
-17 -15 6
4 0 1 5 4
4 1 2 6 5

4 3 7 6 2
4 0 4 7 3
4 0 3 2 1
4 4 5 6 7
3 1 3 4
3 2 0 5
3 3 1 6
3 7 0 2
3 5 0 7
3 1 4 6
3 7 2 5
3 4 3 6
18.05547009
23 0 15 8 21 22 11 4
0 -16 0
8 6 0
15 -15 -6
17 -15 -6
17 15 -6
15 15 -6
15 -15 6
17 -15 6
17 15 6
15 15 6
4 0 1 5 4
4 1 2 6 5
4 3 7 6 2
4 0 4 7 3
4 0 3 2 1
4 4 5 6 7
3 1 3 4
3 2 0 5
3 3 1 6
3 7 0 2
3 5 0 7
3 1 4 6
3 7 2 5
3 4 3 6
16.18641406
16 15 14 13 12 11 10 9
16 0 0
8 6 0
-17 15 -6
17 15 -6
17 17 -6
-17 17 -6
-17 15 6
17 15 6
17 17 6
-17 17 6
4 0 1 5 4
4 1 2 6 5
4 3 7 6 2
4 0 4 7 3
4 0 3 2 1
4 4 5 6 7

3 1 3 4
3 2 0 5
3 3 1 6
3 7 0 2
3 5 0 7
3 1 4 6
3 7 2 5
3 4 3 6
18.05547009
5 14 20 19 1 10 18 17
0 16 0
//

Master 7: Lower Part of Small Shear Box

5 28
8 6 0
-17 -15 -1.651376147
-15 -15 -1.651376147
-15 15 -1.651376147
-17 15 -1.651376147
-17 -15 6.348623853
-15 -15 6.348623853
-15 15 6.348623853
-17 15 6.348623853
4 0 1 5 4
4 1 2 6 5
4 3 7 6 2
4 0 4 7 3
4 0 3 2 1
4 4 5 6 7
3 1 3 4
3 2 0 5
3 3 1 6
3 7 0 2
3 5 0 7
3 1 4 6
3 7 2 5
3 4 3 6
15.55634919
8 7 3 4 5 6 2 1
-16 0 2.348623853
8 6 0
-17 -17 -1.651376147
17 -17 -1.651376147
17 -15 -1.651376147
-17 -15 -1.651376147
-17 -17 6.348623853
17 -17 6.348623853
17 -15 6.348623853
-17 -15 6.348623853
4 0 1 5 4
4 1 2 6 5
4 3 7 6 2
4 0 4 7 3
4 0 3 2 1
4 4 5 6 7
3 1 3 4

3 2 0 5
3 3 1 6
3 7 0 2
3 5 0 7
3 1 4 6
3 7 2 5
3 4 3 6
17.49285568
23 21 18 8 22 20 17 5
0 -16 2.348623853
8 6 0
15 -15 -1.651376147
17 -15 -1.651376147
17 15 -1.651376147
15 15 -1.651376147
15 -15 6.348623853
17 -15 6.348623853
17 15 6.348623853
15 15 6.348623853
4 0 1 5 4
4 1 2 6 5
4 3 7 6 2
4 0 4 7 3
4 0 3 2 1
4 4 5 6 7
3 1 3 4
3 2 0 5
3 3 1 6
3 7 0 2
3 5 0 7
3 1 4 6
3 7 2 5
3 4 3 6
15.55634919
19 18 11 15 16 17 12 14
16 0 2.348623853
8 6 0
-17 15 -1.651376147
17 15 -1.651376147
17 17 -1.651376147
-17 17 -1.651376147
-17 15 6.348623853
17 15 6.348623853
17 17 6.348623853
-17 17 6.348623853
4 0 1 5 4
4 1 2 6 5
4 3 7 6 2
4 0 4 7 3
4 0 3 2 1
4 4 5 6 7
3 1 3 4
3 2 0 5
3 3 1 6
3 7 0 2
3 5 0 7

3 1 4 6
3 7 2 5
3 4 3 6
17.49285568
4 11 10 13 1 12 9 0
0 16 2.348623853
8 6 0
-17 -17 -3.651376147
17 -17 -3.651376147
17 17 -3.651376147
-17 17 -3.651376147
-17 -17 -1.651376147
17 -17 -1.651376147
17 17 -1.651376147
-17 17 -1.651376147
4 0 1 5 4
4 1 2 6 5
4 3 7 6 2
4 0 4 7 3
4 0 3 2 1
4 4 5 6 7
3 1 3 4
3 2 0 5
3 3 1 6
3 7 0 2
3 5 0 7
3 1 4 6
3 7 2 5
3 4 3 6
24.06241883
24 25 26 27 23 21 10 13
0 0 -2.651376147
//

Master 8: Tri-axial Plate

1 8
8 6 0
-0.75 -0.1 -2
0.75 -0.1 -2
0.75 0.1 -2
-0.75 0.1 -2
-0.75 -0.1 2
0.75 -0.1 2
0.75 0.1 2
-0.75 0.1 2
4 0 1 5 4
4 1 2 6 5
4 3 7 6 2
4 0 4 7 3
4 0 3 2 1
4 4 5 6 7
3 1 3 4
3 2 0 5
3 3 1 6
3 7 0 2
3 5 0 7
3 1 4 6

3 7 2 5
3 4 3 6
2.138340478
0 1 2 3 4 5 6 7
0.0 0.0 0.0
//

Master 9: Tri-axial Top and Bottom Plates

1 8
8 6 0
-1.5 -1.5 -0.1
1.5 -1.5 -0.1
1.5 1.5 -0.1
-1.5 1.5 -0.1
-1.5 -1.5 0.1
1.5 -1.5 0.1
1.5 1.5 0.1
-1.5 1.5 0.1
4 0 1 5 4
4 1 2 6 5
4 3 7 6 2
4 0 4 7 3
4 0 3 2 1
4 4 5 6 7
3 1 3 4
3 2 0 5
3 3 1 6
3 7 0 2
3 5 0 7
3 1 4 6
3 7 2 5
3 4 3 6
2.123676058
0 1 2 3 4 5 6 7
0.0 0.0 0.0
//

Master 10: Rail Seat

1 8
8 6 0
-0.14 -0.1016 -0.0889
0.14 -0.1016 -0.0889
0.14 0.1016 -0.0889
-0.14 0.1016 -0.0889
-0.14 -0.1016 0.0889
0.14 -0.1016 0.0889
0.14 0.1016 0.0889
-0.14 0.1016 0.0889
4 0 1 5 4
4 1 2 6 5
4 3 7 6 2
4 0 4 7 3
4 0 3 2 1
4 4 5 6 7
3 1 3 4
3 2 0 5
3 3 1 6
3 7 0 2

3 5 0 7
3 1 4 6
3 7 2 5
3 4 3 6
0.194488483
0 1 2 3 4 5 6 7
0.0 0.0 0.0
//
Master 11: Textured Tie
7 44
8 6 0
-0.6477 -0.083633759 -0.1016
0.6477 -0.083633759 -0.1016
0.6477 0.094166241 -0.1016
-0.6477 0.094166241 -0.1016
-0.6477 -0.083633759 0.1016
0.6477 -0.083633759 0.1016
0.6477 0.094166241 0.1016
-0.6477 0.094166241 0.1016
4 0 1 5 4
4 1 2 6 5
4 3 7 6 2
4 0 4 7 3
4 0 3 2 1
4 4 5 6 7
3 1 3 4
3 2 0 5
3 3 1 6
3 7 0 2
3 5 0 7
3 1 4 6
3 7 2 5
3 4 3 6
0.661620027
0 1 2 3 4 5 6 7
0 0.005266241 0
8 6 0
-0.647700000 -0.103633759 0.000000000
-0.431800000 -0.103633759 0.000000000
-0.431800000 -0.083633759 0.000000000
-0.647700000 -0.083633759 0.000000000
-0.647700000 -0.103633759 0.101600000
-0.431800000 -0.103633759 0.101600000
-0.431800000 -0.083633759 0.101600000
-0.647700000 -0.083633759 0.101600000
4 0 1 5 4
4 1 2 6 5
4 3 7 6 2
4 0 4 7 3
4 0 3 2 1
4 4 5 6 7
3 1 3 4
3 2 0 5
3 3 1 6
3 7 0 2
3 5 0 7

3 1 4 6
3 7 2 5
3 4 3 6
0.119724026
20 22 21 19 33 35 34 4
-0.539750000 -0.093633759 0.050800000
8 6 0
-0.431800000 -0.103633759 -0.101600000
-0.215900000 -0.103633759 -0.101600000
-0.215900000 -0.083633759 -0.101600000
-0.431800000 -0.083633759 -0.101600000
-0.431800000 -0.103633759 0.000000000
-0.215900000 -0.103633759 0.000000000
-0.215900000 -0.083633759 0.000000000
-0.431800000 -0.083633759 0.000000000
4 0 1 5 4
4 1 2 6 5
4 3 7 6 2
4 0 4 7 3
4 0 3 2 1
4 4 5 6 7
3 1 3 4
3 2 0 5
3 3 1 6
3 7 0 2
3 5 0 7
3 1 4 6
3 7 2 5
3 4 3 6
0.119724026
9 11 10 8 22 24 23 21
-0.323850000 -0.093633759 -0.050800000
8 6 0
-0.215900000 -0.103633759 0.000000000
0.000000000 -0.103633759 0.000000000
0.000000000 -0.083633759 0.000000000
-0.215900000 -0.083633759 0.000000000
-0.215900000 -0.103633759 0.101600000
0.000000000 -0.103633759 0.101600000
0.000000000 -0.083633759 0.101600000
-0.215900000 -0.083633759 0.101600000
4 0 1 5 4
4 1 2 6 5
4 3 7 6 2
4 0 4 7 3
4 0 3 2 1
4 4 5 6 7
3 1 3 4
3 2 0 5
3 3 1 6
3 7 0 2
3 5 0 7
3 1 4 6
3 7 2 5
3 4 3 6
0.119724026

24 26 25 23 37 39 38 36
-0.107950000 -0.093633759 0.050800000
8 6 0
0.000000000 -0.103633759 -0.101600000
0.215900000 -0.103633759 -0.101600000
0.215900000 -0.083633759 -0.101600000
0.000000000 -0.083633759 -0.101600000
0.000000000 -0.103633759 0.000000000
0.215900000 -0.103633759 0.000000000
0.215900000 -0.083633759 0.000000000
0.000000000 -0.083633759 0.000000000
4 0 1 5 4
4 1 2 6 5
4 3 7 6 2
4 0 4 7 3
4 0 3 2 1
4 4 5 6 7
3 1 3 4
3 2 0 5
3 3 1 6
3 7 0 2
3 5 0 7
3 1 4 6
3 7 2 5
3 4 3 6
0.119724026
13 15 14 12 39 41 40 38
0.107950000 -0.093633759 -0.050800000
8 6 0
0.215900000 -0.103633759 0.000000000
0.431800000 -0.103633759 0.000000000
0.431800000 -0.083633759 0.000000000
0.215900000 -0.083633759 0.000000000
0.215900000 -0.103633759 0.101600000
0.431800000 -0.103633759 0.101600000
0.431800000 -0.083633759 0.101600000
0.215900000 -0.083633759 0.101600000
4 0 1 5 4
4 1 2 6 5
4 3 7 6 2
4 0 4 7 3
4 0 3 2 1
4 4 5 6 7
3 1 3 4
3 2 0 5
3 3 1 6
3 7 0 2
3 5 0 7
3 1 4 6
3 7 2 5
3 4 3 6
0.119724026
28 30 29 27 41 43 42 40
0.323850000 -0.093633759 0.050800000
8 6 0
0.431800000 -0.103633759 -0.101600000

0.647700000 -0.103633759 -0.101600000
0.647700000 -0.083633759 -0.101600000
0.431800000 -0.083633759 -0.101600000
0.431800000 -0.103633759 0.000000000
0.647700000 -0.103633759 0.000000000
0.647700000 -0.083633759 0.000000000
0.431800000 -0.083633759 0.000000000
4 0 1 5 4
4 1 2 6 5
4 3 7 6 2
4 0 4 7 3
4 0 3 2 1
4 4 5 6 7
3 1 3 4
3 2 0 5
3 3 1 6
3 7 0 2
3 5 0 7
3 1 4 6
3 7 2 5
3 4 3 6
0.119724026
17 18 1 16 30 32 31 29
0.539750000 -0.093633759 -0.050800000
//
Mater 12: Plate
1 8
8 6 0
-15 -15 -1.74774775
15 -15 -1.74774775
15 15 -1.74774775
-15 15 -1.74774775
-15 -15 1.74774775
15 -15 1.74774775
15 15 1.74774775
-15 15 1.74774775

4 0 1 5 4
4 1 2 6 5
4 3 7 6 2
4 0 4 7 3
4 0 3 2 1
4 4 5 6 7
3 1 3 4
3 2 0 5
3 3 1 6
3 7 0 2
3 5 0 7
3 1 4 6
3 7 2 5
3 4 3 6
21.28507980
0 1 2 3 4 5 6 7
0.0 0.0 0.0
//
Master 13: Lower Part of the large Shear Box

5 28
8 6 0
-19.5 -15 -4.181095406
-17.5 -15 -4.181095406
-17.5 15 -4.181095406
-19.5 15 -4.181095406
-19.5 -15 10.818904594
-17.5 -15 10.818904594
-17.5 15 10.818904594
-19.5 15 10.818904594
4 0 1 5 4
4 1 2 6 5
4 3 7 6 2
4 0 4 7 3
4 0 3 2 1
4 4 5 6 7
3 1 3 4
3 2 0 5
3 3 1 6
3 7 0 2
3 5 0 7
3 1 4 6
3 7 2 5
3 4 3 6
16.80029762
8 7 3 4 5 6 2 1
-18.5 0 3.318904594
8 6 0
-19.5 -17 -4.181095406
19.5 -17 -4.181095406
19.5 -15 -4.181095406
-19.5 -15 -4.181095406
-19.5 -17 10.818904594
19.5 -17 10.818904594
19.5 -15 10.818904594
-19.5 -15 10.818904594
4 0 1 5 4
4 1 2 6 5
4 3 7 6 2
4 0 4 7 3
4 0 3 2 1
4 4 5 6 7
3 1 3 4
3 2 0 5
3 3 1 6
3 7 0 2
3 5 0 7
3 1 4 6
3 7 2 5
3 4 3 6
20.91650066
23 21 18 8 22 20 17 5
0 -16 3.318904594
8 6 0
17.5 -15 -4.181095406
19.5 -15 -4.181095406

19.5 15 -4.181095406
17.5 15 -4.181095406
17.5 -15 10.818904594
19.5 -15 10.818904594
19.5 15 10.818904594
17.5 15 10.818904594
4 0 1 5 4
4 1 2 6 5
4 3 7 6 2
4 0 4 7 3
4 0 3 2 1
4 4 5 6 7
3 1 3 4
3 2 0 5
3 3 1 6
3 7 0 2
3 5 0 7
3 1 4 6
3 7 2 5
3 4 3 6
16.80029762
19 18 11 15 16 17 12 14
18.5 0 3.318904594
8 6 0
-19.5 15 -4.181095406
19.5 15 -4.181095406
19.5 17 -4.181095406
-19.5 17 -4.181095406
-19.5 15 10.818904594
19.5 15 10.818904594
19.5 17 10.818904594
-19.5 17 10.818904594
4 0 1 5 4
4 1 2 6 5
4 3 7 6 2
4 0 4 7 3
4 0 3 2 1
4 4 5 6 7
3 1 3 4
3 2 0 5
3 3 1 6
3 7 0 2
3 5 0 7
3 1 4 6
3 7 2 5
3 4 3 6
20.91650066
4 11 10 13 1 12 9 0
0 16 3.318904594
8 6 0
-19.5 -17 -6.181095406
19.5 -17 -6.181095406
19.5 17 -6.181095406
-19.5 17 -6.181095406
-19.5 -17 -4.181095406
19.5 -17 -4.181095406

19.5 17 -4.181095406
-19.5 17 -4.181095406
4 0 1 5 4
4 1 2 6 5
4 3 7 6 2
4 0 4 7 3
4 0 3 2 1
4 4 5 6 7
3 1 3 4
3 2 0 5
3 3 1 6
3 7 0 2
3 5 0 7
3 1 4 6
3 7 2 5
3 4 3 6
25.88918693
24 25 26 27 23 21 10 13
0 0 -5.181095406
//
Master 14: TriX Geo-grid
3 12
8 6 0
-30 -17.32050808 -2
-28.26794919 -16.32050808 -2
0 32.64101615 -2
0 34.64101615 -2
-30 -17.32050808 2
-28.26794919 -16.32050808 2
0 32.64101615 2
0 34.64101615 2
4 0 1 5 4
4 1 2 6 5
4 3 7 6 2
4 0 4 7 3
4 0 3 2 1
4 4 5 6 7
3 1 3 4
3 2 0 5
3 3 1 6
3 7 0 2
3 5 0 7
3 1 4 6
3 7 2 5
3 4 3 6
30.07066794
0 1 4 5 6 7 10 11
-14.57127783 8.412731175 0
8 6 0
28.26794919 -16.32050808 -2
30 -17.32050808 -2
0 34.64101615 -2
0 32.64101615 -2
28.26794919 -16.32050808 2
30 -17.32050808 2
0 34.64101615 2

0 32.64101615 2
4 0 1 5 4
4 1 2 6 5
4 3 7 6 2
4 0 4 7 3
4 0 3 2 1
4 4 5 6 7
3 1 3 4
3 2 0 5
3 3 1 6
3 7 0 2
3 5 0 7
3 1 4 6
3 7 2 5
3 4 3 6
30.07066794
3 2 5 4 9 8 11 10
14.57127783 8.412731175 0
8 6 0
-30 -17.32050808 -2
30 -17.32050808 -2
28.26794919 -16.32050808 -2
-28.26794919 -16.32050808 -2
-30 -17.32050808 2
30 -17.32050808 2
28.26794919 -16.32050808 2
-28.26794919 -16.32050808 2
4 0 1 5 4
4 1 2 6 5
4 3 7 6 2
4 0 4 7 3
4 0 3 2 1
4 4 5 6 7
3 1 3 4
3 2 0 5
3 3 1 6
3 7 0 2
3 5 0 7
3 1 4 6
3 7 2 5
3 4 3 6
30.07066794
0 2 3 1 6 8 9 7
0 -16.82546235 0

C. POST PROCESSING MATLAB CODE

1. Read in DEM Output

```
fid = fopen('vect.txt','r');
c = 0;
cp=0;
V = zeros(500000,3);
NW = zeros(1,3);
SW = zeros(1,3);
m = input('input master block number---');
for i = 1 : 50000,
  if feof(fid)
    break;
  else
    A(i) = fscanf(fid, '%f', 1);
    B(i) = fscanf(fid,'%f\n',1);
    a(i) = fscanf(fid,'%f',1);
    b(i) = fscanf(fid,'%f\n',1);
    M(i) = fscanf(fid,'%f\n',1);
    n = 2*M(i);
    o = A(i);
    p = B(i);
    X=fscanf(fid, '%g %g\n',[3 n]);
    Y=X';
    % if the master block is A
    if o == m;
       for k = 1:2:n-1;
      V((2*c+k),1)= V((2*c+k),1)+ Y(k,1);
      V((2*c+k),2)= V((2*c+k),2)+ Y(k,2);
      V((2*c+k),3)= V((2*c+k),3)+ Y(k,3);
      NW=[V((2*c+k),1),V((2*c+k),2),V((2*c+k),3)];
      end
      for l = 2:2:n;
      V((2*c+l),1)= V((2*c+l),1)-Y(l,1);
      V((2*c+l),2)= V((2*c+l),2)-Y(l,2);
      V((2*c+l),3)= V((2*c+l),3)-Y(l,3);
      end
      cp=cp+M(i);%number of contact points
  end
    % if the master block is B, location is the same but force is in
the
    % opposite direction
    if p == m;
      for k = 1:2:n-1;
      V((2*c+k),1)= V((2*c+k),1)+ Y(k,1);
      V((2*c+k),2)= V((2*c+k),2)+ Y(k,2);
      V((2*c+k),3)= V((2*c+k),3)+ Y(k,3);
      NW=[V((2*c+k),1),V((2*c+k),2),V((2*c+k),3)];
      end
      for l = 2:2:n;
      V((2*c+l),1)= V((2*c+l),1)+Y(l,1);
```

```
      V((2*c+l),2)= V((2*c+l),2)+Y(l,2);
      V((2*c+l),3)= V((2*c+l),3)+Y(l,3);
      end
      cp=cp+M(i);
    end
    % find the contact point between two master block
      if a(i)==1;
          if b(i)==1;
               if o==m|p==m;
                for k = 1:2:n-1;
                  SW=[V((2*c+k),1),V((2*c+k),2),V((2*c+k),3)];
                end
            end
        end
    end
      c = c + M(i);
end
end
d = c;
cp
couple = i-1;

fclose(fid);
```

2. Plot Force Vectors

```
for i = 1: c;
    x(i)=V((2*i-1),1);
    y(i)=V((2*i-1),2);
    z(i)=V((2*i-1),3);
    u(i)=V(2*i,1);
    v(i)=V(2*i,2);
    w(i)=V(2*i,3);
end
   n = input('input scale factor ----');
%quiver3(x,y,z,u,v,w,n);
quiver(x,z,u,w,n);
```

3. Particle Visualization

```
n=input('please input total number of particles --- ');
V=csvread('v3d.dat');

face1=[1    2   6   5
2   3   7   6
4   8   7   3
1   5   8   4
1   4   3   2
5   6   7   8]; %vertice connection order for cubic shapes

face2=[1    2   9   7   8
```

```
2   2   2   3   9
3   3   5   7   9
3   3   3   4   5
5   5   4   6   7
1   1   1   8   10
6   6   10  8   7
4   4   4   10  6
1   10  4   3   2
];  %vertice connection for 6 face shape with 10 vertices

face3=[1    2   9   7   8
2   2   2   3   9
3   3   5   7   9
3   3   3   4   5
5   5   4   6   7
1   1   1   8   10
6   6   10  8   7
4   4   4   10  6
1   10  4   3   2
]; %vertice connection for 6 face shape with 10 vertices

%set(get(gca,'ZLabel'),'Rotation',0.0)
%set(get(gca,'XLabel'),'String','m','FontName','timesnewroman','FontWei
ght','bold','FontSize',18)
%set(get(gca,'YLabel'),'String','m','FontName','timesnewroman','FontWei
ght','bold','FontSize',18)
%set(get(gca,'ZLabel'),'String','m','FontName','timesnewroman','FontWei
ght','bold','FontSize',18)
%set(get(gca,'Title'),'String','Moving Plate Load
Test','FontName','timesnewroman','FontWeight','bold','FontSize',12)

m=1;
for i=1:n;
    partnum = V(m,1);
    partype = V(m,3);
  % find the particle material and assgin different color;
  if partmat(partnum)==1;
    if partype == 1;
        vertn=8;
        vertm=zeros(vertn,3);
        for vn=1:vertn;
            vertm(vn,1)=vertm(vn,1)+V(m+vn,1);
            vertm(vn,2)=vertm(vn,2)+V(m+vn,2);
            vertm(vn,3)=vertm(vn,3)+V(m+vn,3);
        end

patch('Vertices',vertm,'Faces',face1,'FaceVertexCData',hsv(8),'FaceColo
r',[0.6 0.45 0.2]);
     m=m+vertn+1;
     elseif partype >=2;
        vertn=10;
        vertm=zeros(vertn,3);
        for vn=1:vertn;
            vertm(vn,1)=vertm(vn,1)+V(m+vn,1);
            vertm(vn,2)=vertm(vn,2)+V(m+vn,2);
            vertm(vn,3)=vertm(vn,3)+V(m+vn,3);
```

```
        end

patch('Vertices',vertm,'Faces',face2,'FaceVertexCData',hsv(8),'FaceColo
r',[0.6 0.45 0.2]);
     m=m+vertn+1;
    end

  elseif partmat(partnum)==2;
     if partype == 1;
        vertn=8;
        vertm=zeros(vertn,3);
        for vn=1:vertn;
            vertm(vn,1)=vertm(vn,1)+V(m+vn,1);
            vertm(vn,2)=vertm(vn,2)+V(m+vn,2);
            vertm(vn,3)=vertm(vn,3)+V(m+vn,3);
        end

patch('Vertices',vertm,'Faces',face1,'FaceVertexCData',hsv(8),'FaceColo
r',[0.8 0.2 0.2]);
     m=m+vertn+1;
     elseif partype >=2;
        vertn=10;
        vertm=zeros(vertn,3);
        for vn=1:vertn;
            vertm(vn,1)=vertm(vn,1)+V(m+vn,1);
            vertm(vn,2)=vertm(vn,2)+V(m+vn,2);
            vertm(vn,3)=vertm(vn,3)+V(m+vn,3);
        end

patch('Vertices',vertm,'Faces',face2,'FaceVertexCData',hsv(8),'FaceColo
r',[0.8 0.2 0.2]);
     m=m+vertn+1;
     end

    elseif partmat(partnum)==3;
     if partype == 1;
        vertn=8;
        vertm=zeros(vertn,3);
        for vn=1:vertn;
            vertm(vn,1)=vertm(vn,1)+V(m+vn,1);
            vertm(vn,2)=vertm(vn,2)+V(m+vn,2);
            vertm(vn,3)=vertm(vn,3)+V(m+vn,3);
        end

patch('Vertices',vertm,'Faces',face1,'FaceVertexCData',hsv(8),'FaceColo
r',[0.2 0.6 0.2]);
     m=m+vertn+1;
     elseif partype >=2;
        vertn=10;
        vertm=zeros(vertn,3);
        for vn=1:vertn;
            vertm(vn,1)=vertm(vn,1)+V(m+vn,1);
            vertm(vn,2)=vertm(vn,2)+V(m+vn,2);
            vertm(vn,3)=vertm(vn,3)+V(m+vn,3);
        end
```

```
patch('Vertices',vertm,'Faces',face2,'FaceVertexCData',hsv(8),'FaceColo
r',[0.2 0.6 0.2]);
     m=m+vertn+1;
     end

     elseif partmat(partnum)==4;
     if partype == 1;
        vertn=8;
        vertm=zeros(vertn,3);
        for vn=1:vertn;
            vertm(vn,1)=vertm(vn,1)+V(m+vn,1);
            vertm(vn,2)=vertm(vn,2)+V(m+vn,2);
            vertm(vn,3)=vertm(vn,3)+V(m+vn,3);
        end

patch('Vertices',vertm,'Faces',face1,'FaceVertexCData',hsv(8),'FaceColo
r',[0.6 0.2 0.6]);
     m=m+vertn+1;
     elseif partype >=2;
        vertn=10;
        vertm=zeros(vertn,3);
        for vn=1:vertn;
            vertm(vn,1)=vertm(vn,1)+V(m+vn,1);
            vertm(vn,2)=vertm(vn,2)+V(m+vn,2);
            vertm(vn,3)=vertm(vn,3)+V(m+vn,3);
        end

patch('Vertices',vertm,'Faces',face2,'FaceVertexCData',hsv(8),'FaceColo
r',[0.6 0.2 0.6]);
     m=m+vertn+1;
     end

  end
end

view(3);
grid on
campos([-3 -6 3]);
camva(8.25);
%axis([0.05 3 0.05 3 0.05 3]);
axis([0.05 3 0.05 3 0.05 3]);
box
lighting gouraud
zoom(0.7);
```

D. MATLAB CODE FOR THE DYNAMIC TRACK MODEL

```
Read the file containing tie information

fid = fopen('element.txt','r')

for ii= 1 : 100,
  if feof(fid)
    break;
  else
    TIENO(ii) = fscanf(fid, '%f' , 1);
    TM(ii)  =   fscanf(fid, '%f' , 1);
    TIEP(ii)=   fscanf(fid,'%f \ n', 1);
  end
end

fclose(fid);

% 2. Read the file containing matreial properties

fid = fopen('mat.txt','r')

for ii= 1: 100,
    if feof(fid)
        break;
    else
        Kp(ii) = fscanf(fid,'%f',1);
        Kb(ii) = fscanf(fid,'%f',1);
        Dp(ii) = fscanf(fid,'%f',1);
        Db(ii) = fscanf(fid,'%f',1);
    Mt(ii) = fscanf(fid,'%f',1);
        Mb(ii) = fscanf(fid,'%f\n',1);
    end
end

fclose(fid)


function f=fet(V,tl,x,Rmr,Rpr,t,beta);
if x<=0;
    f=(V*Rmr*(exp(x*Rpr))*(exp((V*tl/V)*(i*beta-i*t-V*Rpr)))/(i*beta-
i*t-V*Rpr))+i*(V*Rpr*(exp(i*x*Rmr))*(exp((V*tl/V)*(i*beta-i*t-
i*V*Rmr)))/(i*beta-i*t-i*V*Rmr))-
(V*Rmr*(exp(x*Rpr))*(exp((V*0/V)*(i*beta-i*t-V*Rpr)))/(i*beta-i*t-
V*Rpr))-i*(V*Rpr*(exp(i*x*Rmr))*(exp((V*0/V)*(i*beta-i*t-
i*V*Rmr)))/(i*beta-i*t-i*V*Rmr));
else if x>=V*tl;
    f=(V*Rmr*(exp(-x*Rpr))*(exp((V*tl/V)*(i*beta-i*t+V*Rpr)))/(i*beta-
i*t+V*Rpr))+i*(V*Rpr*(exp(-i*x*Rmr))*(exp((V*tl/V)*(i*beta-
i*t+i*V*Rmr)))/(i*beta-i*t+i*V*Rmr))-(V*Rmr*(exp(-
x*Rpr))*(exp((V*0/V)*(i*beta-i*t+V*Rpr)))/(i*beta-i*t+V*Rpr))-
i*(V*Rpr*(exp(-i*x*Rmr))*(exp((V*0/V)*(i*beta-i*t+i*V*Rmr)))/(i*beta-
i*t+i*V*Rmr));
else
```

```
    f=(V*Rmr*(exp(-x*Rpr))*(exp((x/V)*(i*beta-i*t+V*Rpr)))/(i*beta-
i*t+V*Rpr))+i*(V*Rpr*(exp(-i*x*Rmr))*(exp((x/V)*(i*beta-
i*t+i*V*Rmr)))/(i*beta-i*t+i*V*Rmr))-(V*Rmr*(exp(-
x*Rpr))*(exp((0/V)*(i*beta-i*t+V*Rpr)))/(i*beta-i*t+V*Rpr))-
i*(V*Rpr*(exp(-i*x*Rmr))*(exp((0/V)*(i*beta-i*t+i*V*Rmr)))/(i*beta-
i*t+i*V*Rmr))+(V*Rmr*(exp(x*Rpr))*(exp((V*tl/V)*(i*beta-i*t-
V*Rpr)))/(i*beta-i*t-
V*Rpr))+i*(V*Rpr*(exp(i*x*Rmr))*(exp((V*tl/V)*(i*beta-i*t-
i*V*Rmr)))/(i*beta-i*t-i*V*Rmr))-
(V*Rmr*(exp(x*Rpr))*(exp((x/V)*(i*beta-i*t-V*Rpr)))/(i*beta-i*t-
V*Rpr))-i*(V*Rpr*(exp(i*x*Rmr))*(exp((x/V)*(i*beta-i*t-
i*V*Rmr)))/(i*beta-i*t-i*V*Rmr));
end
end
end


EI=4860000;    % Typical Rail Bending stiffness
EI1=600000;    % stiffness for 4 in aspahlt beam typical : 600000
Temp=0;   % N Rail Axial force due to hightemperature dt=15 cause
600000 N
xob=1.524;             % observation point (point of interest)
ntob=9;                % observation tie number
p=59;                  % kg/m Rail Mass
p1=1400;       % 1400kg/m asphalt beam mass, for 4 in thick and 10 ft
wide
k=100000000; % N/m/m modulus of subgrade reaction, typical 100000000
N/m/m
V=20;                  % m/sec train Speed (45 mph)
distance=8;            % total running distance
nyf=2048;              % nyquist frequency
sumt=1;               % sec total time calculated better to be product
of 2
N=30;                  % number of ties
d=1;                   % loading constants; p0(d-csina);
c=0.1;                 % loading constants
a=2*pi*500;            % loading frequencies 500 Hz
P0=177000;             % N dead weight
tl=distance/V;         % total train running time
dt=1/(2*nyf);          % time domian interval
fp=sumt/dt;            % fft points
dw=2*pi*(2*nyf-1)/(fp-1);              % fft point interval
r=Temp/(2*EI);
tob=TIEP(ntob);
lamda=(p/EI)^(1/2);
omega=1;
omega1=1;
for w=0:dw:(fp/2-1)*dw;
    if w==0;
    Urob(omega)=0;
    Uaob(omega)=0;
    Utob(omega)=0;
    Ubob(omega)=0;
    TBF(omega)=0;
    elseif w == (k/p1)^0.5;
    Urob(omega)=0;
    Uaob(omega)=0;
```

```
    Utob(omega)=0;
    Ubob(omega)=0;
    TBF(omega)=0;
    else
    R=(r^2+(w*lamda)^2)^0.5;
    RR=(R^2-r^2)^0.5;
    Rmr=(R-r)^0.5;
    Rpr=(R+r)^0.5;
    AAA=zeros(2*N,2*N);          % big stiffness matrix
    FFF=zeros(2*N,1);            % big force matrix
    Ur=zeros(N,1);               % rail deflection (w)
    Ua=zeros(N,1);               % aspahlt trackbed deflection (w)
    Ut=zeros(N,1);               % tie deflection (w)
    Ub=zeros(N,1);               % Ballast displacement (w)
    Am=zeros(N,1);               % rail force on pad
    Bm=zeros(N,1);               % force on asphalt track bed
    A1A=zeros(N,1);
    B1B=zeros(N,1);
    C1C=zeros(N,1);
    D1D=zeros(N,1);
    P1P=zeros(N,1);              % material vector pad
    B1B=zeros(N,1);              % material vector for ballast
%form parameter matrix;
    for nnn=1:N;
    P=Kp(TM(nnn))+i*w*Dp(TM(nnn));
    P1P(nnn,1)=P1P(nnn,1)+P;
    B=Kb(TM(nnn))+i*w*Db(TM(nnn));
    B1B(nnn,1)=B1B(nnn,1)+B;
    MT=Mt(TM(nnn))*w^2-P-B;
    MB=Mb(TM(nnn))*w^2-2*B;
    TB=B^2-MT*MB;
    A1=P*(1-P*MB/TB);
    A1A(nnn,1)=A1A(nnn,1)+A1;
    B1=B^2/TB;
    B1B(nnn,1)=B1B(nnn,1)+B1;
    C1=-B^2*P/TB;
    C1C(nnn,1)=C1C(nnn,1)+C1;
    D1=-B*(1-B*MT/TB);
    D1D(nnn,1)=D1D(nnn,1)+D1;
    end;
%form elements in the big stiffness matrix;
      for n=1:N;
        for m=1:N;
        xnm = TIEP(n)-TIEP(m);
        xobm= xob-TIEP(m);
               Kr(n,m)=(Rmr*(exp(-abs(xnm)*Rpr))+i*Rpr*exp(-
i*abs(xnm)*Rmr))/(-4*EI*R*RR);
               Krob(n,m)=(Rmr*(exp(-abs(xobm)*Rpr))+i*Rpr*exp(-
i*abs(xobm)*Rmr))/(-4*EI*R*RR);
               AKr(n,m)=A1A(m,1)*Kr(n,m);
               AKrob(n,m)=A1A(m,1)*Krob(n,m);
               BKr(n,m)=B1B(m,1)*Kr(n,m);
               BKrob(n,m)=B1B(m,1)*Krob(n,m);
            if w<(k/p1)^0.5;
               delta=((k-p1*w^2)/(4*EI1))^0.25;
```

```
Ka(n,m)=(sin(delta*abs(xnm))+cos(delta*abs(xnm)))/(8*EI1*delta^3*exp(de
lta*abs(xnm)));

Kaob(n,m)=(sin(delta*abs(xobm))+cos(delta*abs(xobm)))/(8*EI1*delta^3*ex
p(delta*abs(xobm)));
                CKa(n,m)=C1C(m,1)*Ka(n,m);
                CKaob(n,m)=C1C(m,1)*Kaob(n,m);
                DKa(n,m)=D1D(m,1)*Ka(n,m);
                DKaob(n,m)=D1D(m,1)*Kaob(n,m);
             elseif w>(k/p1)^0.5;
                delta1=((p1*w^2-k)/EI1)^0.25;
                Ka(n,m)=(exp(-abs(xnm)*delta1)+i*exp(-
i*abs(xnm)*delta1))/(-4*EI1*delta^3);
                Kaob(n,m)=(exp(-abs(xobm)*delta1)+i*exp(-
i*abs(xobm)*delta1))/(-4*EI1*delta^3);
                CKa(n,m)=C1C(m,1)*Ka(n,m);
                CKaob(n,m)=C1C(m,1)*Kaob(n,m);
                DKa(n,m)=D1D(m,1)*Ka(n,m);
                DKaob(n,m)=D1D(m,1)*Kaob(n,m);
             end;
           end;
           xn=TIEP(n);
           theta(n)=(P0/(-4*EI*V*R*RR))*(d*fet(V,tl,xn,Rmr,Rpr,w,0)-
c*fet(V,tl,xn,Rmr,Rpr,w,a)/2-c*fet(V,tl,xn,Rmr,Rpr,w,-a)/2);
      end;
%%assemble matrix;
    UL=AKr+eye(N);
    UR=BKr;
    LL=CKa;
    LR=DKa-eye(N);
        for nn=1:N;
            FFF(nn,1)=FFF(nn,1)+theta(nn);
            for mm=1:N;
               AAA(nn,mm)=AAA(nn,mm)+UL(nn,mm);
            end;
            for mm=N+1:2*N;
               AAA(nn,mm)=AAA(nn,mm)+UR(nn,mm-N);
            end;
        end;
        for nn=N+1:2*N;
            FFF(nn,1)=FFF(nn,1)+0;
            for mm=1:N;
               AAA(nn,mm)=AAA(nn,mm)+LL(nn-N,mm);
            end;
            for mm=N+1:2*N;
               AAA(nn,mm)=AAA(nn,mm)+LR(nn-N,mm-N);
            end;
        end;
% get displacement vectors (w) for tie position
        UU=(pinv(AAA))*FFF;
        for o=1:N;
            Ur(o,1)=Ur(o,1)+UU(o);
            Ua(o,1)=Ua(o,1)+UU(o+N);
            Am(o)=A1A(o,1)*Ur(o,1)+B1B(o,1)*Ua(o,1);
            Bm(o)=C1C(o,1)*Ur(o,1)+D1D(o,1)*Ua(o,1);
            Ut(o,1)=Ut(o,1)+Ur(o,1)-Am(o)/P1P(o,1);
```

```
            Ub(o,1)=Ub(o,1)+Ua(o,1)+Bm(o)/B1B(o,1);
        end
% obtain final results
    Urob1=AKrob(1,:)*Ur+BKrob(1,:)*Ua;
    Urob2=(P0/(-4*EI*V*R*RR))*(d*fet(V,tl,xob,Rmr,Rpr,w,0)-
c*fet(V,tl,xob,Rmr,Rpr,w,a)/2-c*fet(V,tl,xob,Rmr,Rpr,w,-a)/2);
    Urob(omega)=Urob2-Urob1;
    Uaob(omega)=CKaob(1,:)*Ur+DKaob(1,:)*Ua;
    Utob(omega)=Ut(ntob,1);
    Ubob(omega)=Ub(ntob,1);
    RTF(omega)=P1P(ntob,1)*(Urob(omega)-Utob(omega));
    TBF(omega)=B1B(ntob,1)*(Utob(omega)-Ubob(omega));
    BAF(omega)=Bm(ntob);
 end;
 omega=omega+1;
end;
 % obtain rest part of fft
 for w=(fp/2)*dw:dw:(fp-1)*dw;
        Urob(omega)=conj(Urob(omega-omega1));  %Ur at observation
        Uaob(omega)=conj(Uaob(omega-omega1));
        Utob(omega)=conj(Utob(omega-omega1));
        Ubob(omega)=conj(Ubob(omega-omega1));
        RTF(omega)=conj(RTF(omega-omega1));
        TBF(omega)=conj(TBF(omega-omega1));
        BAF(omega)=conj(BAF(omega-omega1));
        omega1=omega1+2;
        omega=omega+1;
  end;
f=0:dw:(2*nyf-1)*2*pi;
subplot(2,2,1); plot(f(1:fp/4)/(2*pi),real(Urob(1:fp/4)))
xlabel('Frequency');ylabel('Real Part Rail Displacement');
title('Frequncey Domain Response');
urob=2*nyf*ifft(Urob);
uaob=2*nyf*ifft(Uaob);
utob=2*nyf*ifft(Utob);
rtf=2*nyf*ifft(RTF);
tbf=2*nyf*ifft(TBF);
baf=2*nyf*ifft(BAF);
con1=-urob(5*fp/8);
con2=-uaob(5*fp/8);
con3=-tbf(5*fp/8);
con4=-baf(5*fp/8);
con5=-utob(5*fp/8);
con6=-rtf(5*fp/8);
disrob=urob+con1;
disaob=uaob+con2;
distob=utob+con5;
frt=rtf+con6;
ftb=tbf+con3;
fba=baf+con4;
time=1:fp;
subplot(2,2,3); plot(time(1:2048)/(2*nyf), disrob(1:2048))
xlabel('Time(sec)');ylabel('Displacement(m)'); title('Rail Deflection');
subplot(2,2,4); plot(time(1:2048)/(2*nyf), disaob(1:2048))
xlabel('Time(sec)');ylabel('Displacement(m)'); title('Asphalt Track-Bed
Deflection');
subplot(2,2,2); plot(time(1:2048)/(2*nyf), ftb(1:2048))
```

```
xlabel('Time(sec)');ylabel('Force(N)'); title('Force underneath the
Tie');
subplot(2,2,2); plot(time(1:2048)/(2*nyf), frt(1:2048))
xlabel('Time(sec)');ylabel('Force(N)'); title('Force on the Top of the
Tie');
```